TIRE DEFORMATION MODELING AND EFFECT ON AERODYNAMIC PERFORMANCE OF A P2 RACE CAR

by

Rotem Livny

A Thesis

Submitted to the Faculty of Purdue University

In Partial Fulfillment of the Requirements for the degree of

Master of Science in Engineering

School of Engineering and Technology

Indianapolis, Indiana

August 2021

THE PURDUE UNIVERSITY GRADUATE SCHOOL
STATEMENT OF COMMITTEE APPROVAL

Dr. Hamid Dalir, Chair

School of Engineering and Technology

Prof. Andy Borme

School of Engineering and Technology

Prof. Chris Finch

School of Engineering and Technology

Approved by:

Dr. Hamid Dalir

TABLE OF CONTENTS

LIST OF FIGURES

ABBREVIATIONS

CFD	computational fluid dynamics
FEA	finite element analysis
ALE	Arbitrary Lagrangian - Eularian
CP	contact patch
FP	footprint
DF	downforce
FW	front wing
RW	rear wing
UF	underfloor
LHS/RHS	left/right hand side
RH	ride height
EOS	end of straight
CRN	cornering
CAD	computer aided design
WBH	width between heels
EPI	ends per inch
SST	steady state transport
SLR	static loaded radius
RANS	reynolds averaged navier stokes
LES	large eddy simulation
DES	detached eddy simulation
SRF	single reference frame
MRF	Multiple reference frame

ABSTRACT

The development work of a race car revolves around numerous goals such as drag reduction, maximizing downforce and side force, and maintaining balance. Commonly, these goals are to be met at the same time thus increasing the level of difficulty to achieve them. The methods for data acquisitions available to a race team during the season is mostly limited to wind tunnel testing and computational fluid dynamics, both of which are being heavily regulated by sanctioning bodies. While these methods enable data collection on a regular basis with repeat-ability they are still only a simulation, and as such they come with some margin of error due to a number of factors. A significant factor for correlation error is the effect of tires on the flow field around the vehicle. This error is a product of a number of deficiencies in the simulations such as inability to capture loaded radius, contact patch deformation in Y direction, sidewall deformation and overall shifts in tire dimensions. These deficiencies are evident in most WT testing yet can be captured in CFD. It is unknown just how much they do affect the aerodynamics performance of the car. That aside, it is very difficult to correlate those findings as most correlation work is done at WT which has been said to be insufficient with regards to tire effect modeling. Some work had been published on the effect of tire deformation on race car aerodynamics, showing a large contribution to performance as the wake from the front tires moves downstream to interact with body components. Yet the work done so far focuses mostly on open wheel race cars where the tire and wheel assembly is completely exposed in all directions, suggesting a large effect on aerodynamics. This study bridges the gap between understanding the effects of tire deformation on race car aerodynamics on open wheel race cars and closed wheel race cars. The vehicle in question is a hybrid of the two, exhibiting flow features that are common to closed wheel race cars due to each tire being fully enclosed from front and top. At the same time the vehicle is presenting the downstream wake effect similar to the one in open wheel race cars as the rear of the wheelhouse is open. This is done by introducing a deformable tire model using FEA commercial code. A methodology for quick and accurate model generation is presented to properly represent true tire dimensions, contact patch size and shape, and deformed dimension, all while maintaining design flexibility as the model allows for different inflation

pressures to be simulated. A file system is offered to produce CFD watertight STL files that can easily be imported to a CFD analysis, while the analysis itself presents the forces and flow structures effected by incorporating tire deformation to the model. An inflation pressure sweep is added to the study in order to evaluate the influence of tire stiffness on deformation and how this results in aerodynamic gain or loss. A comparison between wind tunnel correlation domain to a curved domain is done to describe the sensitivity each domain has with regards to tire deformation, as each of them provides a different approach to simulating a cornering condition. The Study suggests introducing tire deformation has a substantial effect on the flow field increasing both drag and downforce.In addition, flow patterns are revealed that can be capitalized by designing for specific cornering condition tire geometry. A deformed tire model offers more stable results under curved and yawed flow. Moreover, the curved domain presents a completely different side force value for both deformed and rigid tires with some downforce distribution sensitivity due to inflation pressure.

1. INTRODUCTION

1.1 Tire Aerodynamics Overview

The tire and wheel assembly is known to account for significant amounts of the forces generated by a race car. Up to 25% of the vehicles entire drag [1] value can be traced back to the tire, as it is by itself a bluff body, and as such it produces some pressure drag. This is generally due to stagnation at the front of the tire while as the air accelerates over the top of the tire, it separates at some forwards position to the rear of it. The combination of the two creates a significant amount of drag in addition to its negative contribution downstream providing separated flow instead of high energy flow. [2] Downforce values are also negatively affected by the tires due to wheel lift. As the flow comes in contact with the front face of the tire it stagnates at a lower position than the axle center, thus creating a high-pressure area forcing the tire upwards. At the same time accelerated flow on top of the tire creates a suction region at the top [3]. These two coupled together along with the Magnus effect generating a force perpendicular to the direction of rotation creates the phenomenon known as wheel lift [4]. Work on this subject suggested that while wheel lift exists for both rolling and stationary tires, it provides for lower values for a rotating case as flow above the tire separates at a more forwards position, increasing pressure on top of the tire and also reducing drag as the stagnation point is lower down the surface [5]. Much work had been published on the vortex generation around a standalone tire simulating the effects on open wheel race cars [6] [7], yet limited amount of work was done on the effect of actual tire deformation to the flow field [8], let alone the effect on a closed wheel car. As the body of the vehicles covers most of the tire the driving force in closed wheel cars is the contact patch. On this section of the tire previous work suggested that increased energy coming into the leading edge of the contact patch, along with reduced energy going away from the trailing edge of the footprint, cause for a pressure differential [9]. These differential increases drag, while at the same time the reduced clearance between tire and road creates a negative pressure peak that provides suction. As a result, both downforce and vorticity in the axial direction (jetting) are increased as high pressure at the front is directed outboards of the tire due to the low-pressure peaks local to the edges of the contact patch [10]. This study will look into

the leading flow features and examine their importance to both local force generation and propagation downstream.

1.2 Objectives and Methodology

In order to be able to include realistic tire deformation in the CFD analysis, a tire deformation modeling technique has to be implemented. This technique has to be able to capture both static deformations as well as dynamic ones, doing so in a time efficient yet accurate fashion. The software chosen for the task is Abaqus by Dassault systems, which has a specific laid out procedure for implicit tire modeling to account for both static and dynamic deformations. This method has substantial usage in the tire industry and is considered accurate and efficient when done correctly. Once a tire model is generated it is to be verified against existing static and dynamic tire data. From that point loading conditions are to be calculated for each individual tire, as centrifugal forces induce roll and weight shift creating a large deviation between RHS and LHS tires, while the downforce distribution along with weight distribution provides for some relative difference between loading conditions for front and rear tires. A method for transferring nodal coordinates into 3D CAD model is to be implemented using excel VBA interacting with SolidWorks. This method is to be able to generate STL files designated for the CFD analysis in as automatic fashion as possible. The CFD analysis will be performed under a single loading condition for each tire, while steer and yaw will be swept to examine the deformation effect in a verity of cornering conditions. A curved domain will be simulated there after to determine the sensitivity of deformation modeling to CFD technique, as well as the sensitivity to deformation of front vs rear wheels. In addition, an inflation pressure sweep will be performed to investigate whether changing inflation pressure has a significant effect on the flow structures around a tire.

2. TIRE MODEL GENERATION

2.1 Tire Section Analysis

The tires in this study were supplied by "Hoosier tire", One of the leading racing tire manufacturers in the world. The P2 car developed at IUPUI is set to run on 20X7.5 – 13 tires. These tires have a slick tread and are bias tires as opposed to radials. While Hoosier tire could supply the actual tires, they could not supply any data on materials or build. Yet in order to construct an accurate model, these values had to be obtained. It was decided that since the main purpose of this study is to generate a modeling process of the effect of tire deformation on aerodynamics along with understanding the flow field around the vehicle, it is not necessary to create an exact tire model rather creating a similar enough model would be sufficient. An exact model would require material testing, test rig data and footprint data. All of which can be obtained at a testing facility, yet they would be expansive to test and time consuming. Reviewing literature on the subject, a similar tire had been modeled in the past. The tire in subject was used for the same purpose as this one, along with a similar size [11]. Thus material data such as rubber hyperelasiticy, viscoelasticity, and cord strength were extracted from literature. Obtaining the layout of the tire was done using the old school approach of drawing the tire on millimetric paper. A sheet is sectioned into 1X1 mm boxes. On this sheet it is easy to capture the tires outlines by drawing it once it is mounted to the rim. To do so the tire was cut to a cross section, and the beads were clamped at a fixed width. This width is an important characteristic of the tire, it is called the width between heels. And while this width will change once pressure is applied, the original state determines the amount a stress the tire would experience due to different rim width mounting. At a wide rim, the bead seat stress would be lesser than in a narrow rim, thus it will impact both dimensional similarity along with failure point due to excessive stress at the heel. This width was evaluated to be 8.75" to allow for the mounting range listed by Hoosier as 7-9" rim width. The nominal position of an 8" rim would be too narrow for the WBH size as the fit on a 9" rim will be loose, thus a value closer to 9" yet not as wide was selected. The layout was sketched by hand multiple times to ensure repeatability. Coordinates were marked in key locations along the tire to construct the curves to be fitted using CAD. Tread,

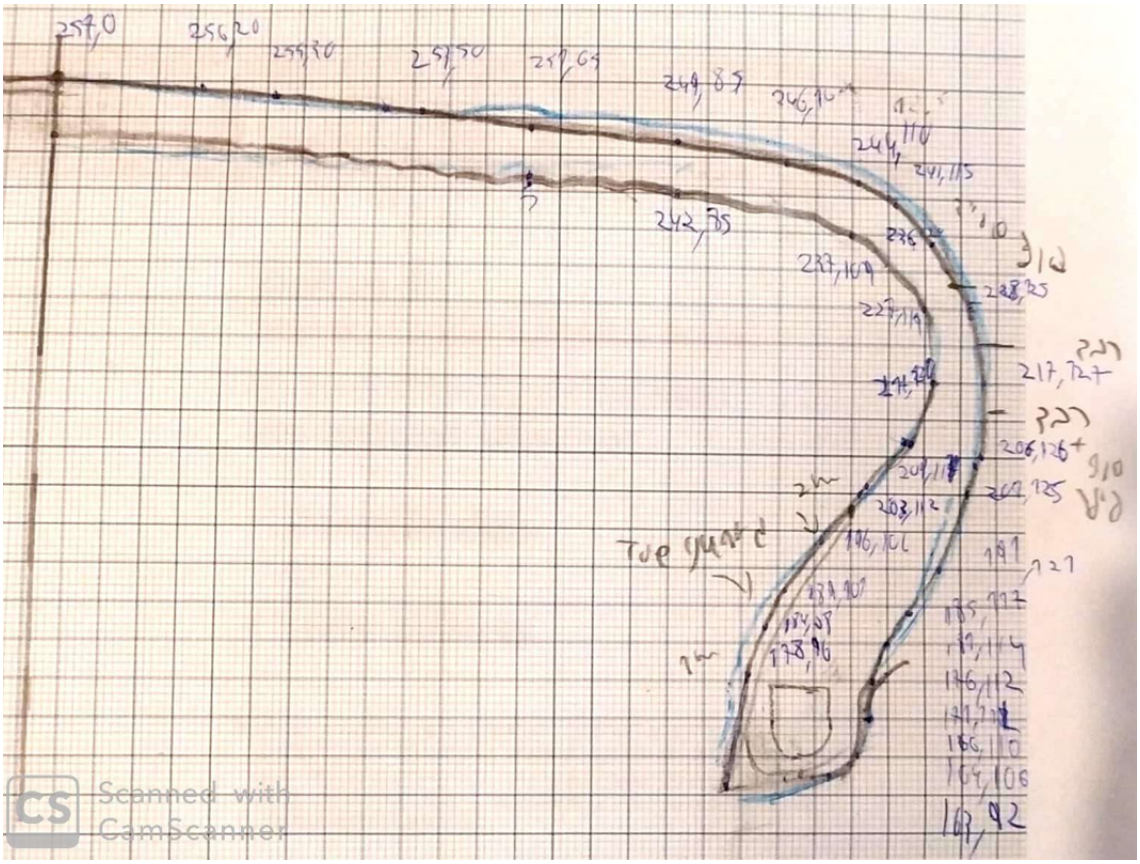

Figure 2.1. Tire cut section analysis

side wall and innerliner end locations were marked along with measured thickness, while the bead was located in plane by ink marking the cut section and placing it on the sheet as was done for the bead filler. A second tire was kept intact for measurements and comparison to cross section. This layout was later sketched using solidworks adding the ply representation. The sketch was then exported into "Abaqus". This sketch is the representation of the rubber cured uninflated dimensions. To this cross section, rubber data can now be assigned for the tread, sidewall innerliner, bead filler and toeguard. Once the rubber was set it was needed to investigate the plies construction, as this will have the dominant effect on tire stiffness and force generation properties. In order to model the cords in a sufficient manner cord material had to be evaluated, along with number of plies, ply angle, and ply density (EPI). The cross section was cut in the middle to enable this study, as in this manner a simple approach was taken for section analysis. It was found that the tire consists out of three plies, two of which

were made from the same material while the third ply was made from a different material. To better evaluate it, each ply was exposed by carving through the rubber and then cutting a sample size piece to examine the cord strength. As was discussed above, this is a simplistic approach and only should be taken under time and financial constraints. It was concluded that the two plies were made out of polyester like material, while the third was an Aramid hybrid due to extreme difference in shear resistance. This build characteristics agreed with work done on similar purpose and sized tires, thus assuring the conclusions are within logic. The next phase was to determine the crown angle. Using geometrical relations it was possible to obtain the angle. For a fixed width in X, the visible ends were counted in both the X and Y directions. Dividing the distance in Y by the distance in X and applying arc-tan, the cured angle is revealed and was calculated to be +-25 for all plies. One must keep in mind that the ply angle changes from build to post inflation to uninflated tire (lift factor), yet since the mold data is not available, this property is extremely difficult to evaluate, thus ply angle was maintained at +-25 constant disregarding the lift factor. Two additional quantities called "Ends Per Inch" (EPI) and "Spacing" are needed to complete the analysis setup. EPI is calculated by dividing the ends counted by the ply angle, as to place them in a parallel plane to the cut angle in order to obtain the correct EPI (laying the plane). Spacing is calculated as the distance between centerlines of the rebars in the true plane parallel to the cut plane, and is obtained from the diameter of the cord along with the EPI. Using these values it is now possible to assign them to rebars in the FEA model.

2.2 FEA Model Setup

The FEA code used for this study is the "abaqus" implicit code with the "Arbitrary Lagrangian-Eularian" frame work. Much of the capabilities of this software were developed specifically for tire analysis and simulation. This code is common in the tire industry thus it offers a robust package that is well regarded. The FEA tire simulation procedure is comprised out of sub steps with each one filling a specific purpose in order to save computational time without loss of accuracy. The first step is the generation of a 2D Axisymmetric model. An axisymmetric cross section of the tire is modeled, mounted and inflated to the designated

pressure. Since this is a 2D analysis, it is quick to solve and provides for an early fault detection analysis, as it shows mistreated areas that can be easily fixed and reiterated. The rubber components are modeled as shell elements with enabled twist - CGAX4H - and hybrid formulation, as rubber is an incompressible material, thus it cannot calculate stress due to nodal displacement under pressure stress. The hybrid formulation adds a degree of freedom to enable this calculation, thus for any incompressible material analysis this feature has to be present. Rubber is considered a hyperelastic material under steady state loading, therefore the yeoh Hyperelasticity model was chosen as was described in the work of . The viscoelasticity is defined using a Prony series representation which, is a function defining the decay in a property with respect to time, which is essentially what viscoelasticity means. In this case, the stress in a fixed strained rubber relaxes/ decays as the rubber maintains its predetermined deformation. Both quantities differ from one rubber to the other, yet for this study a representing rubber material was chosen for each segment of the tire, as both studies are examining tires in similar dimensions and from the same application [12]. Rebar elements were modeled using surface elements - SFMGAX1 - and are constrained to the rubber using the embedded elements constraint. This constraint essentially binds the rebar to the rubber and calculates the movement of the two combined together. Using the quantities acquired in the physical set up chapter, the rebar is fully captured as a strengthening component. The rim is modeled as a rigid surface and only the contact of the heel with the rim is modeled, as the rest has no significance in the virtual tire assuming the rim is fully rigid. The rim contact is described as frictionless. Two steps are performed on this Axisymmetric model. The first being a mounting step, as the rim is moved to its end position, which is the actual rim width. The predefined contact region moves with it as to make contact with the rim surface. Once the rim is in its final position and has some contact with the tire, the next step is performed. This step is the pressure step where the inner edge of the cross section is applied with a pressure boundary condition to simulate inflation. Once the tire reaches the final loading increments it presents a fully inflated cross section of a tire mounted to the proper rim.

The next step is to take that model and revolve it around the centerline of the tire as to create a half tire with a symmetry constraint. This analysis provides a more accurate

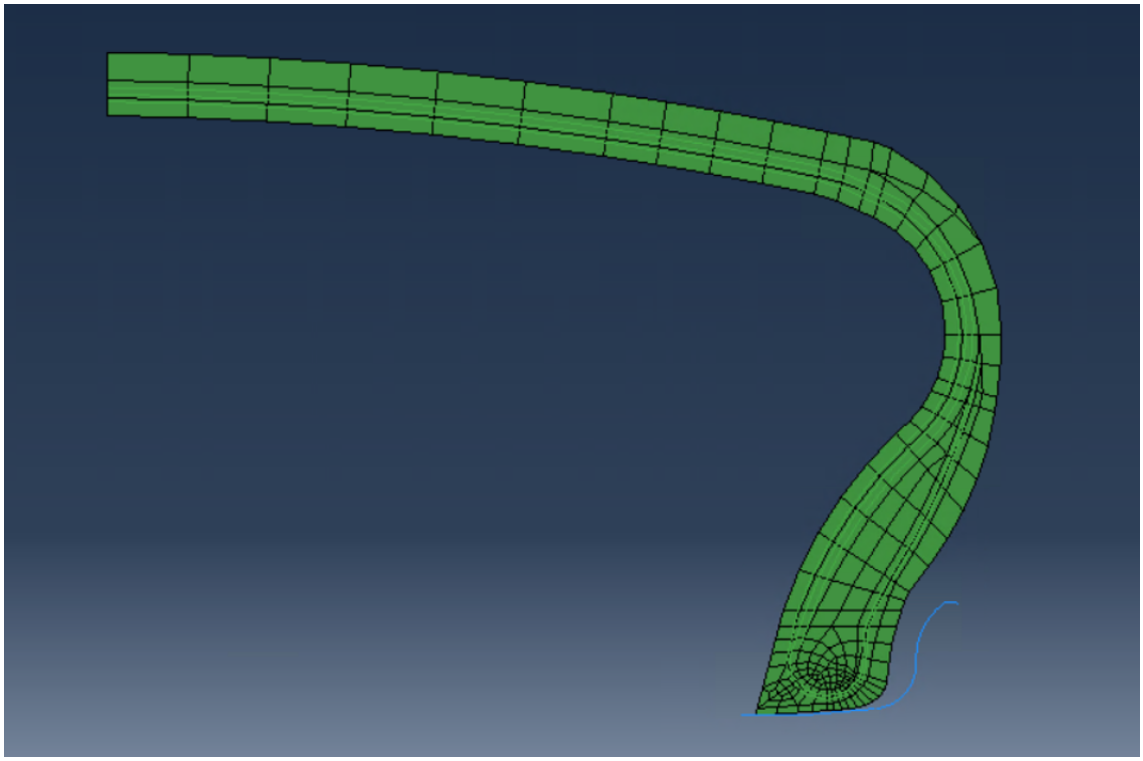

Figure 2.2. Axisymmetric mesh

description of the fully inflated tire, as 3D cells react slightly different than 2D cells, thus the final dimensions can defer to some extant from the Axisymmetric analysis. In the revolve stage, loads can be applied to the model as it is pressed against a rigid surface, while the following step simply reflects the tire about the centerline to create a full 3D tire analysis. This action saves computational resources, as loads are applied to the half model and then reflected to the full model. Yet in this study a slightly different approach was taken as the file structure calls for a higher level of modularity, even at the cost of some increased computational time. After the static model is generated, the last step is a steady state rolling analysis that takes the output of the last analysis and uses it as input of the SST. It is much more convenient to call for the correct step that corresponds to a curtain load once all of the loading conditions are grouped under the same file. That is why the revolve option was applied without loading, while after the tire was reflected, load was applied to it and that output was used in the SST analysis. Each step of the reflect analysis represents a different tire (LF,LR,RF,RR) by changing the loading condition according to the data acquired in the

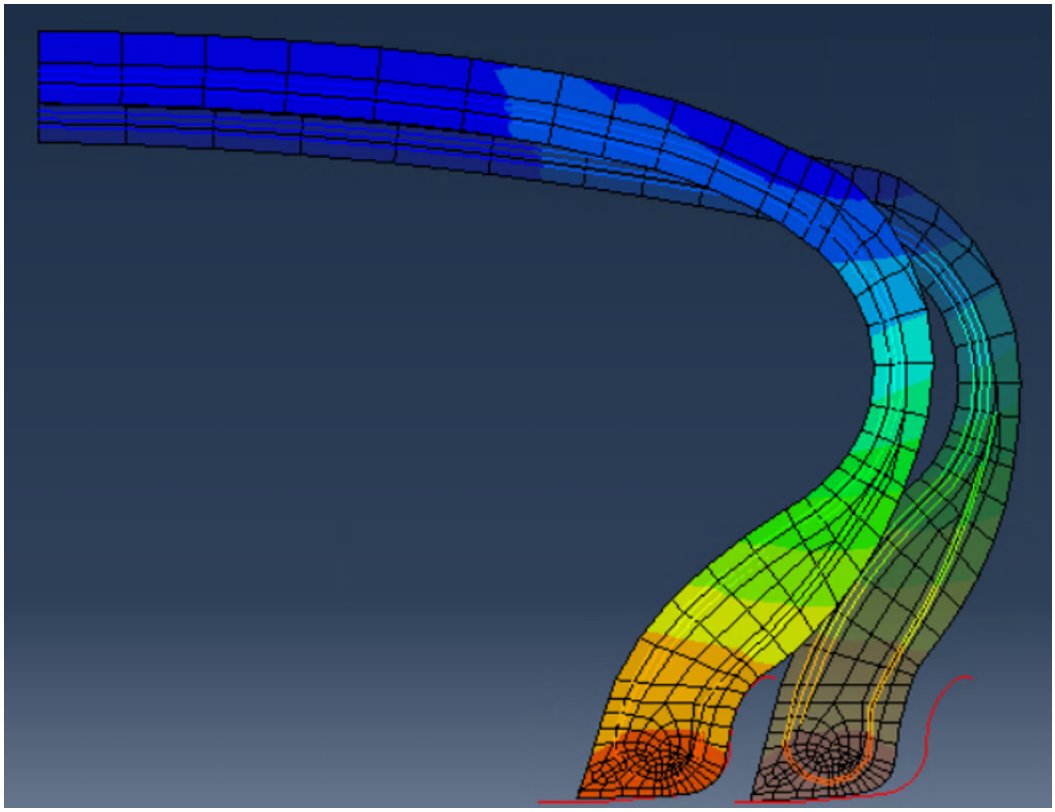

Figure 2.3. Inflation and Mounting

preliminary study. For EOS and CRN straight line positions only two tires were analyzed, assuming loading symmetry, while for the cornering conditions weight shift was calculated and added to each tire accordingly. Thus, the overall load on each tire was comprised out of mass of the vehicle at 45% distribution, downforce with the balance results from preliminary data set and weight shift due to cornering (no banking was considered for generalization). Drag effect on front to rear weight shift was neglected due to unknown center of pressure height, along with neglectable contribution to loading and unloading front/rear. Load cases were calculated using a simplified vehicle dynamics model. This was done as the steering geometry was not yet decided, suspension geometry and behavior were undecided as well. In addition, since this process can be added to any vehicle dynamics model it is of lesser importance to fully capture the dynamic behavior of the car, yet it is needed to include some realistic roll value along with a common pivot for the front wheels. A scenario was chosen to fit the current vehicle performance - this would include a cornering maneuver at 100 mph

through a 318 ft radius corner producing 2G of lateral acceleration. Using these quantities and the geometry in place, the roll gradient was calculated and found to produce a 0.5 degree of roll for the given acceleration. These calculations resulted in a maximum weight shift of 677 lbs. Each tire was given a downforce load according to the initial data set, that resulted in a 50% aero balance front and aft as well as side to side, thus the average downforce was distributed evenly between all four tires. A representative downforce value was calculated from the initial data set for each of the conditions – EOS, CRN and fully including steer and yaw in cornering RH – thus every tire was loaded with a specific load for the given analysis. The corresponding rigid tire received the same treatment as the same loads were applied to it using the spring rate data, the loaded radius was calculated and a plane was set in that radius to cut the tire, as this would be the interaction with the ground plane. In the initial data set, the car was found to be quite indifferent to both yaw and steer thus the loading conditions do not vary wildly from case to case. For a more sensitive vehicle an iterative process might be more suitable assuming initial loading due to aerodynamics, performing the analysis, and reiterating to solve the tire again with the obtained results. Once each tires deflected state had been captured, the final step in the process is to conduct a Steady State transport analysis. In this analysis a special framework developed by "Abaqus" called the "Arbitrary Lagrangian-Eularian" approach was implemented.

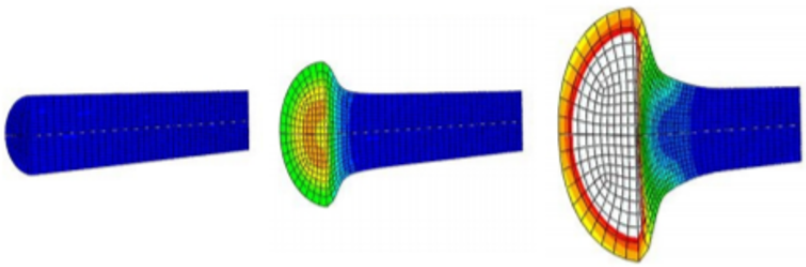

Figure 2.4. ALE example

This method is a clever and simple approach for reduction in computational time while maintaining accuracy using an implicit solving method compared to the resource demanding explicit analysis. This is done by defining a Lagrangian mesh, which exactly follows the material as was generated in the last increment of the reflect analysis. A rotational velocity

is then applied to this mesh, using an Eularin domain allowing the material to revolve within the mesh, while a subsequent Lagrangian half step is then computed to indicate the new location of the mesh in order to maintain all of the initial components within the model. For this analysis to be repeatable it is needed to define a free rolling state. This state

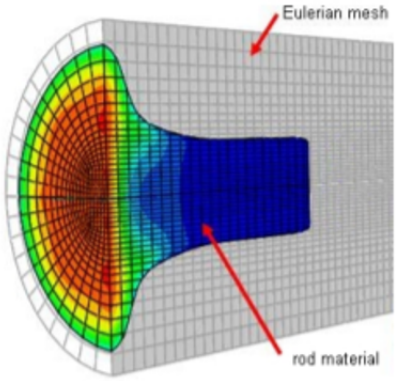

Figure 2.5. Eulerian mesh

indicates a case where no tractive or braking forces are applied to the tire. Applying a slip angle from this position would provide for a source of comparison, otherwise it will be difficult to properly compare states as both X and Y forces will vary. To compute the free rolling position a full braking and full traction steps are executed with the point where the forces generated equal to 0, being the free rolling position. Full traction will be at the most compressed position of the tire, which due to centripetal forces will be the SLR or static loaded radius, while full braking will be the most stretched position of the tire, which essentially is the inflated radius. At some point in between will be the transition from maximum to minimum which is the free rolling state. Thus, for each tire a SST analysis is performed using this methodology while adding an increased precision step. This step is aimed for describing the free rolling rotational velocity in the most accurate manner. It is done using a zoomed in approach changing maximum and minimum Ω values to a narrower span, thus increasing precision. This further ensures that the tire is completely at free rolling, allowing for the most accurate source of comparison. Once free rolling is obtained, a slip angle is added to the model by introducing a X and Y component of velocity. This

angle is supplied in increment of 0.1 from 0 to 10 degrees, thus providing 10 equilibrium states of the tire under 10 different slip angles. It is important to note that while the lateral slip is controlled explicitly, the longitudinal slip is a function of the rotational velocity and the friction coefficient. For this analysis some simplification is taken into account as the friction coefficient in X and Y is maintained constant and equal, while the actual friction behavior is known to vary with speed, temperature and in X and Y. While the ALE is a framework that reduces computational time, it has one flaw that can impact an analysis involving large dynamic deformation. As the material flows through the mesh there is a limit as to how large the Lagrangian deformation can be at the end of the step. Thus higher levels of friction results in larger deformation that cannot be captured in this analysis, and requires an explicit solver to do so. This limit will be tested on the virtual tire to determine if the ALE framework is sufficient for this study.

2.3 Tire testing and verification

When using a FEA tool to model a tire, it is highly recommended to verify the results by comparing the model to real tire measurements. The verification process is usually comprised out of 3 steps:

Dimensional similarity. In this step the simulated tire is first mounted to the corresponding real tire rim width and then inflated to a specific inflation pressure. Using the probe tool, it is easy to locate the minimum and maximum deviation from real tire measurement which is done by simply using a measurement tape for measuring circumference of the tire and its width. It is of high importance to measure the tire at the same rim width, as a reduction in rim width can alter the results by increasing circumference and limiting sidewall deflection. For this case, "Hoosier tire" provided the formal dimensions for this specific tire that were then used to compare against the simulated tire. Outer diameter was measured at 20.6" for the real tire while the simulated one resulted with an O.D of 20.59". The measured section width was slightly narrower than the simulated one listed at 9.4" while the analysis showed a section width of 9.55". While there is some deviation in the results for the section width, the diameter is precisely the same. In addition, the 0.15" deviation is relatively small

especially when taking into account tire to tire variation due to building and curing inaccuracies as well as measurement repeatability errors. Thus, it can be concluded that the tire possesses dimensional similarity to the real tire and the second phase of verification can now be examined.

Static loading. This phase is usually conducted on a testing rig that has pressure sensors in its floor. The tire is fixed in space and unable to rotate nor deflect in any other axis except for the Z axis (Vertical) while the floor raises up to press the tire against a predetermined load. This method determines the vertical stiffness of the tire (i.e spring rate) by repeating the test at a variety of loads and inflation pressures. It also provides the static loaded radius and sidewall deflection at every data point, while the pressure sensors provide a scan of the contact patch allowing to see the contact patch size, shape and pressure distribution. Unable to perform a physical test, again relying on "Hoosier tire" data was the guideline for spring rate verification while the contact patch could not be evaluated by correlation. The model was tested at three different inflation pressures adding load in 100

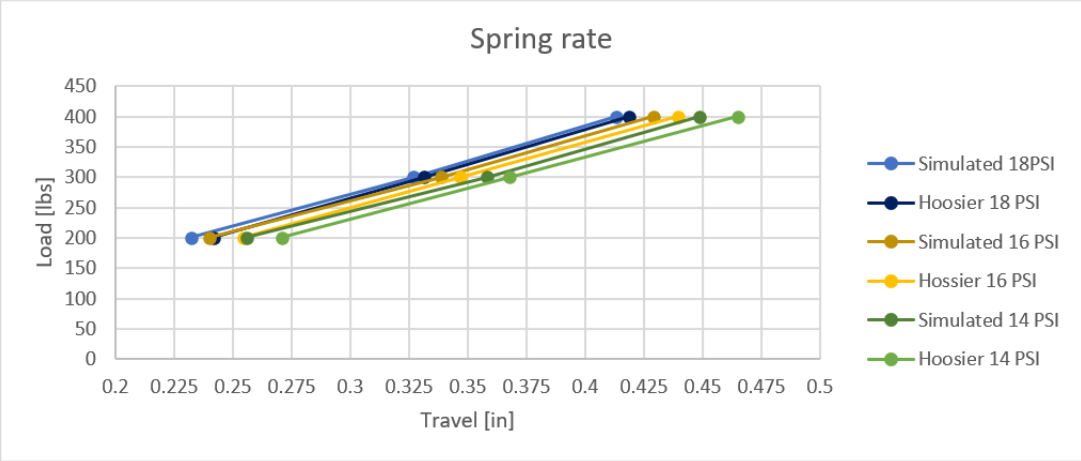

Figure 2.6. Spring rate analysis

lbs increments up to 400 lbs. It was found that as the pressure increased the correlation improved resulting in an average error of 0.66% for the 18 PSI case, where at the same time even the 14 PSI case correlated well producing an average error of 1.36%. In addition to the resulting numbers, the tire showed a linear response over the testing range, as was expected,

thus the simulated model showed good correlation for spring rates, static loaded radius and a linear response concluding that it can be used with high accuracy for static cases.

Dynamic verification. Determining the dynamic response of a tire is done by either road testing or at a test rig. Testing at a test rig can provide the dynamic loaded radius, longitudinal and lateral slip along with forces in all directions. In some cases, even a dynamic footprint can be obtained. Since tire testing is an expensive and time-consuming process, a set of available tire data that was gather for the very similar 20.5X7 – 13 tire also from "Hoosier tires", was used for this section, as it was assumed that it has the same build, materials and compounds with only slight changes to diameter and width. The test was conducted under the "Calspan" facility which is one of the leading tire test centers in the world and provides service to FSAE teams in order to obtain accurate tire data. The tire was tested for longitudinal slip under various loading conditions, inflation pressures and camber angles. Under the same conditions the tire was also tested for lateral slip. Using the relation

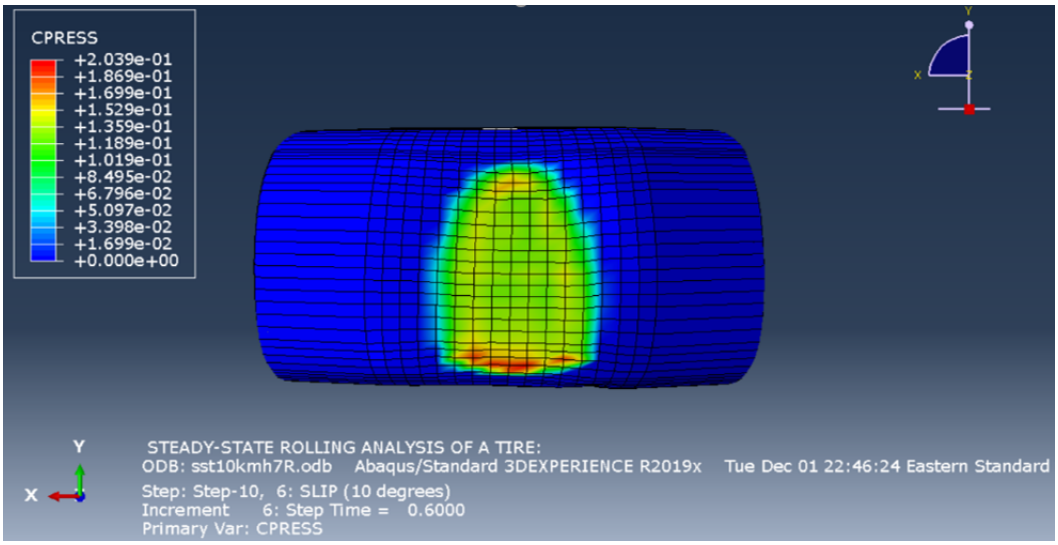

Figure 2.7. SST Slip analysis

$Fx = \mu * Fz$ and dividing the Fx which is measured by the Fz which is given and controlled, yields the μ for the given slip state [13] [14]. Using this approach over the test data, it is possible to construct a plot of μ values as a function of slip and from there determine the peak μ and the average μ level. For design purposes, the peak μ is calculated as this is the value where the largest force can be generated, thus it is desired to maintain operating

conditions that would allow for this peak value to be applicable. The simulated tire had gone through the same virtual process as the real tire. Inflation pressure was changed from 18 PSI to 12 PSI to match the "Calspan" data, the tire was then given a rotational velocity based on the calculated free rolling radius. Slip was calculated as the relation is known as $1 - wr/V$, while slip angle was given as input for the slip angle analysis. Using these calculated slip values along with the methodology to obtain the μ values, a data set was extracted from the analysis containing the tractive force, slip values and μ values. Since the "Calspan" rig along with this specific tire construction allows for extremely high μ values it was decided to normalize the force to obtain the response characteristic, as it was assumed that correlating the tires normalized behavior would present the quality of the analysis for a general case, while applying a specific μ level would be for a unique case. Where at this point the ALE approach might be insufficient and thus a much more time-consuming explicit approach would be needed. Since this study intends to present a best practice for time efficient tire modeling for aerodynamics development, an explicit approach is unrealistic as the time and effort involved in the process makes the tire modeling redundant as the time gap between CFD runs and FEA runs would be too high to keep up with. For that reason, using the normalized response will be sufficient as it will capture the quality of the simulated tire under the same relative conditions. Both sets of tire data were normalized for a side force value ranging from 0 to 1 at the same inflation pressure. Plotting the normalized response of the simulated tire on top of the measured tire provided a graph that showed both sets of data correlate nicely, presenting the same exact response from a 4 degree slip angle to 10 degrees, while the linear slope representing the tires lateral stiffness or Ca showed good agreements with measured and simulated data with the correct linear slope along with a very similar generated force for a given slip angle. The results were then compared to a case with an 18 PSI inflation pressure to demonstrate the uniqueness of the normalized response to a given set of initial conditions. As can be seen the 18 PSI case produces lower force values for a given slip angle, due to a lesser lateral deflection of the tread and a smaller contact patch – higher slip for the same force. This set of data shows that the simulated tire is a good representation of the real tires side force generation, keeping in mind that the limit of the model is not material failure rather it is the modeling method of the ALE limiting the amount

of deformation in the Lagrangian mesh for the Lagrangian half step segment of the framework Thus while this model captures the tires response in a very accurate manner, it is limited to

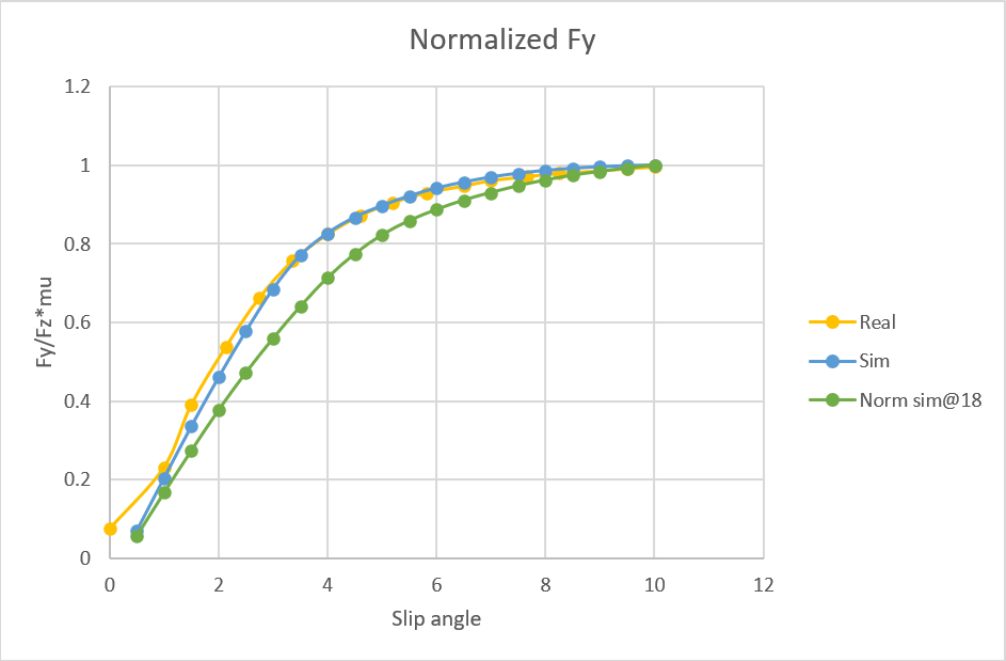

Figure 2.8. Normalized Fy simulated VS test data

μ values lower than the values the tire can produce on"Calspans" test rig which were tested to be close to 3.0, where the simulated tire was found to be limited to 1.3 μ values which still represents a real life racing value. That said, using the scaling factor by normalizing the response and then using the correct μ value, it is possible to shift one model from its friction behavior and explore if the variation is magnified as the friction value increases. As can be seen in this plot, using the normalized response assumption provides high correlation levels for both matching the real tire and the simulated one. The next verification to be conducted is the longitudinal force generation. This section was done in a similar manner to the side force verification, as the normalized longitudinal force was plotted against the longitudinal slip in percentage. This was done for both braking and tractive performance, whereas the side force was only tested to one side cornering.

It can be seen that once again the normalized response of the simulated tire matches the response of the measured tire. A slight overshoot can be observed in the braking side of

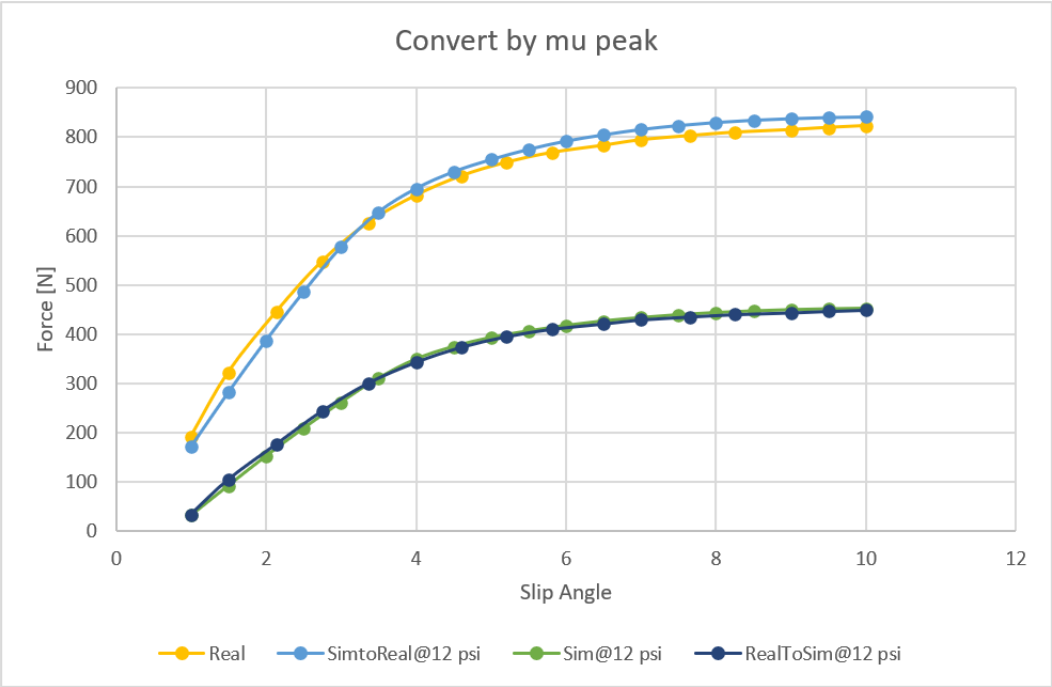

Figure 2.9. Conversion by Mu peak

the plot, showing higher values in the simulated tire, yet at the same time the longitudinal stiffness determined by the slop at the origin is identical, suggesting that within the test range the tire shows the same behavior. Thus, once dimensions, static measurements and dynamic measurements were confirmed and showed good correlation to the real tire, it can be concluded that this tire model is sufficient for this study and is a physical representation of the real tire.

2.4 File structure

Once the simulated tire was proven to match the real tire behavior and dimensions, it was now needed to create a simple framework that will transfer the coordinates from "Abaqus" into "SolidWorks" in order to create a smooth STL file for CFD analysis. To do so a visual basic code was written that extracted nodal coordinates from "Abaqus" and saved them as an excel file. This file was then reorganized as the reflect procedure generates the nodes in a reverse order to the revolved feature, thus renumbering the nodes is needed in order to create a full cross section at a given location on the tire. 24 such cross sections are needed

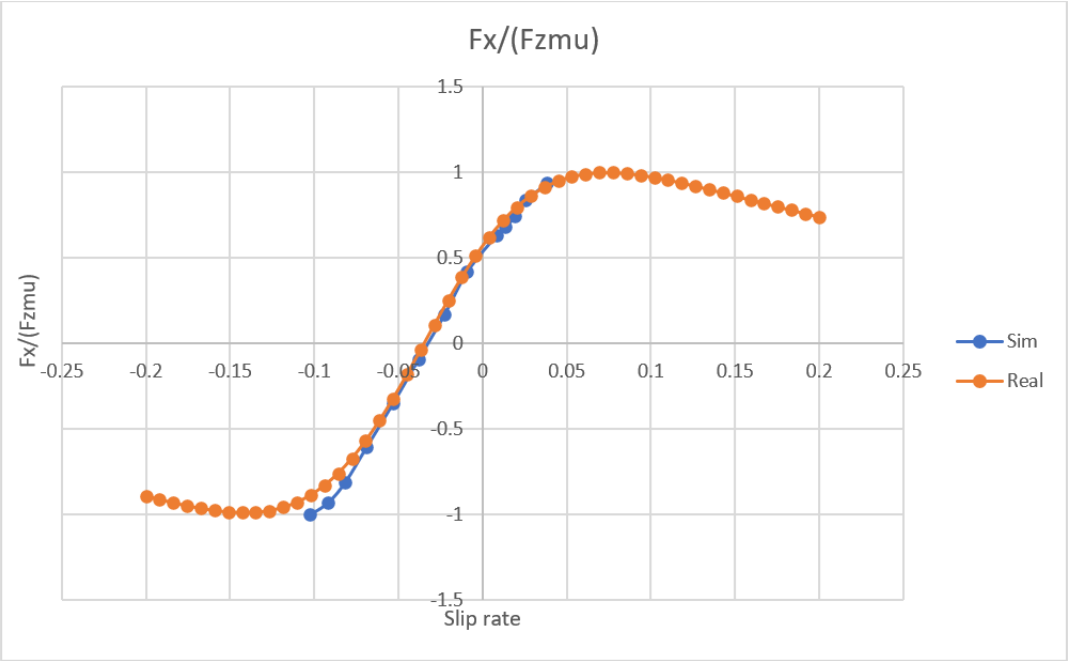

Figure 2.10. Normalized Fx simulated VS test data

with 16 of them representing the contact patch area, as this area experiences the highest amount of deformation thus increasing discretization in that area is essential to fully capture the correct shape of the deformed tire. The VBA code rearranged the nodes and then saves each cross section as a single *txt file while adding 4 more files, each representing a guide point along the tire circumference. Two points, one at the outer midpoint of the tire and the other at the inner midpoint, while two more points at the heels, are documented to form 4 guide curves. A grided 3D tire is generated in SolidWorks using this code and the "spline through XYZ" command, with a lofted surface connecting between each cross section. The sections are then patched together and being made a solid body. Using this code generates the tire in a timely manner speeding the CAD generation phase, as it is only needed to assemble each tire to the correct rim at the designated position in the master assembly file. This code can be upgraded to fully automize the procedure in future work, as to include the surfacing phase in the code itself reducing preparation time even more. The use of this code enabled the large data set matrix to be generated. Each tire was then assembled to the rim according to its orientation. It is important to do so as the contact patch is asymmetrical

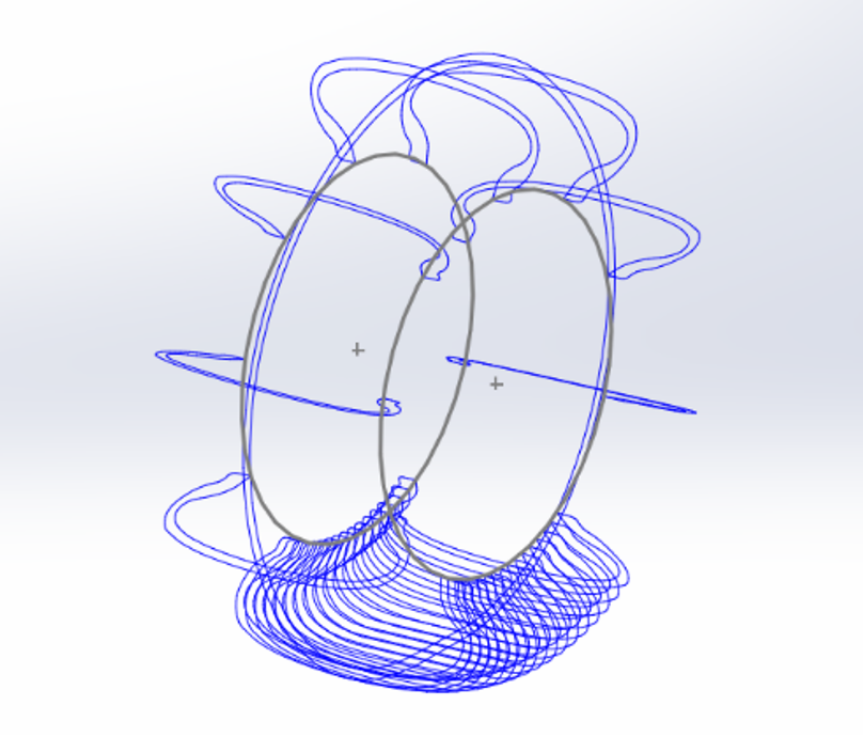

Figure 2.11. 3D Wireframe tire construction

even in straight line conditions due to the asymmetric construction of the tire, this is even more important when slip angle is applied. The process is repeated for each tire, while Z location of the centerline is documented as this will represent the rotational velocity of the MRF domain. While modeling the exact deformation of each tire takes much time and effort, the undeformed tire load treatment is quite easy. Using the given spring rates and the same loading conditions as the deformed tire, the tire deflection in Z is calculated assuming a linear spring for the tire using $F = KX$. In this simplistic representation the side deflection is neglected along with the deformation in Y of both the tire circumference and the contact patch, thus it is only representing the expected loaded radius. The modeling itself is done by mating a plane in the calculated location to the assembly ground plane. This brings the tire to the desired Z height while maintaining all other properties. The CFD domain then treats the contact patch as a non-sliding region that is not subjected to airflow. While clearly there is some level of slip between the tire and the road, as this is the mechanism for tire traction force generation, the free rolling baseline leads to this being neglectable, as free rolling is a

state without longitudinal force generation thus no slip. In that case, modeling the contact patch as a plane traveling at the same velocity as the road is the correct approach. Once the entire matrix of conditions was simulated and modeled, it was possible to asses the severity of deformation in each principal direction as load increases as well as slip angle. While

LR	X Max	X Min	Y Max	Y Min	Z Max	Z Min
6	252.389	-253.603	109.118	-132.683	262.73	-240.753
4	252.454	-253.609	110.347	-130.871	262.855	-241.187
2	252.681	-253.59	113.802	-125.463	263.049	-241.737

Figure 2.12. LR Tire minimum/maximum dimensions

LF	X Max	X Min	Y Max	Y Min	Z Max	Z Min
6	252.606	-253.732	109.653	-130.662	262.798	-242.244
4	252.656	-253.742	110.832	-128.958	262.902	-242.585
2	252.851	-253.719	114.08	-124.22	263.061	-243.031

Figure 2.13. LF Tire minimum/maximum dimensions

X dimensions are, for the most part, maintained throughout the test range due to the free rolling condition, the Z dimension is dependent on loading condition as expected. The added load for the LR case shown compared to the LF case suggests that an increase of 400 [N] leads to a Z deformation of 1.4 [mm] at every slip angle, and since it is assumed that this loading graph is linear, the values can be extrapolated to all conditions for a single inflation pressure. The Y deformation is the most significant one, it increases significantly as slip angle is added: once the angle increases, the max Y deformation increases in a milder fashion as the initial Y shift from straight rolling to 2 degrees for the LR case showed 8 [mm] increase, while the difference from 2 to 4 degrees slip is reduced to 5.4 [mm]. The last step between 4 to 6 degrees shows only a 1.8 [mm] increase, suggesting that the decision to limit the slip angle at 6 was the correct one as the deformation does not appear to be increasing further. Overall, from a forward rolling tire to a steered tire at 6 degrees of slip the maximum Y deformation was recorded as 16 [mm] under the tested conditions. It can also be inferred that the reaction to slip angle in deformation terms is similar between LF and LR cases, showing low sensitivity to load with higher dependency on slip angle. Further examining the data, the free radius is largely maintained, as the tire must deform under loading in addition

to the fixed X dimension due to free rolling condition, it can be understood that the only degree of freedom left is the Y direction, thus it experiences the largest change in dimension.

3. CFD MODEL GENERATION

3.1 Model generation and setup

The CFD code used for this study is provided by "TotalSim" and is an "OpenFOAM" code. This has been the main tool for aerodynamics development of this vehicle for quite some time, thus it was decided to use this code as to ensure values are within a known margin.

The analysis is a "RANS" one using the K-ω SST turbulence model. While it was documented in most of the recent work done on tire and wheel aerodynamics that this problem is a transient one thus requires and unsteady or time dependent analysis such as URANS or LES [9] [15], the computational time involved with those methods along with the new meshing and verification process for a new code would make this study impossible to finish within the time frame. Thus, it was decided to make use of the current computational resources, acknowledging that some of the unsteadiness will be left uncaptured, along with some absolute numbers deviation from real world data, due to the inability to capture some of the vortices as previously described [10] Yet, this is less of an issue in this study as the work done on this field was either for open wheel cars or simplified tire models [16], with the former presenting a completely different flow field around the tires and the latter introduced vortices that might not exists on an actual tire due to increased curvature as the deformation increases. The study was conducted on a sharp edge cylindrical tire that differs greatly from the tested geometry in this case. Moreover, the vehicle is yet to be manufactured thus full-scale verification is not yet possible. In addition, while the absolute values might defer from real data or unsteady analysis data, the relative trends should remain the same thus tracking the trends in both forces and wake generation are more important than the headline numbers. The use of the K-ω SST model here incorporated with a highly refined mesh around the tires and the contact patch is assumed to be able to capture the tires effect on aerodynamics in the most accurate fashion, as this turbulence model is most accurate RANS model for near wall treatment. Once it moves away from the wall towards the upper level of the boundary layer, the model shifts to a k epsilon model which better represents free stream flows, thus

in theory this is the most adequate RANS model to capture the tires effect as both the wall is well represented as well as the detached flow.

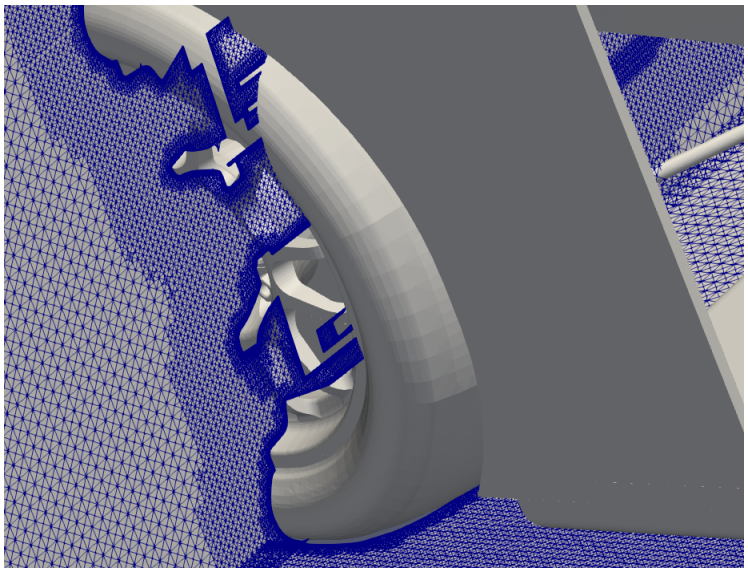

Figure 3.1. Tire assembly mesh

To improve accuracy of the rotating tire, the approach shown in 3,4 has been used. This approach is to use a MRF zone for the tires and the wheels. This essentially assigns rotational velocity to the nodes in the MRF region according to the specified position of the tire [17], in this case each tire has a different rotational velocity as each tire is loaded with a different load case. Extreme refinement was given for both the contact patch and the wheels

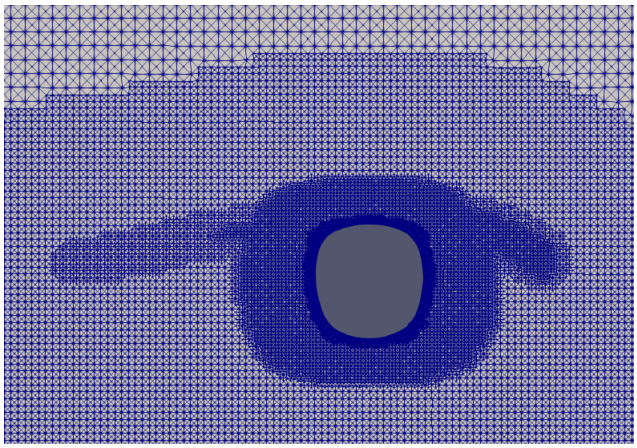

Figure 3.2. Contact patch mesh

themselves. In addition, 3 refinement regions were added on top of the fine mesh around the car to capture the wake from the tires, wake of the car towards the back and the side wake of the car. Outside of those refinement regions, a large domain was constructed using relatively large cells, as to make sure that no interruptions are present due to wall interaction along with some computational resources relief

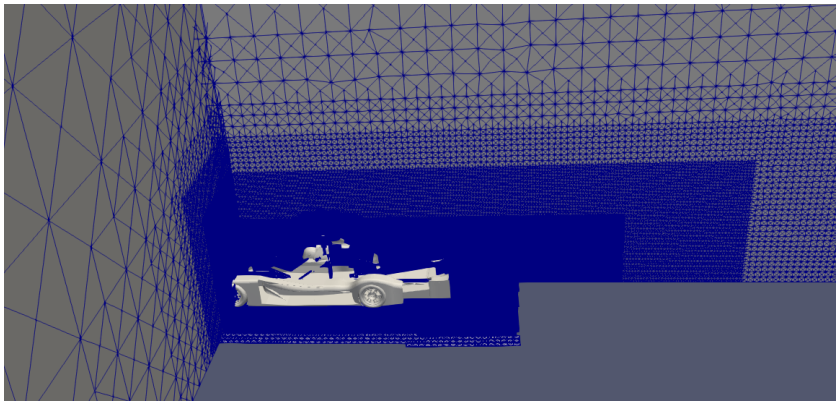

Figure 3.3. Centerline mesh

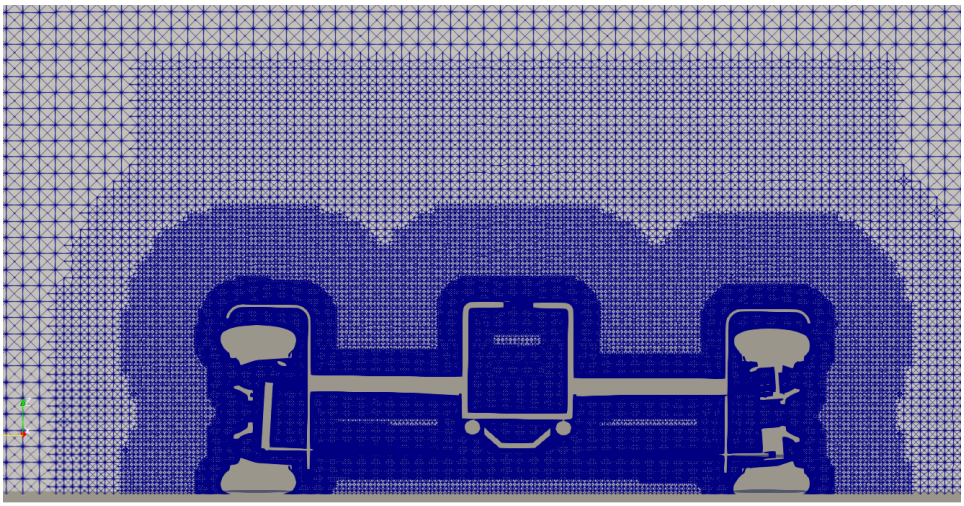

Figure 3.4. X plane mesh

Inlet velocity was set at 44.7 m/s which is equivalent to 100 mph, results were then scaled up using coefficients for Cx,Cz,Cs. Since this study involved yawed flow, the inlet also had a velocity in the y direction, while the outer wall was set with the same conditions as yawing the flow introduces air coming in from the side. Outlet in X and y were set to

pressure outlets as they are far away from the model where flow is assumed to settle back to atmospheric conditions. Upper wall was given a stationary wall with slip condition as

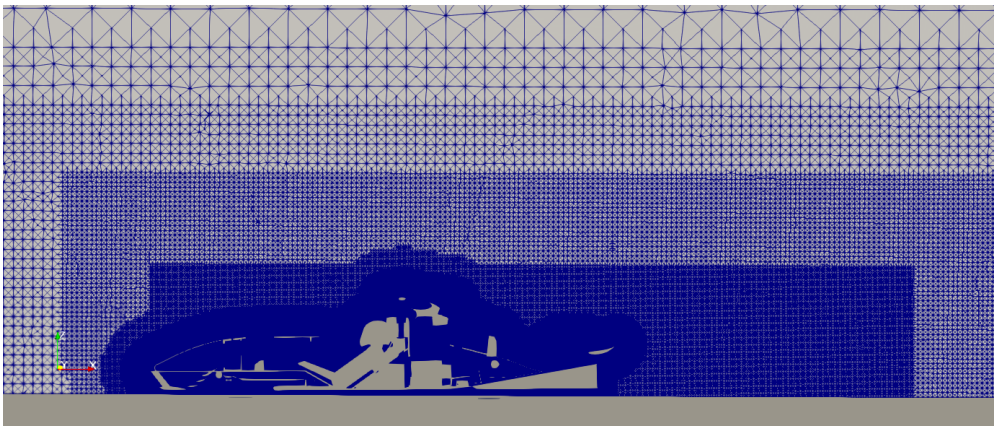

Figure 3.5. Y plane mesh

to avoid shear forces prediction on the wall, while the road was described as a moving wall traveling under the same velocity conditions as the inlet. Lastly, the car was modeled as a non-slip stationary wall, while the wheels were given the rotational velocity that correlated to the SLR. No slip was assumed at the contact patch thus the forward velocity of each wheel matches the forward velocity of the ground. For curved domain cases, the same mesh refinements were given, yet a curved structure was formed maintaining the wake refinement along the centerline of the curved domain. Since it was decided to maintain the onset flow angle relative to the centerline, in order to determine the change in yaw along the car, the boundary conditions for the curved case deferred from the straight line and were a more conventional setup, where the Y direction walls were modeled as slip walls with zero gradient, as was the case for the top wall [18]. Inlet was given in terms of rotational velocity as this analysis is done using an SRF approach. The SRF is a single rotating frame which essentially means the car is maintained at a position in space and the domain is rotating about the center axis. It is important to note that the mesh is not physically rotating rather it just has a rotational velocity, the mesh itself is fixed in space. This approach models a steady state solution, thus is compatible with the assumptions taken under this study for steady state cornering. The inlet velocity is determined by the distance from centerline and the rotational velocity of the domain. These were set for 100 m radius turn with an Ω of 0.447

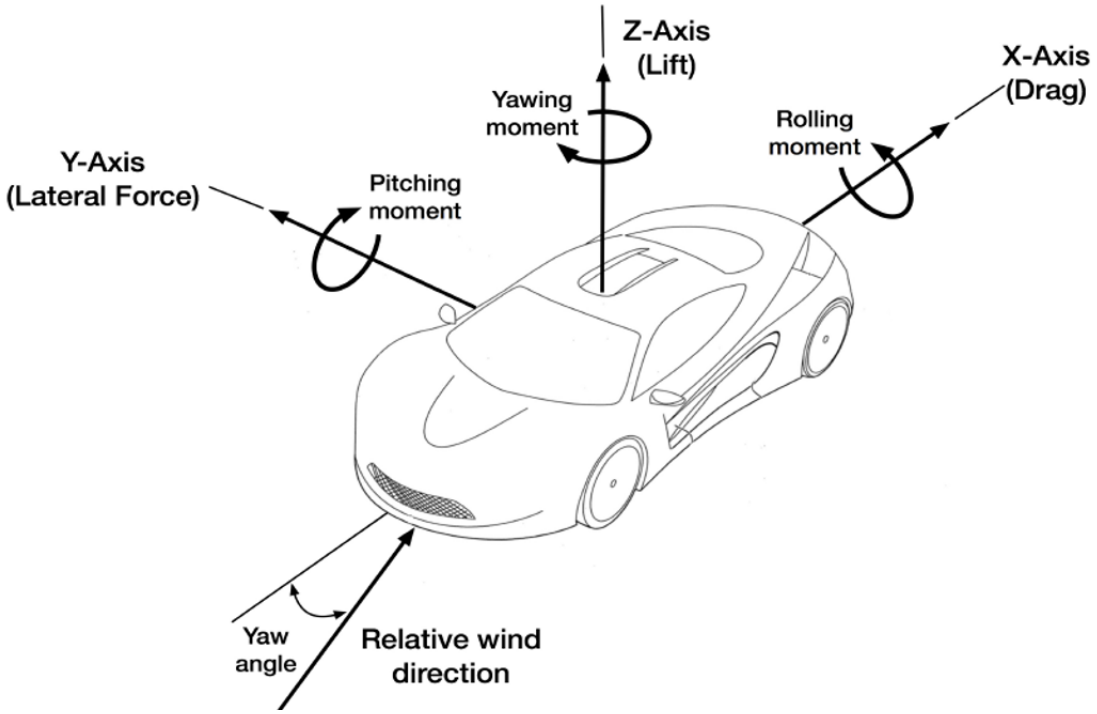

Figure 3.6. Coordinate system

and an axis of rotation pointing along the Z axis. This setup produces a domain that has a varying rotational velocity from inner Y wall to the outer one, with the centerline presenting the forward velocity of the vehicle. The curved domain setup determines that the flow along the car will change direction from side to side in a more realistic fashion than a complete yawed flow case, where the artificial yaw is applied in a similar manner to the entire length of the car.

3.2 Preliminary study

Prior to the deformed vs rigid tire study, an initial study was conducted to understand and quantify the performance of the car under yaw and steer variations. This was done to evaluate the vehicles sensitivity to steer and yaw, define which aspect effect the car the most and if the simulation set up provides for logical numbers, as correlation to WT was not possible due to financial and design constraints. A matrix consistent of 4 yaw and steer sweeps was assembled using 0, 2, 4, 6 angles for both steer and yaw. This matrix assisted

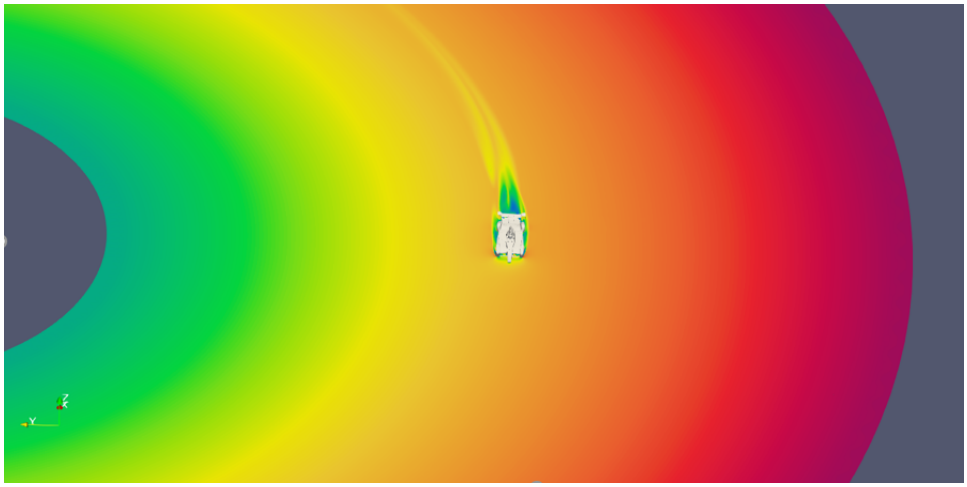

Figure 3.7. Curved Domain Rotational velocity

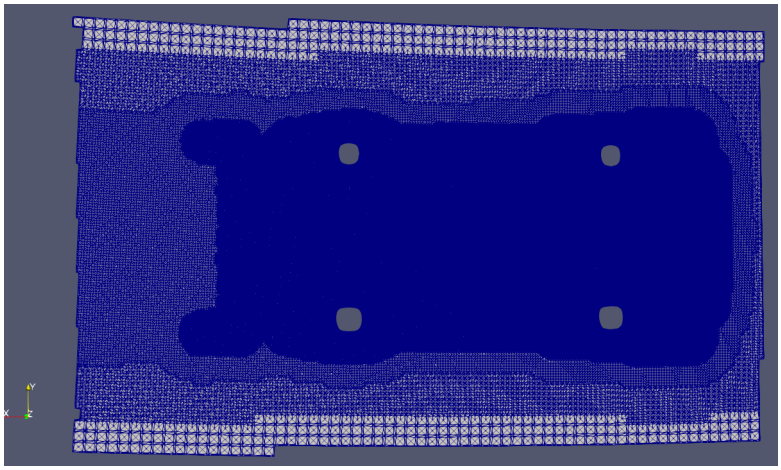

Figure 3.8. Z plane curved domain mesh

with determining the most critical data points for cornering along with understanding which areas are most effected by the flow angles. In addition, a 6-degree increment yaw sweep was conducted to zoom in on any in between effects on aerodynamics. A mesh study was performed increasing biased mesh refinements in the direction of yaw. This study yielded the final mesh set up that was later used with the same boundary conditions in this tire deformation study. The results of the preliminary study suggested that no major sensitivities were found for downforce or drag due to yaw and steer. Both were shed as cornering angle increased with the main effected component being the FW. The side force generation did however show sensitivity to yaw angle with a linear trend showing a steady increase of 50

[N] as yaw is increased with complete indifference to steer changes. Using these trends as a guideline for this study will ensure that results are consistent in both values and flow behavior.

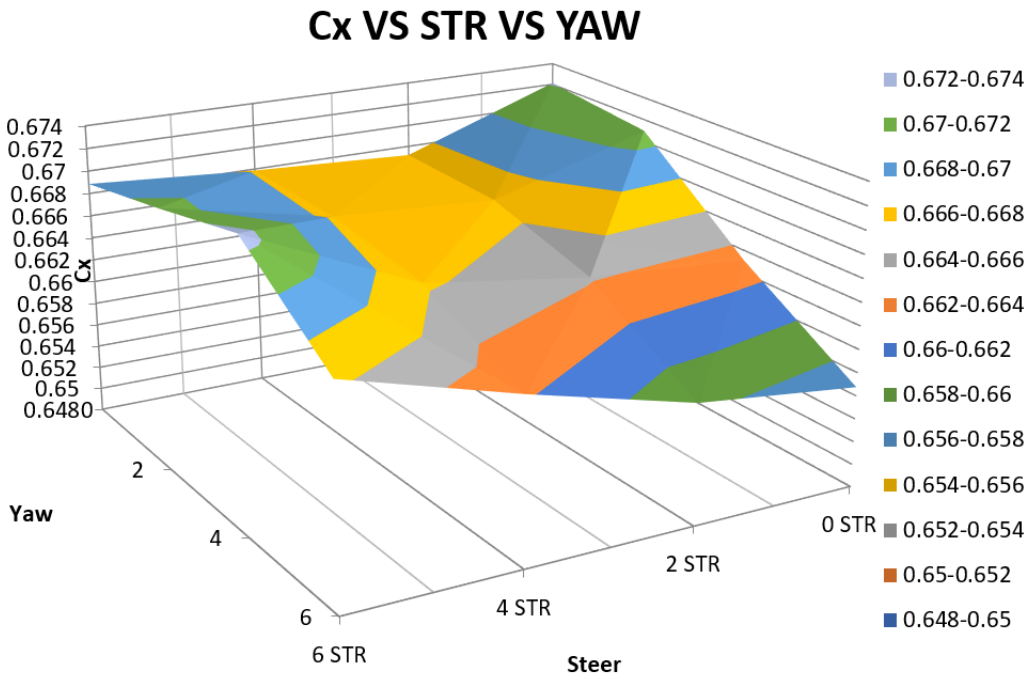

Figure 3.9. Cx VS STR VS YAW

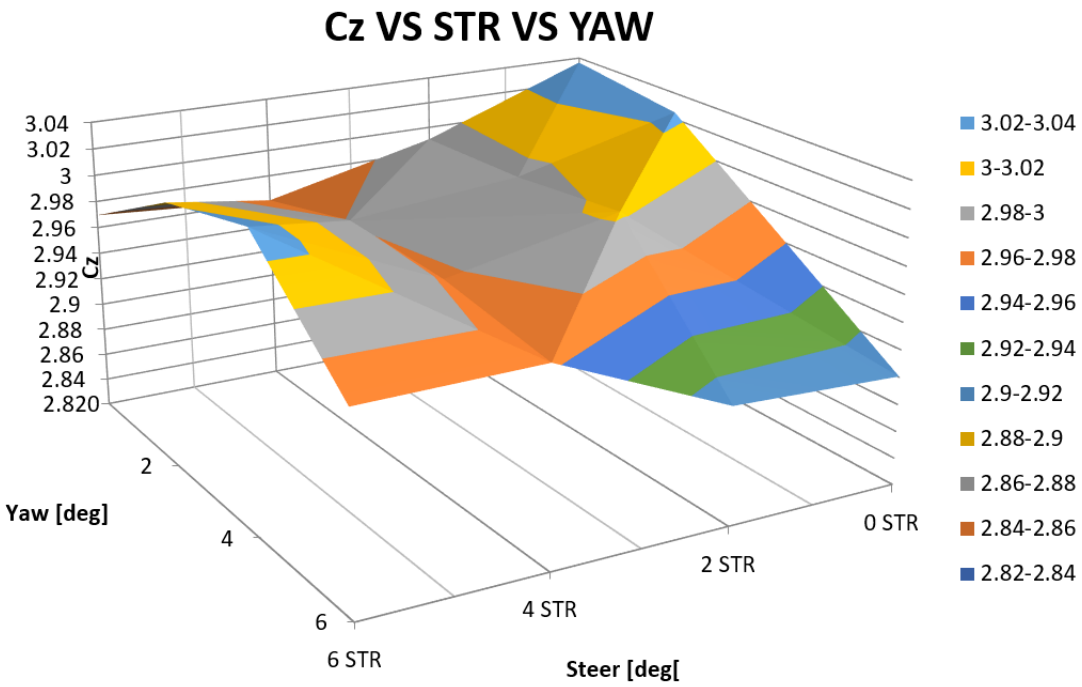

Figure 3.10. Cz VS STR VS YAW

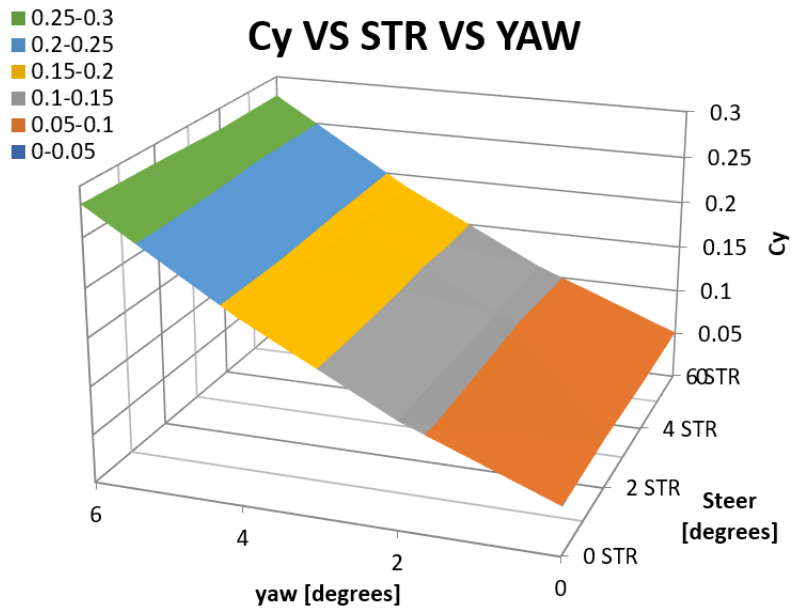

Figure 3.11. Cs VS STR VS YAW

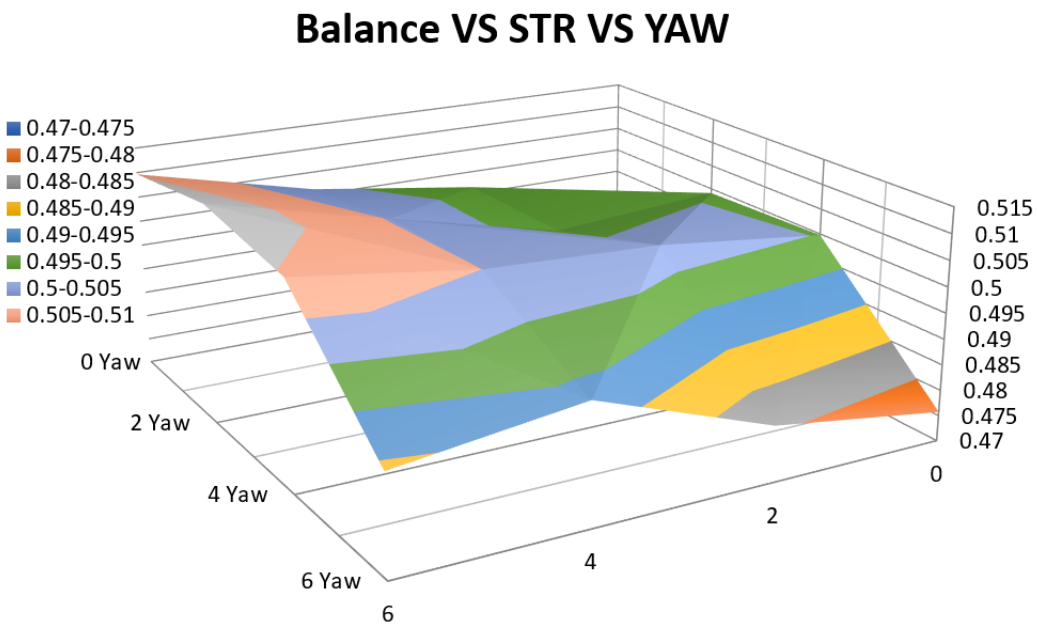

Figure 3.12. Balance VS STR VS YAW

4. RESULTS AND DISCUSSION

4.1 Straight-line analysis

The first segment of this study was the comparison between flow in a straight-line case of both rigid and deformed tires. When a race car goes through a course it has a wide variety of front and rear ride height changes. Usually, a single front and rear RH is used to specify a certain position in the course, for example, in this case 13/07 mm is the RH for the EOS case and 38/63 mm is the RH for the cornering position. To evaluate whether the tire modelling has an effect during simple straight-line analysis both end positions were modeled where the loads acting on the tires were extrapolated from the large data runs of the preliminary study.

Initially one can immediately see the difference between modeled and rigid tires. Both modeled cases present higher Downforce numbers along with a drag force and balance change. One must keep in mind that while the rigid tire FP position is calculated from spring rates, the modeled tire is allowed to deflect under the given load freely and to reach its final shape according to the FEA model. This difference between the two creates a few distinctions

1. Tire dimensions – while the rigid tires dimensions were modeled according to the tires naming convention (width and diameter), the deformed tires dimensions are now a factor of tire pressure and are not constant along the surface rather follow the tires curvature in each part of the cross section. This results with two different widths and diameters showing a larger diameter and width for the modeled tire compared with the rigid tire. In addition, the loaded side of the tire has a different shape than the unloaded top part of it, in contrast to the rigid tire where the SW and tread shape is maintained throughout.

2. Contact patch shape – since the rigid tire is cut by the bottom wall of the domain i.e. the road, its contact patch shape is just the plane at a given RH resulting with a rectangular FP shape that spans all along the width and length of the cutting plane, whilst the modeled tire is given another degree of freedom to obtain a more realistic oval contact patch shape that does not span for the entire width unless a severe loading condition is given.

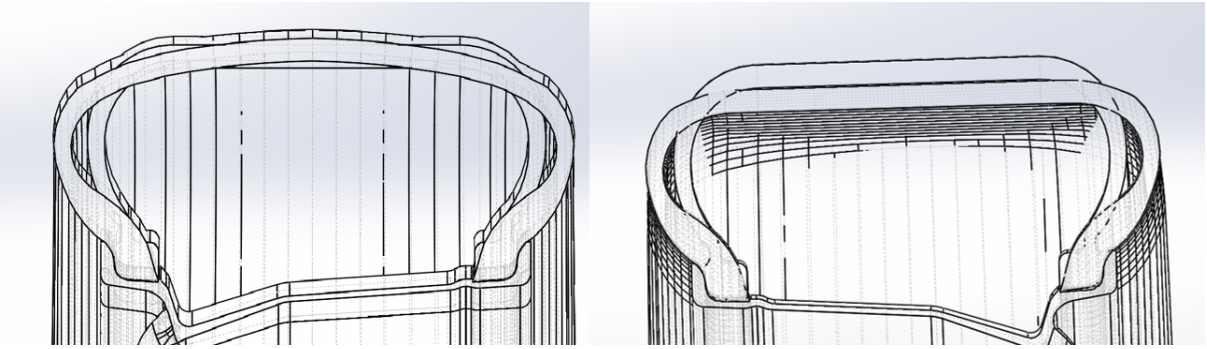

Figure 4.1. Loaded VS unloaded cross section of both models

3. Each tire has its own rotational velocity, and since it was shown before that the dimensions differs at each wheel, it implies that the rotational velocity must change as well, creating another distinction between the cases.

Looking at the End of Straight RH, a slight difference in results can be noted as the deformed model gains 50[N] of DF along with 13[N] of drag to obtain a 10-point increase in drag coefficient and 38 point increase in DF coefficient. While it is clear that the modeled tire has an effect on the result, it is now needed to zoom in on each section and understand where the effects lay. Here it is clear that the realistic contact patch shape has an effect on the flow

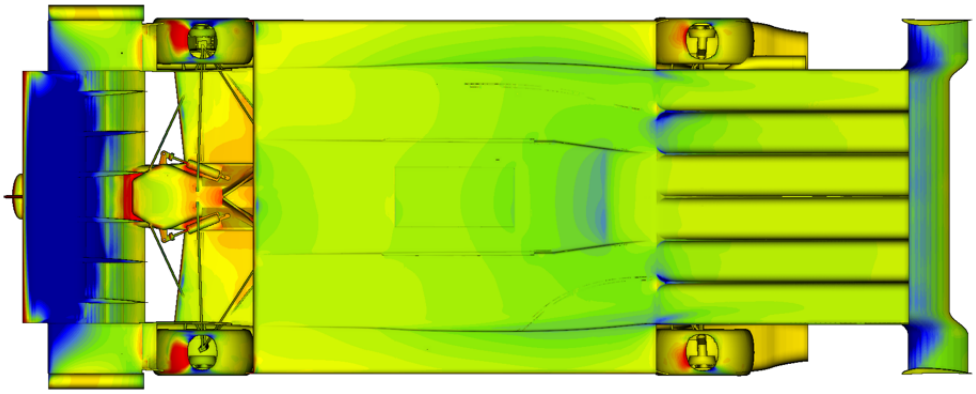

Figure 4.2. Deformed model body pressure contours EOS

along the vehicle. Since only part of the tire is in contact with the road, there is a funnel like

shape in the X-Z plan creating low pressure at the sides of the CP. This is more pronounced at the front than at the rear due to high Cpt oncoming flow, along with a big underfloor directing air underneath it, while the rear wheels are left with slow moving air. This local low-pressure peak helps removing some of the wheel lift created by the rotational movement of the tire. This also allows for higher velocity air to enter the underfloor area increasing its efficiency. Wheel lift is commonly generated from the stagnation point at the front of the contact patch, creating a high-pressure zone in front and below the tire horizontal centerline, which pushes the tire up. Observing the rigid tires contact patches it is possible to see this high pressure forming at the front of the contact patch, generating that lift as the contact patch in this model, is very wide and perpendicular to the flow direction. The combination of the two accounts for a significant pressure gradient that produces large lift forces on the tires. On the other hand, since the shape of the contact patch in the deformed tire is more realistic

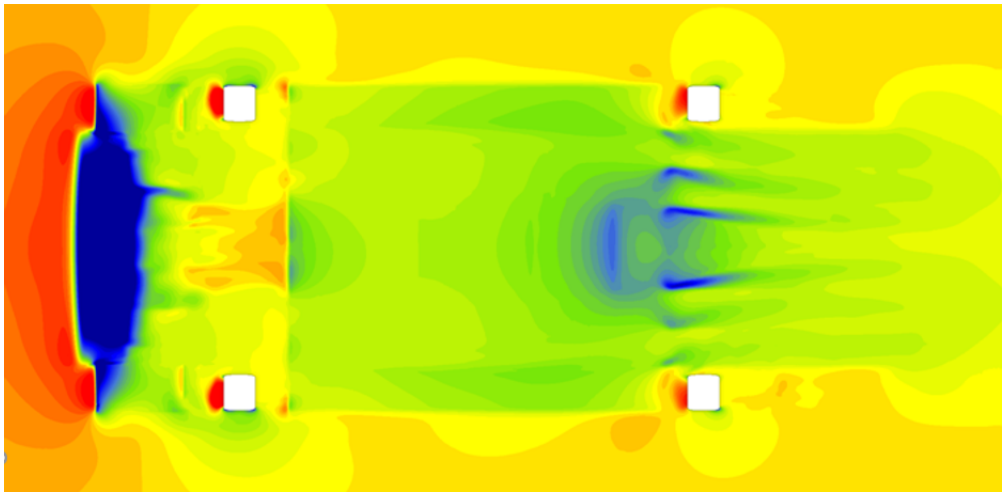

Figure 4.3. Rigid model pressure contours EOS

and resembles an oval, it produces a lower pressure peak as flow stagnation is localized to the center of the contact patch. In addition, the patches shape induces acceleration along the sides of the tires contact with the ground, thus reducing overall pressure build up and the lift force that follows. The reduced wheel lift was evident in every comparison between deformed and rigid tire thus strengthening the case this phenomenon has a clear repeatable trend. This showed that wheel lift is sensitive to rigid/deformed tire model. At the same

time, the drag addition was very much pronounced as well showing 150-200% increase in wheel drag due to deformation modeling. This effect has less to do with the contact patch or the shape of it rather it is more dependent on the actual final dimensions of the tire being more realistic in the deformed model. It is clear then that including deformation, even at straight ahead conditions, has a significant and clear effect on the aerodynamics of a car. Examining the effect during a cornering maneuver will determine the importance of including this deformation modeling along with understanding how does it effect the flow field.

4.2 Cornering analysis - Yawed Flow Domain

Once the tire modeling contribution was tested on a straight-line condition and showed relevance to modeling accuracy, the next phase of the study was to perform the same analysis on a vehicle at mid corner conditions. This was done by calculating the roll angle and resulting weight shift along with extrapolated initial DF values from the big data runs. All of which resulted with four different tire models for each wheel position. To this weight shift a slip angle was added at two-degree increment (2, 4, 6) to account for both the lateral displacement of the contact patch in the Y direction along with the whole tire deformation in the Y direction that is a resultant of the contact patch shift. Each combination was given a yaw angle equal to the steer angle in order to simulate a wind tunnel cornering condition test, where the air flow is approaching the vehicle at a yaw angle equal to the rear wheel slip angle. This adds a level of complexity to the model but enables the understanding of the modeling importance to accurately predicting the correct values. Placing both models next to each other provides a visual understanding of the tire deformation contribution to the effects on the airflow field. There is a significant change in pressure build up at all directions of the tire as the tire shape is more realistic. The contact patch has a true oval shape that moves about the Y direction while cornering, and the weight shift effect from the inner tire is much more pronounced in the modeled tire, as its CP is smaller and allows for air to flow beneath it. Observing the force data gathered it can clearly be concluded that the deformed model has a significant effect on the flow field. at every instance the deformed

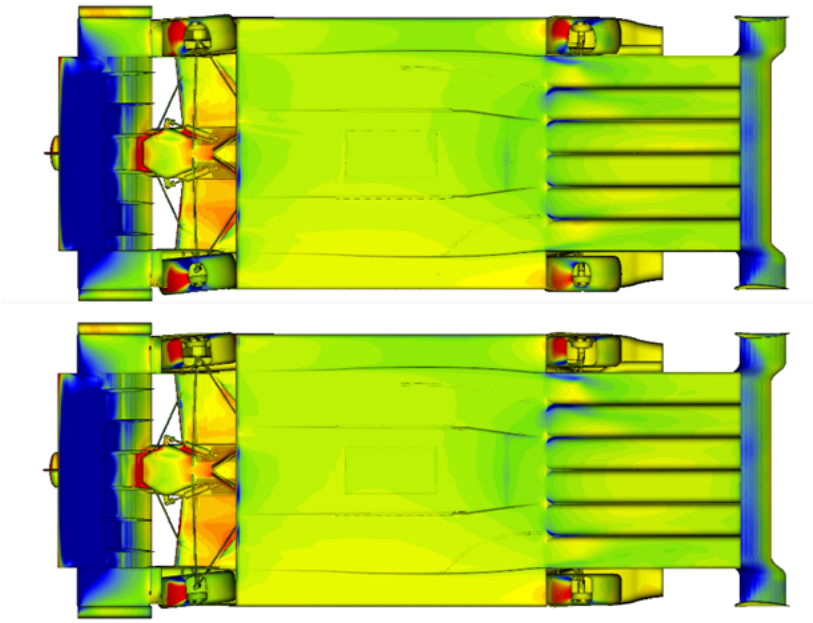

Figure 4.4. Rigid VS Deformed Body Cp at 6 STR/YAW

tire produces more downforce than its rigid counterpart, and while this increase starts to drop off after 4 degree of yaw and steer, it is incredibly significant at the lower angles as it reaches a full 225 points of Cz increase along with a very high 14 points of Cx increase. This results in a single run L/D of 4.692 compared to the mere 4.451 of the rigid tire. That difference in L/D shows that including tire deformation in the analysis actually efficiently increases the prediction of downforce generated by the car. It appears as if the drag addition is solely due to the wheels, the only component that experiences a significant change in drag are the wheels. It can be seen that the increased width exposes more of the front wheel to oncoming flow, thus the stagnation pressure acts on a larger area increasing the force on the wheel. In addition, the rear wheel faces the same issue, also increasing the drag force on the wheel. This phenomena is evident on every wheel yet its most pronounced on the outer wheels. It can also be inferred that this increase in wheel drag has relieved some of the drag generated by the body as, again, the larger frontal area of the tire relieves some of the pressure acting on the body. A common result in all deformed tires runs was the increased DF at the front diffuser or front wing. This increase ranges from 20 [N] at the

straight-line cases to 140 [N] at the cornering condition. By looking at the contact patch one can visualize what causes this increase. Observing the inner tire (RHS), the deformed

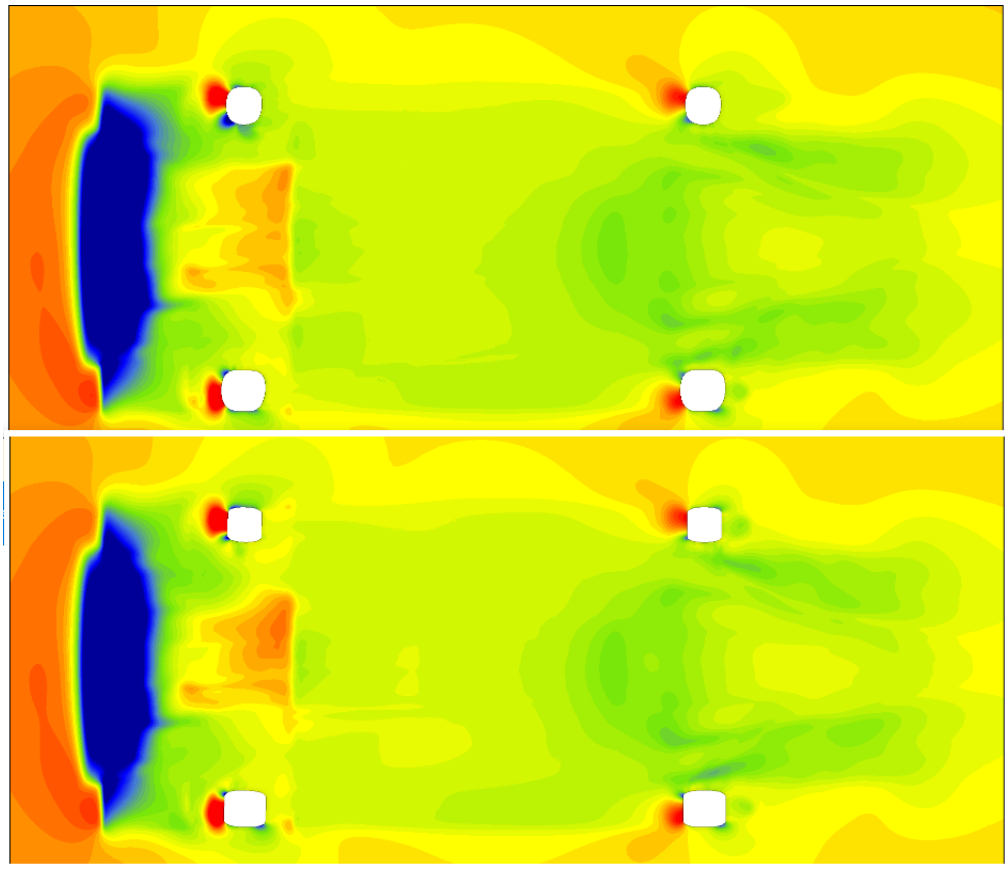

Figure 4.5. Rigid VS Deformed Z pressure contours 2 STR/YAW

tire causes an increased magnitude of high-pressure flow in front of it, due to a narrower FP, and shifted center position caused by the slip angle. At the same time, the narrower FP also creates a suction pocket underneath the inner side of the tire, thus creating a high to low pressure path that increases the size and magnitude of the front diffuser pressure peak and creates more downforce. On the outer tire, it is possible to notice the same effect yet to a lesser extent as the Y direction shift is towards the centerline of the vehicle, thus the tire is pressed harder against the ground at that position, as opposed to the inner tire that experiences reduced load towards the centerline of the vehicle. It does show an increase in suction yet not as pronounced as the inner tire. The combination of the two increases the suction which has a downstream effect on the underfloor increasing its downforce as

well. The effect on the front diffuser is more powerful than the underfloor effect causing a forward's shift in balance, increasing the load on the front by up to 3% more than the rigid tire. This feature is common to both front and rear wheels, yet at the front the pressure difference created by the tire is much greater. This effect is not just local to the contact

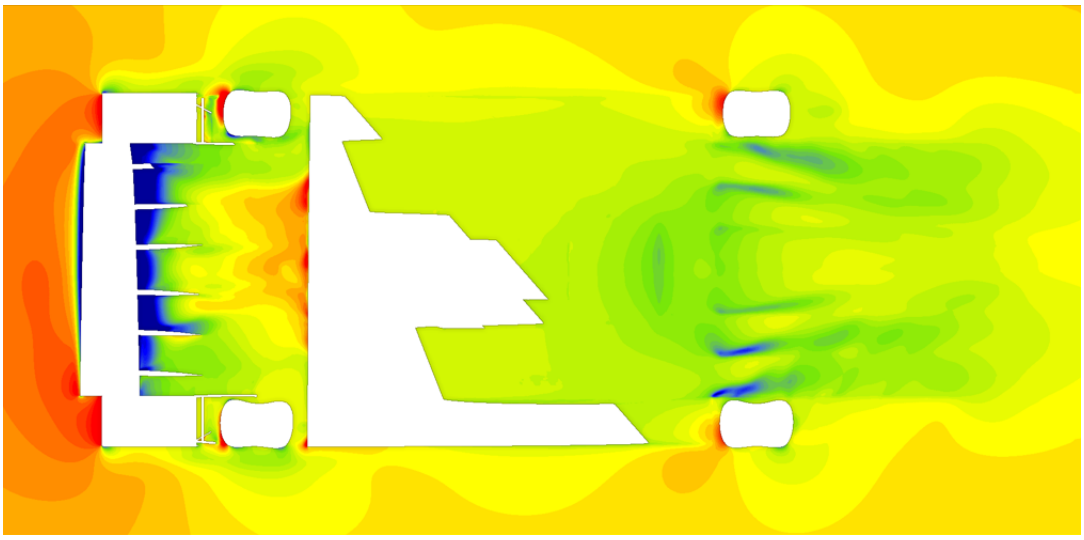

Figure 4.6. Deformed Z pressure 5 cm off ground

patch, as the pressure difference is still maintained up to 5 cm above ground. This increases the low-pressure zone below the airfoils of the FW and increasing the high pressure above them, as mass flow is directed below the airfoils due to the increased suction. This in turn increases the pressure atop the body producing lower body lift compared to the rigid tire. Another way to look at this result is the induced drag increase at the front wing along with

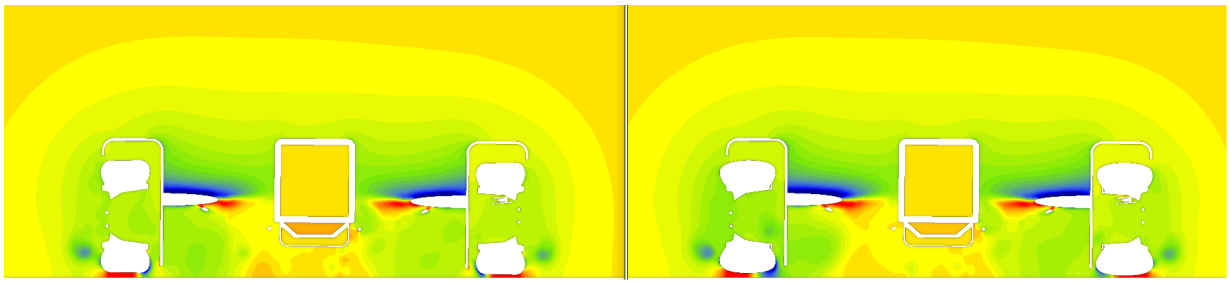

Figure 4.7. Rigid VS Deformed X Pressure contours

the downforce increase, suggests that the tire deformation increases the attached span of the

front wing. Observing a cut X-Z plane local to the increased low-pressure zone, it can be seen that the slight separation visible at the rigid tire model is no longer evident at the deformed model cut section due to that low pressure peak. This alone shows that tire deformation is an integral part of the vehicle's behavior during a run, as it presents effects up and down stream that influences every aspect of the vehicle. Once this phenome has been identified,

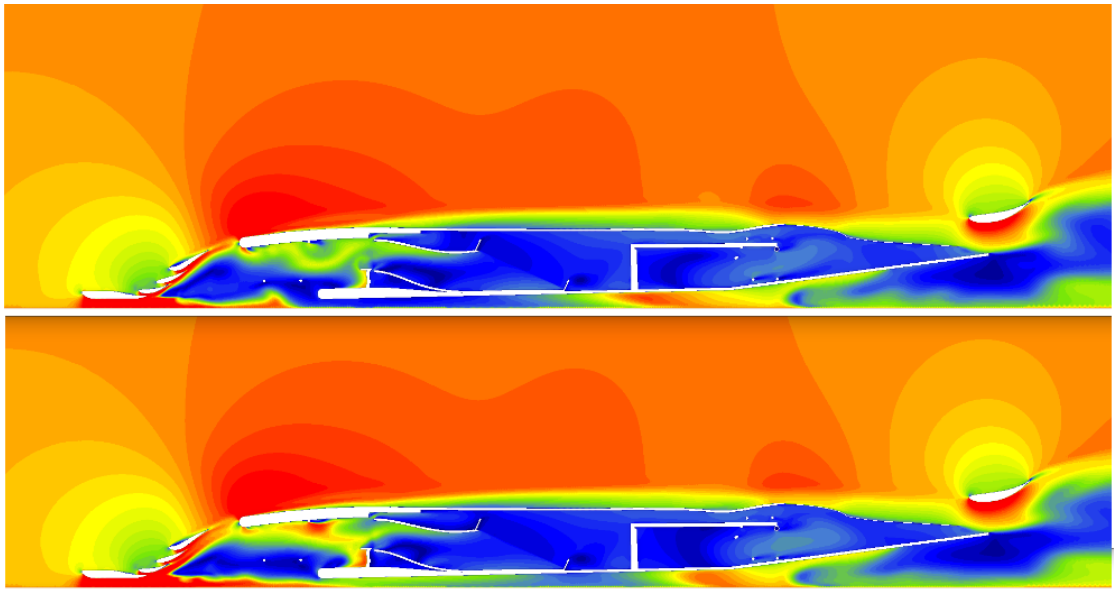

Figure 4.8. Rigid VS Deformed Y Velocity contours

one can assume that at higher steer angles the effect will only magnify as the contact patch center of pressure shifts even more towards the corner, thus the portion of the contact patch closer to the vehicle centerline is elevated compared to the lower steered model. Yet, from the force data this delta is reducing as the Steer/Yaw is increased, it will later be shown that this conflict is due to the higher yaw of the wind by comparing between 6 steer and 2 steer configurations at a curved domain flow without any artificial yaw. Examining the pressure contours in the X-Z plane, it is possible to note that same low-pressure zone underneath the front diffuser spanning further back, thus increasing front DF. While the area around the deformed wheel experiences lower pressure compared to the rigid tire which in turn reduces body lift. While it is clear that tire deformation modeling has an impact on both downforce and drag prediction, as well as the force distribution, it is yet to be concluded whether this approach has an effect on side force prediction. Force data from the performed study shows

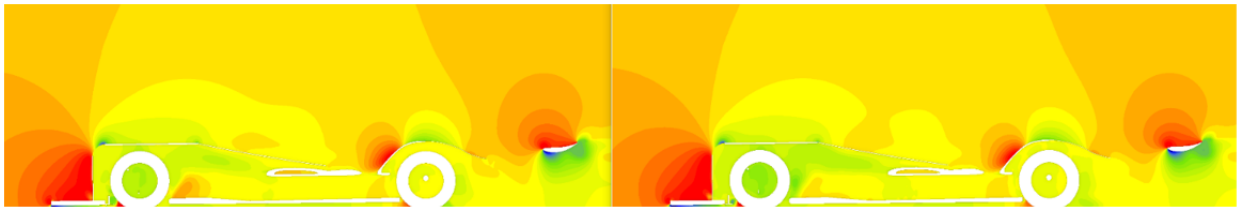

Figure 4.9. Rigid VS Deformed Y Pressure contours

that performing an analysis using the rigid tire model has the tendency to over-predict the side force generated by up to 12 points, which translates to a mere 15 [N] or 5% of the overall side force generated. Thus concluding that the effect on side force generation using the straight domain approach is of lesser magnitude than the relatively significant effect tire deformation modeling has on drag, downforce and balance. Dissecting each development area, one can see that while tire deformation modeling has proven to have a significant effect on the front DF of the vehicle, along with some contribution to underfloor, wheel and body lift predictions, it showed little to no effect on the rear wing. This can be attributed to the large distance between the rear wheels and the rear wing, along with the distinction between front and rear wheels. This distinction implies that the front wheels are more sensitive to the modeling approach, as they interact with oncoming freestream air rather than the rear which interacts with flow that converges into the diffuser along with yawed flow from the cornering condition. This in turn renders them indifferent to the tire modeling method. Comparing this effect with a curved flow case will assist with determining the importance of rear tire modeling, as it will be possible to understand if the cornering condition is the limiting factor or is the vehicle construction the limiting factor. As was described earlier, the deformed tire model has yielded more realistic dimension in both cross section and overall width and diameter. These values are extremely important when designing the body work, specifically the wheel wells and the surrounding area. Aside from the obvious fact that the opening must be large enough to contain the tire, using this model for further development is of great importance. Since most of the aerodynamics development work on a car is based off of the Bernoulli principal, clearances and the pressure change created by them are a tool to manage and condition the flow according to the desired force generation. An example can

be made for the design of an oval circuit car. Since these races are conducted at high banking angles and high velocity, a very common method to increase the cornering ability of a car is generating side force through body work. While it is possible currently to design an aero component that will generate side force in the desired location, using the suction behind the rear wheels, it is currently very difficult to understand whether or not a passage that small might close up during an actual corner. As was described above, during a corner the center of the contact patch shifts towards the corner, and with it the entire tire experiences a large deformation in the Y direction. Specifically, for this tire the centerline of the tire can shift up to 1" under heavy cornering conditions. This in turn can result in complete blockage of the wheel well opening up to the point of contact with the body work. While this effect can negate some of the development work done to capitalize on the wheel well suction, it can also be used as a tool for the creation of a dynamic mechanism that produces high side force values during cornering where the blockage is increased at the inner tire and decreased at the outer tire. Using that knowledge, one can create a geometry that during a straight line increases suction and thus higher Cpt values to the underside of the vehicle resulting in lower drag (smaller wake). Yet at the same time, also capitalizes on the blockage change left to right so that on the inner side of the body higher velocity flow would be present, while on the outer side higher pressure due to increased clearance to the underbody resulting with an airfoil effect generating side force pushing towards the corner. Trying to do so without lateral tire deformation would result in an unrealistic effect that while is completely reproducible in wind tunnel testing, it is unrepresented in a real world - full track testing as the wind tunnel cannot handle large tire deformation. To put this in simple terms, developing and area that changes during a corner without taking into account that change, is similar to examining the flow field of a car using one RH for all conditions. It cannot represent the change in the flow behavior just as a nose down cornering RH cannot represent a nose up end of straight condition. It is thus shown that the geometric contribution alone can have a significant effect while it can also be used as an aerodynamic device by itself to generate or negate the specific force desired.

Examining the force results, it is possible to see some trends showing the contribution tire modeling has on each quantifiable aspect of the flow field. Plotting the downforce coefficient

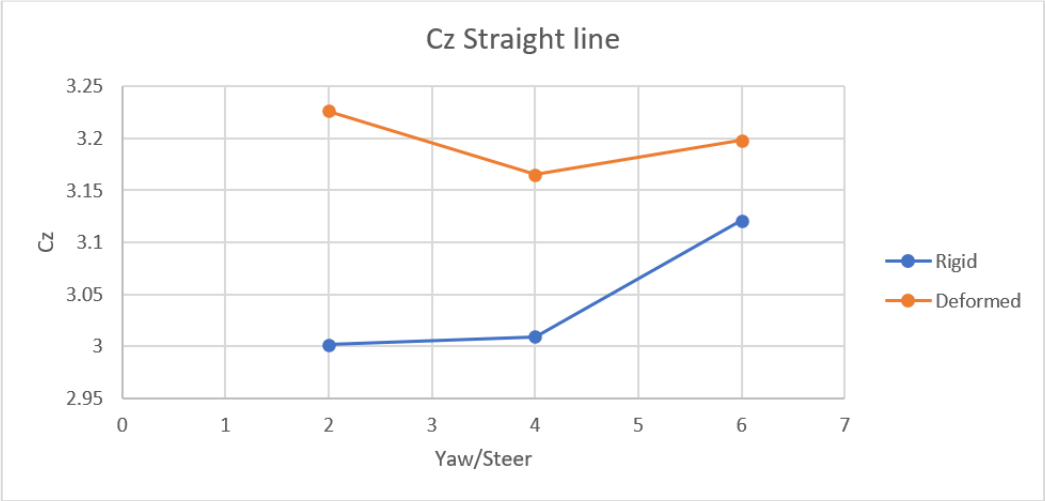

Figure 4.10. Rigid VS Deformed yawed flow domain Cz

as a function of flow angle shows that as the angle increases, the change in downforce compared to a rigid tire decrease. To understand this trend, it is needed to dive into each section of the car and observe its sensitivity to Yaw/Steer angle. Rear wing shows the same trend for both models as it loses downforce due to the yaw angle, yet it experiences little to no effect from the tire wake, as it is shielded by the large diffuser. The wheels themselves show low Cz amplitude as a function of cornering angle in both models. Yet the deformed tire is considered to be more sensitive resulting with a 25[N] amplitude compared to a 3[N] in the rigid tire model, these values are low relative to other development areas. The underfloor presents a similar trend for both methods as it gains downforce with an increase in cornering angle. This is due to the size of the underfloor that enables it to inhale high Cpt flow from its sides resulting with a lower pressure that in turn creates more downforce. Similar values were measured for this section of the car in both models, which hints on model sensitivity to underfloor modeling. This issue is even clearer observing the high cornering angles, in which the suction peak at the diffuser shows the ability to inhale the flow effected from the front tires while increasing its velocity to a point where it is no longer separated. The body presented similar trends to the underfloor as the yawed flow actually relives some of the lift generated due to the flat shape of the body in an offset flow condition. The main difference between rigid model and deformed model with regards to downforce was captured at the

front of the car. Here, the two models presented a trend discrepancy, as the FW of the rigid tire was fairly stable losing only 20[N] of DF during the sweep, while the deformed tire lost more than 100[N]. In addition, as was described above in the straight line condition, there is a highly pronounced FW DF gain while using the deformed model. Combining that with the results from the cornering sweep, it is clear that a change in steer angle results with a lower suction in the front contact patches, which lowers the FW efficiency due to slight separation of the airfoil package. To generalize these conclusions, it is possible to conclude that a deformed tire drastically changes the flow patterns both in front and behind it, while the wake effect can be negated using a large and efficient diffuser. Yet the upstream effect only strengthens when implementing a large suction device at the front such as a front diffuser or a front wing. Using the same conclusions from each development area, the tire effect on aerodynamic balance can be noted. The balance tended to shift backwards in the deformed model, while the rigid model presented the opposite trend. This can be related to the same FW loss the deformed model experiences, which in addition to the increase in UF downforce shifts the balance rearwards. On the other hand, the rigid tire maintains a fairly stable FW with the same trend in UF gain, yet the body lift reduces significantly combined with a RW loss resulting in a forwards shift of aero balance. This conclusion is of great importance as

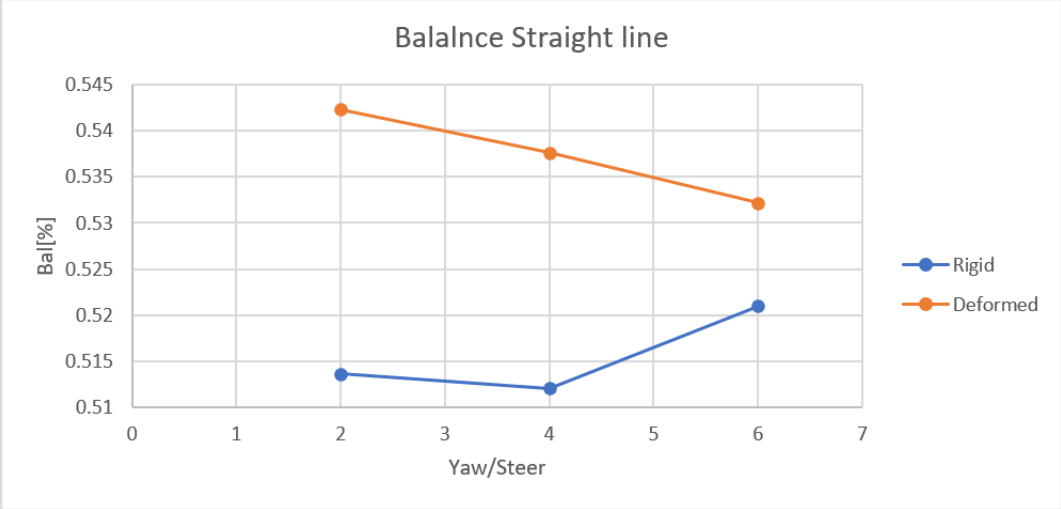

Figure 4.11. Rigid VS Deformed yawed flow domain Balance

it presents the level of complexity the deformed tire model adds to the CFD analysis. The

location of the aero balance is no less important than the force itself. The results of this sweep suggests that the behavior of the car can be completely different when choosing one model over the other. This can result in loss of performance due to incorrect data gathering. While as was stated before, correlation in the WT is important, the end result on the track is the most significant data. Thus, it is possible to understand from these results that further investigation of the deformed model under track conditions is required to validate it as WT cannot correlate these results while the data obtained justifies this investigation. Examining the effect on drag, one can see that the overall drag coefficient is much more sensitive to angle changes in the deformed model than the rigid model. An amplitude of 13 Cx points was recorded as opposed to the 5 points amplitude in the rigid model, this is not only due to the increased size of the tire but also due to a completely different wake region behind the tires. In addition, the Y direction deformation that increases the exposed area for oncoming flow in the X direction, also effecting the increased drag sensitivity. Wheel drag by itself showed higher values, as was expected, for the deformed model, as the tire itself is larger. Yet in an unexpected fashion, it was not sensitive to angle change as there is a clear trade off between front right and rear left wake size during the sweep. The same development areas trends were evident in the rigid tire model, with the exception of body lift, which is completely stable for the deformed model yet fluctuates in the rigid model. The main contribution to the increased drag is the wheel drag, as RW and FW showed little to no drag effect while the underfloor drag was slightly lower in the deformed model. To better understand this phenomenon, a greater test matrix is needed yet the significance it has on the eventual conclusions is to a lesser extent, thus it can be concluded that the deformed model presents higher and stable drag values. The only force data that presented an under-prediction of forces in the deformed model relative to the rigid tire was the side force coefficient. Both models presented the same linear increase in side force with respect to cornering angle, yet the rigid tire model showed slightly sharper slope suggesting that the modeling technique is not sensitive to the cornering angle under straight domain condition, as most of the tire effect is relaxed by the UF and the magnitude of the tire effect is insignificant relative to the other components. In previous work done in this field, most of the focus was on the wake structure and flow patterns around the tires of an open wheeled car, mostly F1 or FSAE [19] [20] [21].

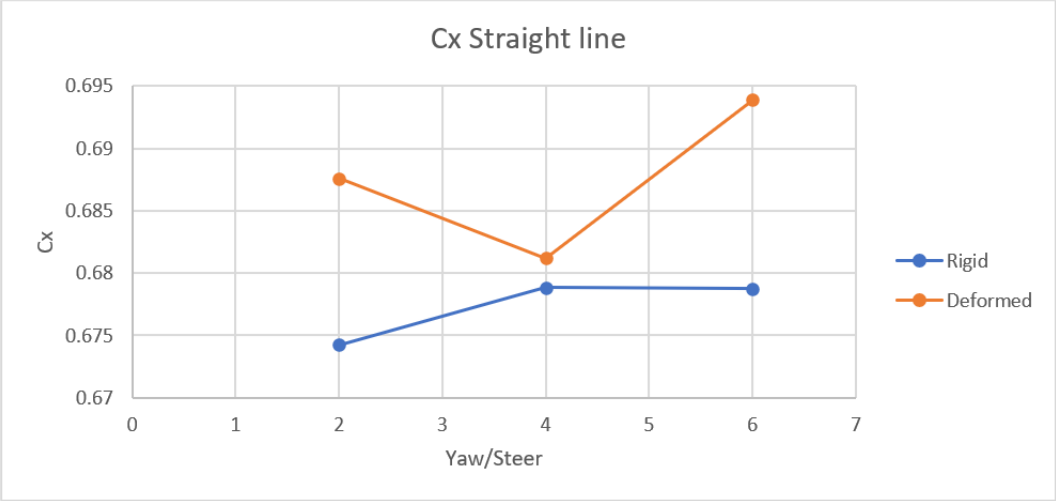

Figure 4.12. Rigid VS Deformed yawed flow domain Cx

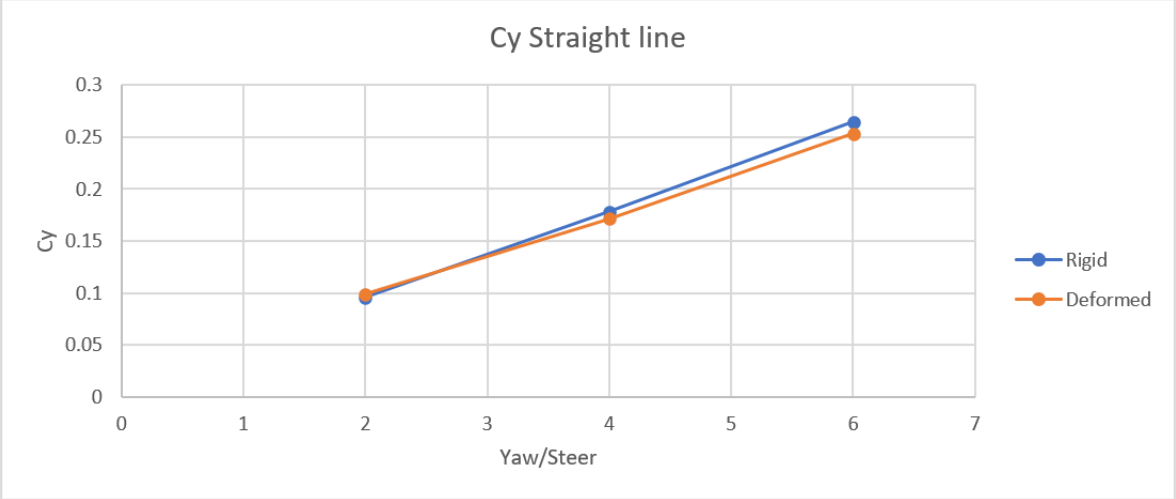

Figure 4.13. Rigid VS Deformed yawed flow domain Cy

The importance of tire deformation under these conditions can be easily understood due to the fact that the tire is a bluff body hanging from the vehicle, and, in addition, it is rotating about 3 axes simultaneously. These features causing the tire to have a significant effect on the flow field around the car, as wake from the tire is dynamic and will adversely affect the aerodynamic performance. Thus, understanding the tire aerodynamics wake behavior is of great importance for open wheel racers. No work could be found up to now on the effect of tires on closed wheel race cars. Some work has been done on passenger cars, yet this was

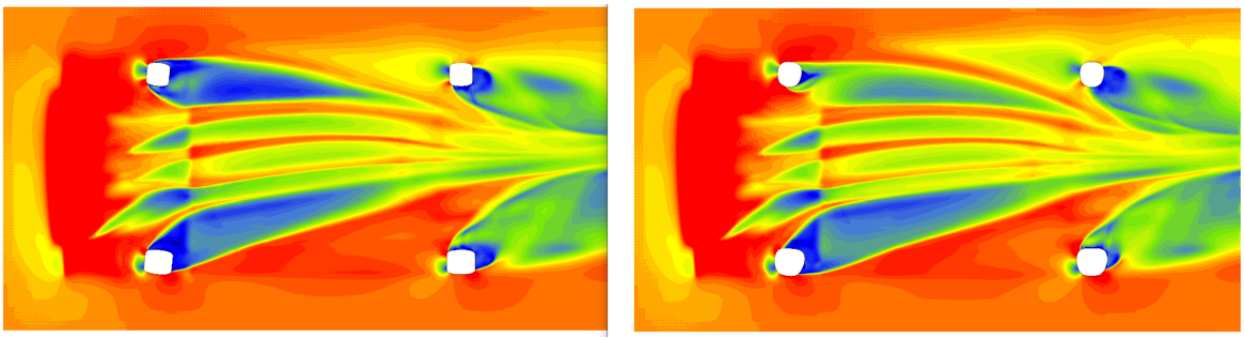

Figure 4.14. Rigid VS Deformed Z Velocity contours

more specific to tread pattern effect or wheel bend construction rather than to deformation. In this specific racing category, the tire is set to have a significant effect even though the car is considered a closed wheels vehicle. It is built in such a manner that the wheel is fully enclosed within the wheel well, yet the well is exposed to both X and Y direction flow while the rear end of the wheel well is fully uncovered in the X direction, allowing for flow coming off the tires to have an effect downstream on the rest of the car. In a similar manner, the rear wheels are also built under the same bodywork, as they are covered from front to rear, yet have an opening behind them that might have an effect on the diffuser and RW. Taking this under consideration, it is clear that the simplification of open wheel VS closed

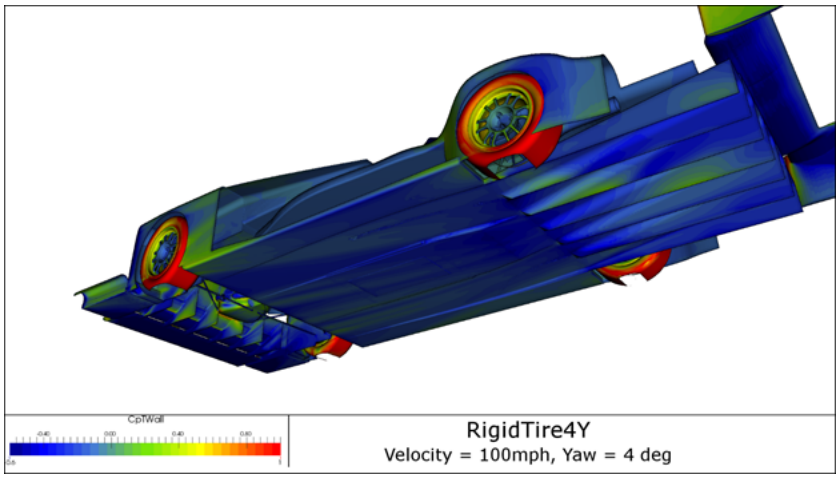

Figure 4.15. Semi open wheel body work design

wheels is a much too crude assessment of the flow features and thus every category should

examine the sensitivity to tire and wheel effects as to determine its significance. In this case, it was assumed the tire would have a significant effect and thus the elaborate analysis was performed. Much was already discussed on the effects of the tires contact patch on aerodynamic performance as an isolated feature effecting the underbody suction features as the UF and FW. Yet looking at wake structures enables a better understanding of body lift reaction to the tire and wheel assembly, as well as RW reaction and balance shift. Looking at the wake from all angles would assist with both establishing better knowledge of flow patterns around a semi closed wheel, while also understanding the effects of yaw, steer and slip angles on the performance of the car. A cut plane in the Y-Z plane right at the center of the front wheels presents a picture of the flow sensitivity to tire deformation

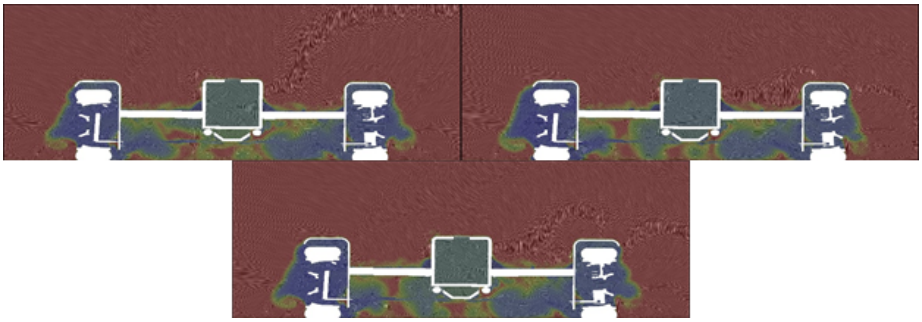

Figure 4.16. X Cpt of 2(left),4(bottom),6(right) Rigid tire

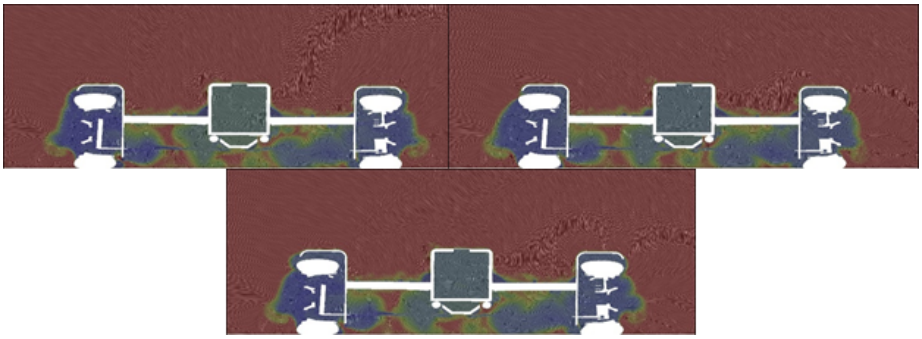

Figure 4.17. X Cpt of 2(left),4(bottom),6(right) deformed tire

Comparing these pictures, it is possible to note that the wake changes quite substantially from state to state while also exhibiting large changes from deformed tire to rigid tire. Since this analysis changes yaw and steer at the same time, comparing state to state variations

would only contribute to the understanding of flow patterns during cornering. While as can be seen, this subject is extremely important yet it is not the main goal of this study rather to compare rigid tire to deformed tire under every cornering condition. The rigid tire presented a common pattern in all conditions showing that once the tire has made contact with the ground a large separated wake forms inboard of the tires, increasing in size moving along the X axis until the tire loses contact with the road. At this point the airflow coming in re-energizes the wake area, this was evident in both LHS and RHS tires. On the outboards side of the tires, no separated flow Is visible on the LHS due to the onset angle of flow while the RHS showed slight separation at 6 degrees. The 2 and 4 degree runs showed absolutely attached flow as the tangential component of the tire's revolution energizes the flow, while as the yaw angle increases this component is countering the yaw angle, thus the larger separation is present at the 6-degree case. The velocity flow patterns viewed for the

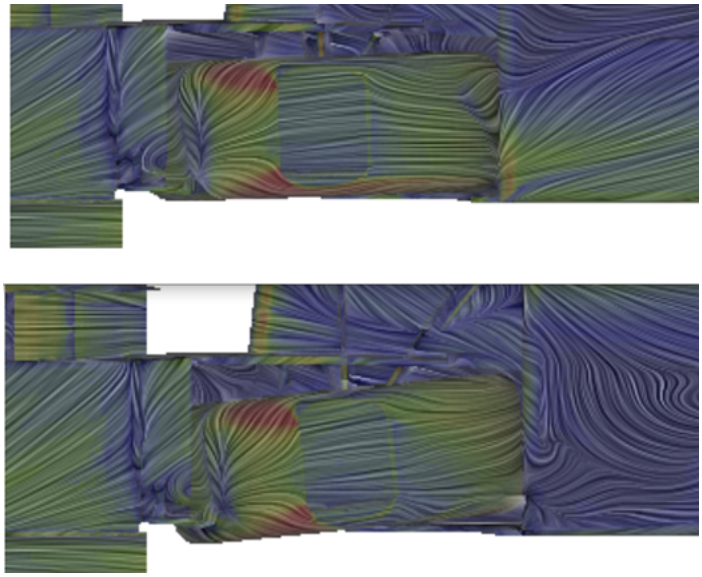

Figure 4.18. Flow visualization 2(top),6(bottom) Rigid tire

2 and 6(bottom) cases further illustrate this condition, showing increased velocity along the shoulder in the 2-degree case while the 6 degree sees complete separation and increased wake. This is not true for the deformed tire front RHS. The increased side deformation along with the steer angle exposes the tire to higher Cpt flow local to the contact patch, allowing for a longer attached flow region at the shoulders. Yet the inboard and center of the tire has

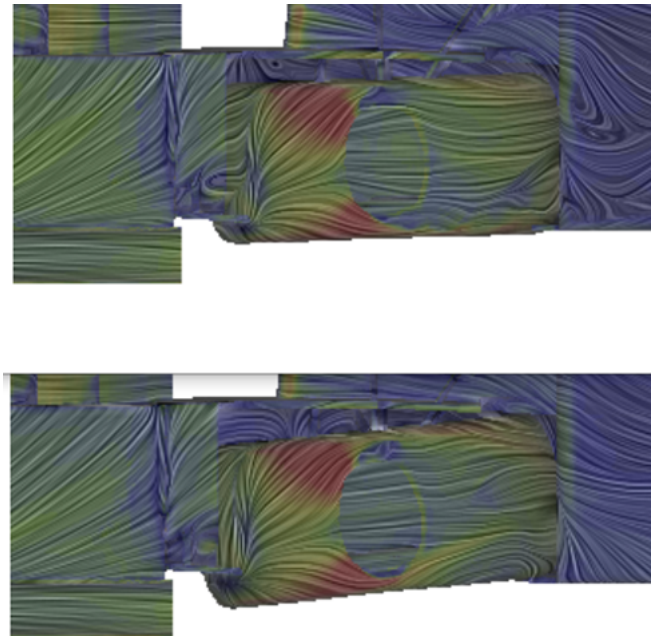

Figure 4.19. Flow visualization 2(top),6(bottom) Deformed tire

separated sooner than the 2-degree case, due to the squash vortex [22] and the tangential component of flow. The LHS of the deformed tire showed similar behavior to the rigid tire as far as outboards contact patch wake development.

The deformed tires outboards side-wake showed a larger area along with an upwash relative to the rigid tire. This is mostly due to the deformed tires larger cross section along with the increased deformation in the Y axis, which, again, exposes more surface area to the airflow thus increasing the wake size. The upwash is created due to the wider top section of the tire from those same reasons. A vortex shedding off of the top of the tires shoulder outboards contributes to the upwash as the orientation of that vortex is to pull air from below upwards. Increased blockage inside the wheelhouse has an effect on this upwash as well. The rigid tire essentially directs flow downwards using the wheelhouse construction, while the deformed tire blocks that path and thus directs the air from the wheelhouse outboards through the sides and not straight down. This creates some upwash instead of pushing the jetting vortex downwards as does the rigid tire. Observing the wake formation character, it can be seen that there is a clear distinction in wake formation comparing both models. In the rigid tire, the inboard side wake combines with the vortices coming from the FW. This

allows for high Cpt air to come from the sides of the Underfloor. In contrast, in the deformed model it is possible to note the horseshoe vortex forming at the leading edge of the contact patch sending two vortices that creates a larger area of low Cpt around the sides of the UF. These findings are in large compatible with the findings of [10] with the different geometry accounted for relative vortex generation difference. This vortex also pulls some of the wake evident in the rigid tire with it , thus the low cpt region is in the outboard side of the UF. The major component here is the inboard and outboard vortices from the leading edge of the contact patch ("horseshoe") along with the geometry difference in diameter, width and curvature. In a Similar manner, no tire axis vortex was found as the wheel well fully covers the front of the tire, thus the most influence from oncoming flow will be due to the jetting vortex and the interaction with the front wing. Comparing the results with previous literature work, it is possible to understand that the aerodynamics of a closed wheel car, and specifically a racing vehicle, is very much dependent on geometry, thus this study does not generalize this behavior, rather explains the effect of including tire deformation models. A different tire or a different construction of the FW, UF or wheelhouse can drastically change the flow field and with it even the trends in wake and force generation. From this conclusion, one can assess when this modeling approach is most important. For a heavily coupled FW and UF combination, tire deformation is essential, as can be seen in this study, due to the effects of the deformation on flow leaving the FW and entering the UF. While a non-ground effect vehicle might experience a smaller change to aerodynamics performance due to tire deformation, as the flow beneath the car is already highly turbulent, introducing some more irregularities. Thus, the tire would not disrupt any flow managing devices and the effect on performance is assumed to be neglectable. As was described in the introduction chapter, the tire has a substantial part in the aerodynamic composition of an open wheel race car due to both its local effect on the fully exposed front wheels, as well as a downstream effect shedded from the wheel. While the effects of tire deformation on the front end of a closed wheel race car were discussed in this section, the downstream effect and the local contribution of the rear wheels are yet to be included in any study. This vehicle makes use of both a large underfloor coupled with a long and massive diffuser. Thus, it is interesting to note that the underfloor is successful at settling the front wheel wake to a point where the flow patterns

are largely identical for both rigid and deformed cases at the entrance to the diffuser. This

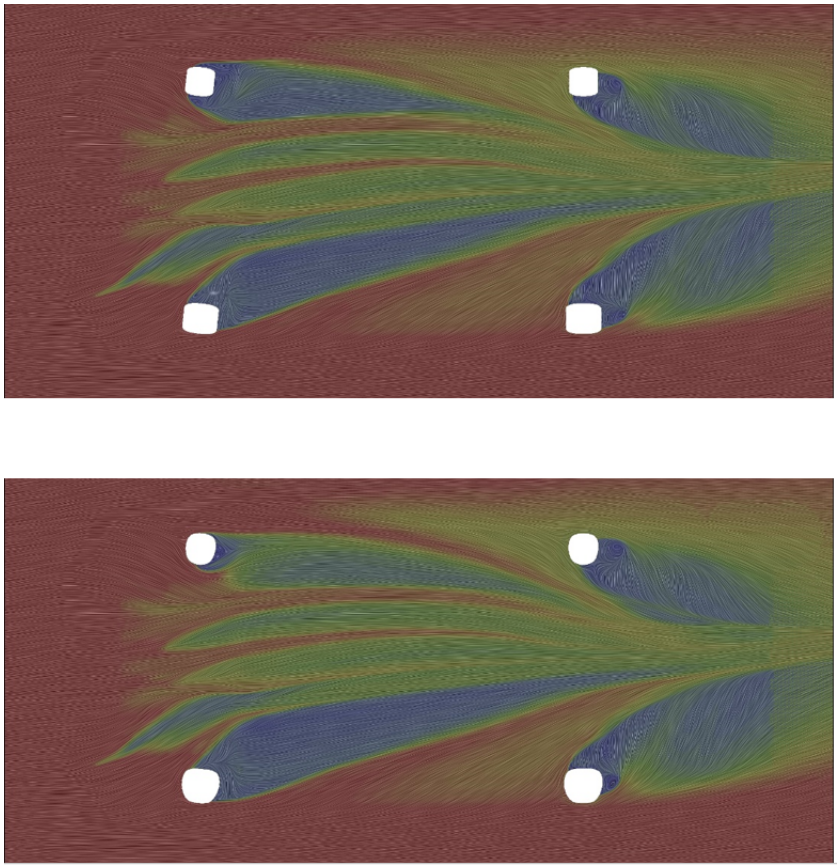

Figure 4.20. Rigid (top) VS Deformed (bottom) Z Cpt at 6 STR/YAW

is maintained at the center of the vehicle due to the UF and diffuser at all slip angles. The only difference being a slight shift of cpt distribution to the RHS in the deformed case, due to the contact patch suction in the inboard side of the RHS wheel, pulling the air in that direction thus a shift is created. It can be concluded that for large ground effect devices at the rear, the tire deformation contribution is not of great significance. The wheel wake, though, differs from rigid to deformed as the deformed tires presents a larger wake with a more pronounced upwash, due to a larger portion of the tire exposed to oncoming flow generating suction. In addition, the shape of the contact patch itself causes separation in different manner, for the rigid tire vs the deformed one. Looking further back at the wake from the wheels, the flow at the diffuser shows that, again, the flow management devices at that area overcome any initial difference in flow structures coming from the wheels, and the

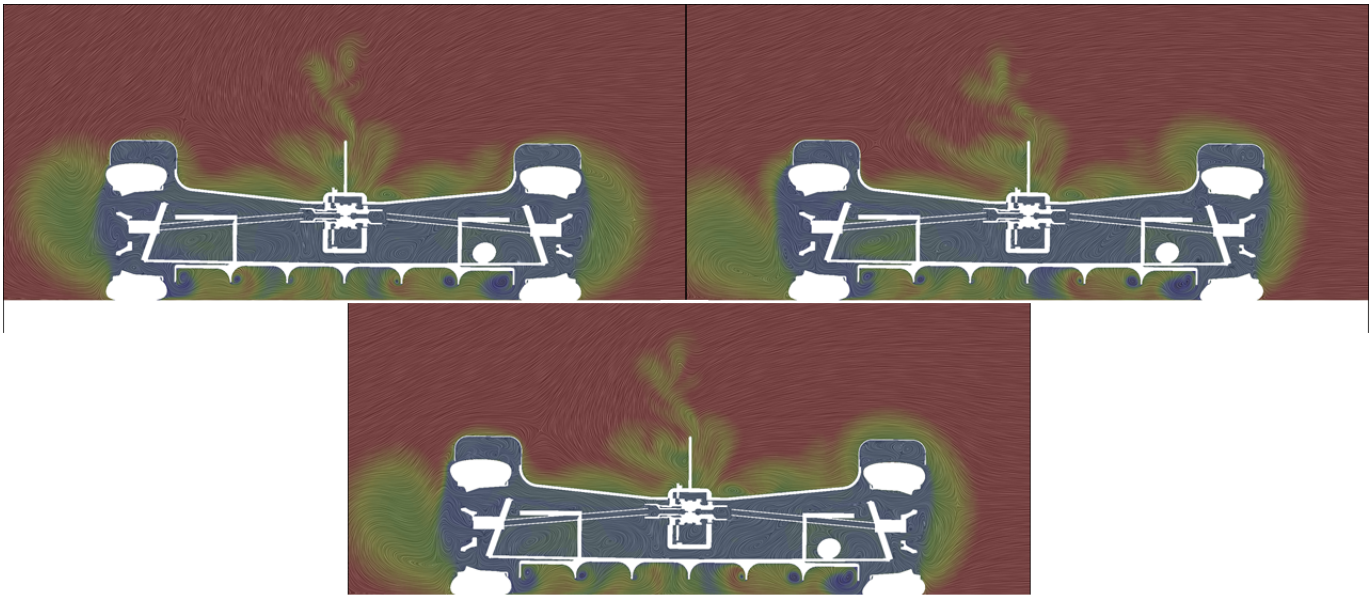

Figure 4.21. X Cpt of 2(left),4(bottom),6(right) deformed tire at rear axle

vehicle experiences almost an identical flow field. Combining these findings along with the flow structures at the throat of the diffuser, it can be said that for a yawed flow case of a car utilizing substantial ground effect devices, the rear tires are largely indifferent to deformation modeling, as they are less exposed to oncoming flow, less prominent due to high efficiency ground effect devices navigating the flow, and present a lesser contact patch suction due to higher loads flattening the tires contact with the ground over the width of the tire.

4.3 Cornering analysis - Curved Flow Domain

This section of the study would assist with understanding the behavior of the flow while fixing the Yaw variable. It was previously shown that the DF delta between rigid and deformed model reduces as Yaw and Steer increase. Furthermore, since it was also seen that the side force increases linearly with yaw and steer, it was concluded that yaw must be fixed while sweeping steer. Since sweeping steer by itself would not account for any wind

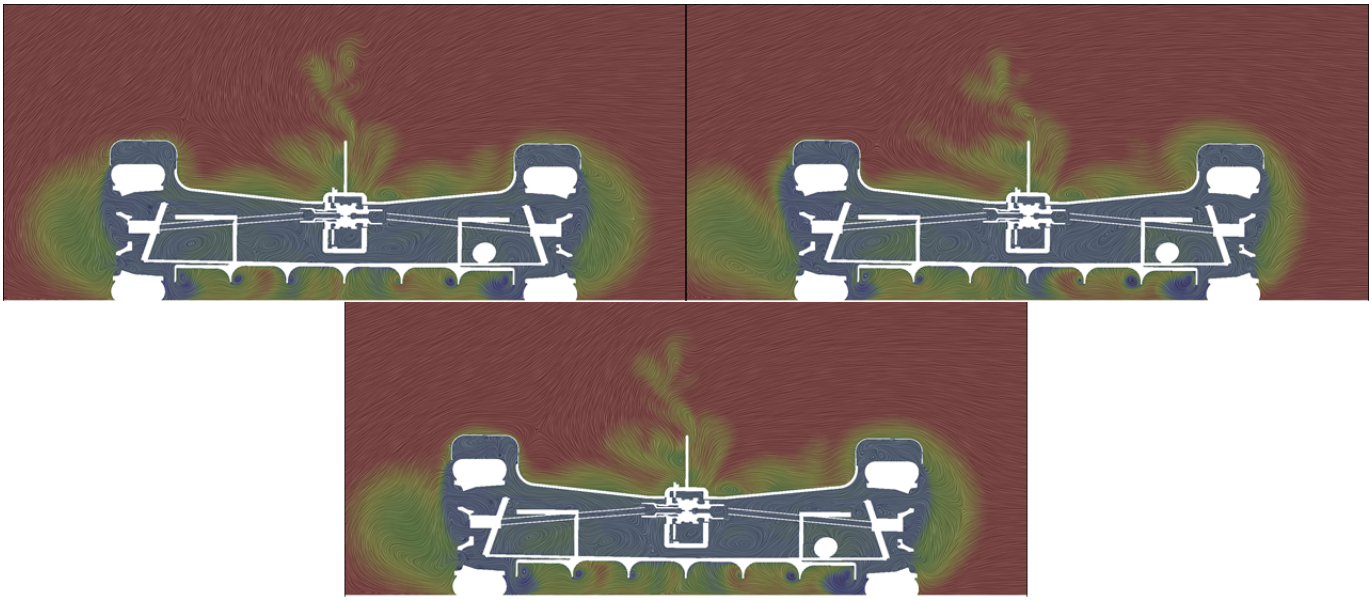

Figure 4.22. X Cpt of 2(left),4(bottom),6(right) rigid tire at rear axle

angle changes, performing just a steer sweep by itself would result in a large error, as it was seen that wind angle has a large effect on the wheel wake. Thus, by introducing curved flow, yaw is supplied to the model by the path curvature which was set at 100 [m] radius. This yaw is not fixed along the vehicle's centerline allowing for a more realistic physical representation of the flow during a cornering maneuver. It is important to note that this method can only be correlated at full scale on track testing, as no wind tunnel is built to handle this simulation. With that said, this study is set to understand the contributions deformed tires has to the flow structures, thus using this method would help obtaining the behavior of the flow, even if it could not be correlated particularly well. In order to make sure the data from the curved domain case is the same order of magnitude as the straight-line case, results from the curved and straight domains were compared at 2 degrees for both rigid and deformed tire. This was chosen for comparison as it was expected that as the steer increased, the deviation from modeling technique would increase as well. Thus, the lowest angle would present a good case for baseline comparison. It was seen that all force values

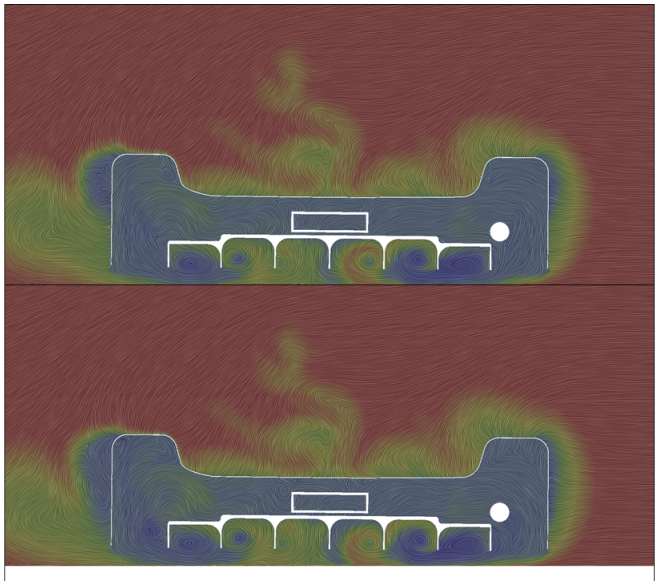

Figure 4.23. X Cpt of rigid tire (top) and Deformed (bottom) at Diffuser throat

for the deformed model were very much identical, with the exception of side force, as it is clear that introducing artificial yaw over-predicts the side force values. In addition, a 1% backwards balance shift was documented in the curved case, due to an increase in underfloor performance. Looking past the 2-degree case and comparing all tested angles, it is clear that these force results are very close to the straight domain, showing low sensitivity to modeling technique. At the same time, the curved analysis provided higher values for Cz and much lower and stable values for Cs, while Cx values were practically unchanged. The rigid tire provided a trend showing better correlation at high yaw values, while the results differed greatly at lower values. Looking ahead, this implies that once a significant change has been made to the tire angle, the effect it has on the flow along the vehicle is greater than the effect the artificial yaw has. This conclusion calls for the most accurate representation of the tires effect on aerodynamics, as it is the dominant factor for steered simulations, thus including deformed tire model in the simulation would help with achieving the best representation. Once it was determined that the curved flow case does produce physically relevant results, both tire models were compared to gain understanding as to where are the most significant force generation location and how they compare to a straight domain. Observing the 6 degrees cases for both models, using both CFD modeling techniques, it can be understood

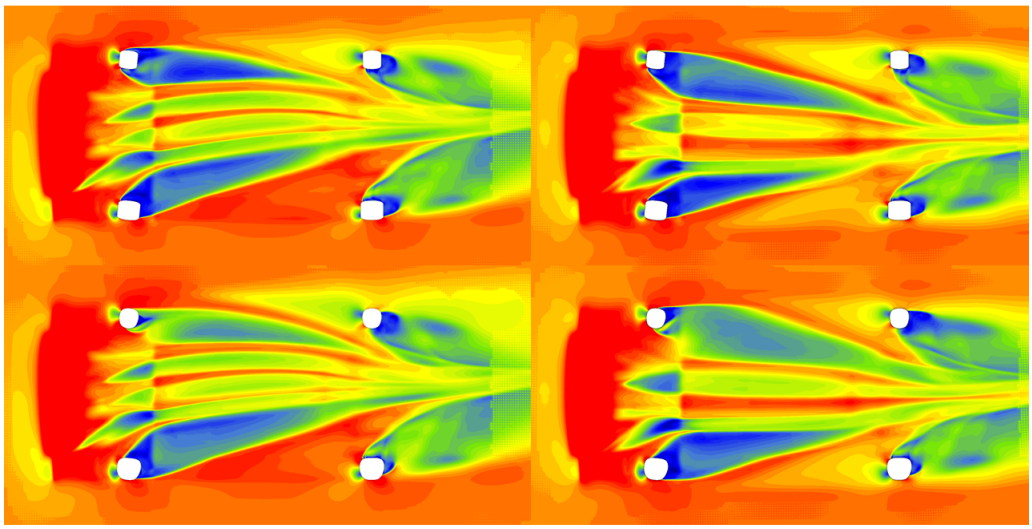

Figure 4.24. Z Velocity contours Rigid (top) VS Deformed (bottom) at curved (right) and yawed (left) domains

that the rear of the car is mostly unaffected by modeling technique, as the onset flow angle is set by the rear wheels, thus this result was predictable. Yet, it is clear that the centerline of the car is provided with higher energy air at the curved cases, as the flow on the front-end experiences little to no yaw, thus air can be directed with only a slight curvature into the diffuser. The deformed case showed a larger wake behind the RHS tire, which results in slower air under the UF. the force data further supports this claim showing lower DF values for both the UF and the RW. On the other hand, the same trend as was seen in the straight domain cases, is evident at the front end where the suction peak under the front diffuser is much greater due to the increased suction from the deformed RHS tire. The shape discussion from the straight domain case illustrated the effect side deformation has on the stagnation point in front of the tire. It was concluded that at high steer angles the tires contact patch loses its oval shape and becomes a trapezoid with a wide and flatter front end, resulting with lower suction in the inner side of the RHS tire, increasing stagnation pressure. These trends result in a huge 3.3% forwards shift in aero-balance at this position for the curved domain case. This increase relative to the straight domain is due to the lower yaw angle experienced by the front. Moreover, the yaw angle the front experiences is

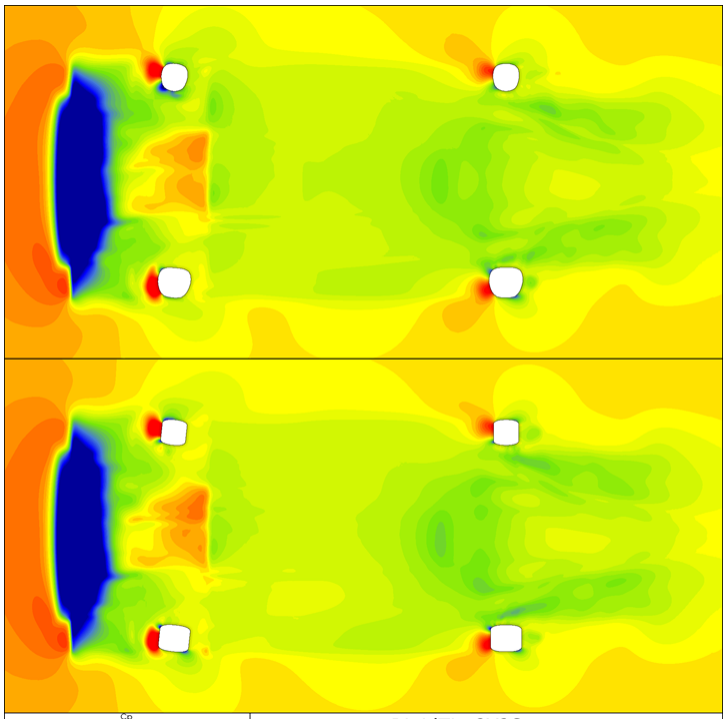

Figure 4.25. Z Pressure contours Rigid (bottom) VS Deformed (top) at curved domain

actually positive for the curved case, as the yaw is coming in at the velocity vector which changes direction front to rear. Due to that fact, the suction peak at the front of the curved domain case is much greater than in the straight domain, as the flow aligns with the tire centerline enables it to accelerate along the surface of the tire without abrupt stagnation, due to artificial yaw at an angle opposite to the flow lines. Examining the trends within the curved domain would determine if the tire effect is dependent on CFD technique, or does the change in yaw along the centerline of the vehicle presents a large contribution to the tire effect. The Cx trend showed an obvious example for the curved domain contribution to this study. The rigid tires drag values decreased as the steer angle increased, while the deformed tire experienced higher drag values with steer increase, yet with a less clear trend. It was expected that the rigid tire would present these results, since increasing steer aligns the front wheels with the oncoming flow, reducing drag. The result for the deformed tire was much less predictable, as it was seen that due to the increased contact patch width along with the alignment to the incoming flow, increased the drag values. Yet, at the highest

steer angle a slight reduction was observed relative to the 4-degree steer angle. This can be attributed to the higher suction created at the 6-degree case due to the shift outboards in the RHS tire. The Lift coefficient showed that both models provided the same trend for

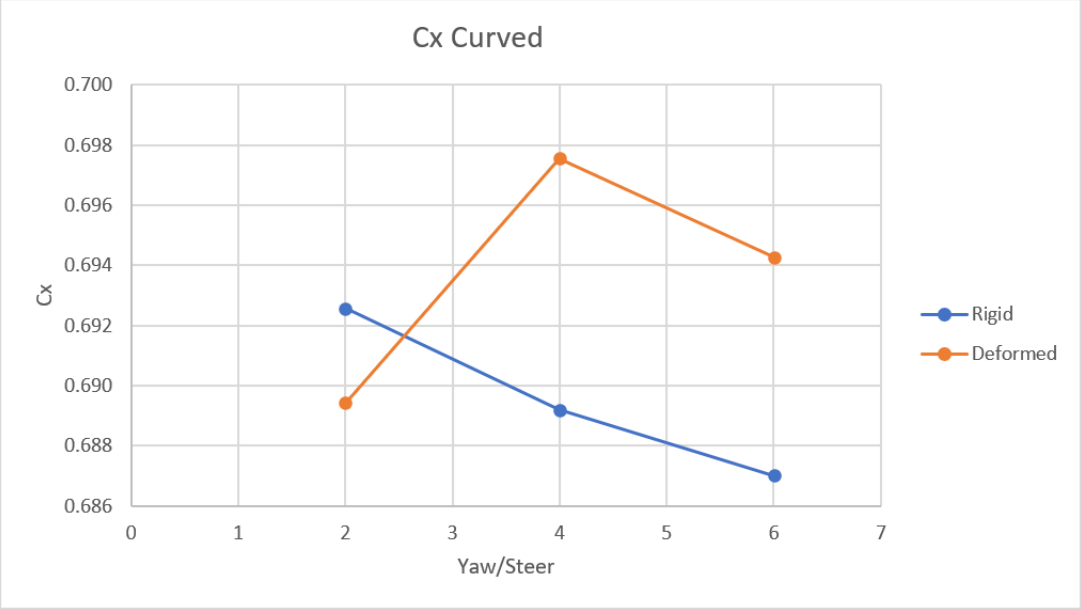

Figure 4.26. Rigid VS Deformed curved flow domain Cx

downforce generation, albeit the deformed tire produced much greater downforce number than the rigid tire in a similar manner to the results documented from the straight-line case. This is due to increased suction under deformed cases RHS tires with the same mechanism of force generation as was discussed in the straight line analysis. Focusing in on the tires effect on balance under the curved domain demonstrates every effect discussed so far and visualizes the Y direction shift in contact patch, tire centerline and dead wake behind the tires. This discussion enables a complete understanding of the flow field and with it a more educated conclusion. Moving from the front end backwards it is visible that at 6-degrees the highest Cpt values are present providing higher energy air below the diffuser and into the under floor, resulting in high values of down force in both areas. The tire wake seems to be largest at 2-degrees and smallest at 4-degrees, this is due to the acceleration at the contact patch. The 2-degree case shows the weakest contact patch pressure peak at the front RHS tire, and thus the flow detaches fairly early on the tires surface resulting with a large

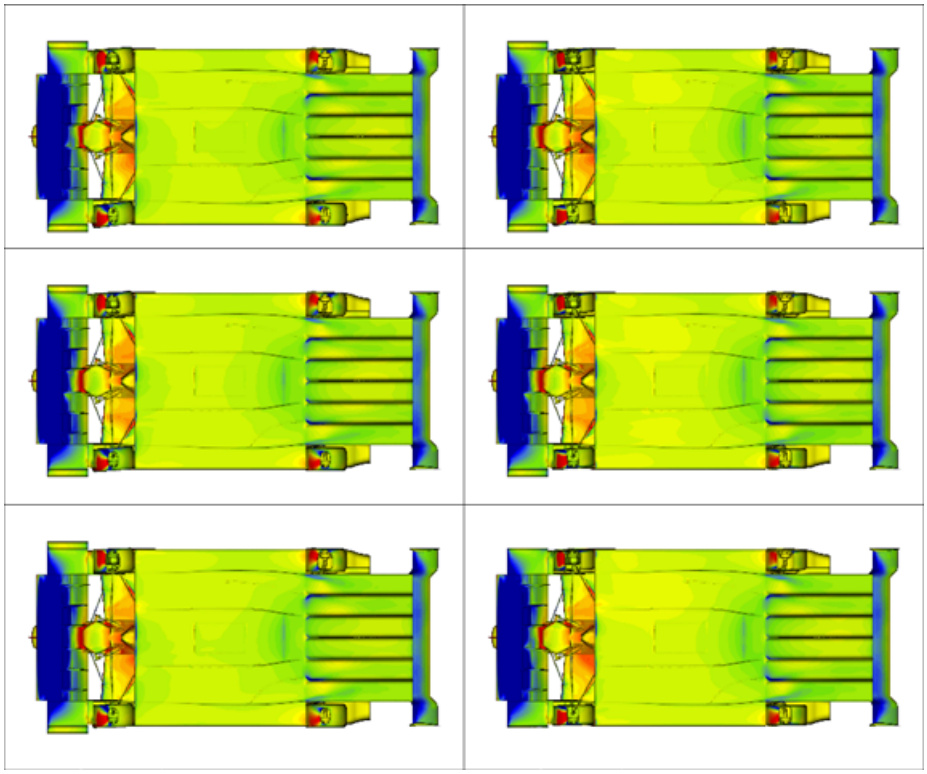

Figure 4.27. Rigid (right) VS Deformed (left) curved flow domain Body cp sweep

wake, yet the smallest recirculating bubble. Thus, the pressure behind the RHS wheel is the highest which accounts for the lower wheel drag value recorded. On the LHS both front and rear experiences the weakest stagnation pressures, especially at the rear, allowing for higher energy air to be inserted into the underfloor due to pressure difference. At 4-degrees the smallest wakes are seen, but with the most pronounced recirculating bubbles. The increased suction on the front RHS causes the FW pressure peak to shift towards the RHS tire to a position where it is less effective, as no airfoils are placed in that section, resulting with lower downforce values along with lower UF values, as the air coming into the UF is not as fast flowing as in the other cases. The lowest RHS stagnation pressures were recorded in this case, along with moderate stagnation pressures on the LHS, resulting in the smallest wheel wake size. Yet, this combination pushes the streamlines into the centerline, reducing UF efficiency and thus overall downforce. The 6-degree case showed the largest wakes resulting with a high drag penalty along with the highest FW downforce values. The large rear wakes are sent into the RW loosing performance while the front wing gains performance, this accounts

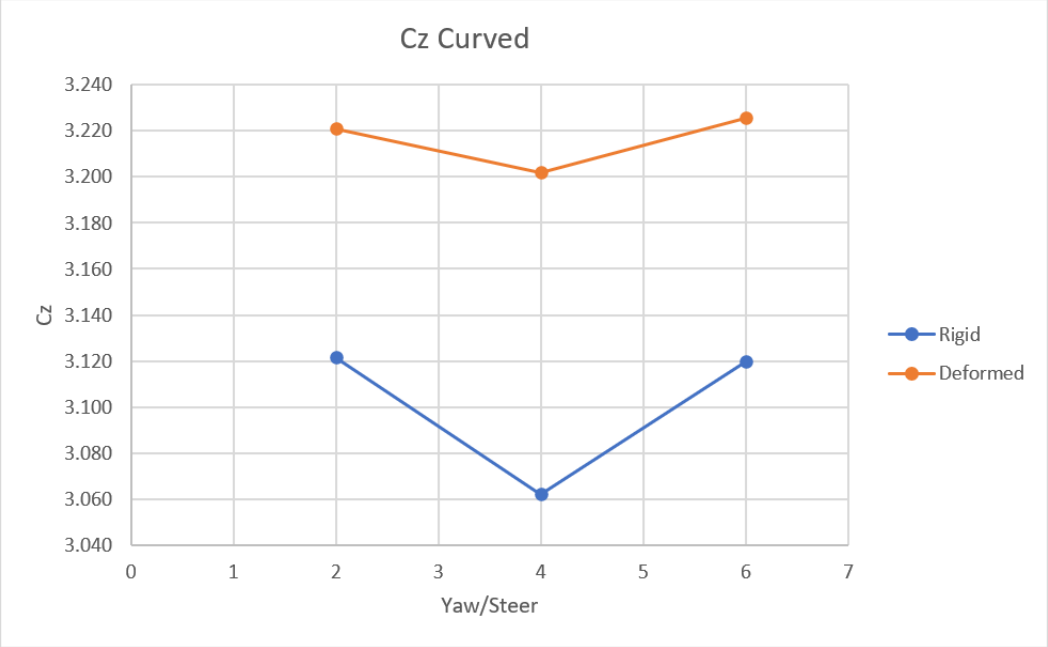

Figure 4.28. Rigid VS Deformed curved flow domain Cz

for a significant forward shift in balance relative to the other two cases. At 2-degrees the highest values of Cpt can be viewed along the centerline of the car, representing the best performing underfloor. High stagnation pressure in front of the contact patch, along with only moderate suction due to their shape, provides for the highest wheel lift values. At this steer angle the largest amount of body lift was recorded, with the bulk of it apparent at the front. Thus, the combination of all the components maintains similar values of downforce as the uncurved domain, yet a slight shift backwards is evident in this case as the underfloor is less effected by yaw due to the curvature of flow in that area. As was the case in the straight domain study, the deformed tires present significant alterations to the flow field up and down stream, changing flow structures by the same mechanisms:

1. Contact patch shape – providing local acceleration and suction at the ends of the contact patch due to low ground clearance. It also accounts for the reduction in stagnation pressure which presents a significant effect upstream.

2. Contact patch location – A shift in the Y direction shifts the whole tire, increases drag while enables a reduction of stagnation pressure behind the FW. Both account for the intensity of separation at the wheel wake.

Comparing the results from both domain types, it is possible to see that the deformed tire model shows a lower force data sensitivity to CFD testing approach. The values agreed with the straight domain, yet the data trends were opposite for both balance and side force. In contrast, the rigid tire results varied greatly from the straight domain, yet most trends were maintained with the exception of drag decreasing, using a curved domain while the straight domain showed stable drag values. Both models showed exactly the same trend for side force under curved domain analysis just as they showed in the straight domain case. Yet, while the straight domain introduced a linearly rising curve, the curved domain presented a polynomial decrease in side force. In addition, the difference in values between rigid and deformed model in the curved case was much greater as both cases presented significantly lower values of side force, thus suggesting that yawed flow does not represent true side force values, as it introduces an error assuming constant yaw angle along the vehicle. This conclusion further supports the claim for on track testing of the deformed tire, as it presents another error introduced by wind tunnel testing limitations, that when properly correlated would have the potential to completely alter the aerodynamics testing procedures up to date.

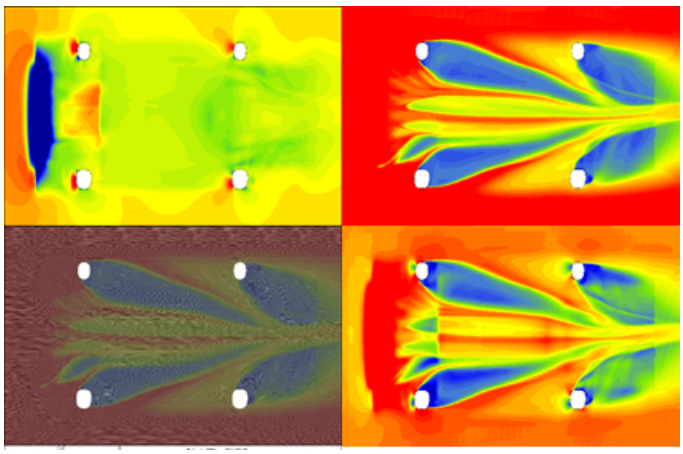

Figure 4.29. Deformed curved flow Cp, Cpt, Velocity at 2 STR

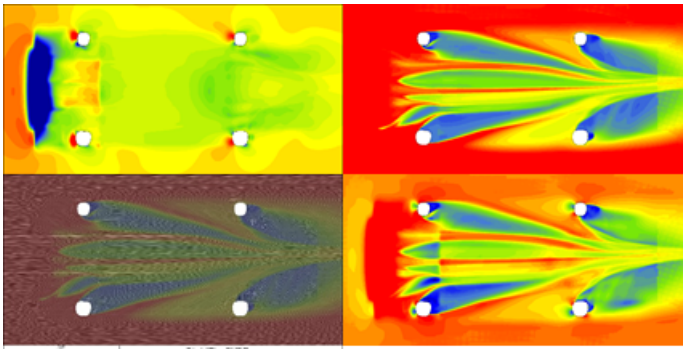

Figure 4.30. Deformed curved flow Cp, Cpt, Velocity at 4 STR

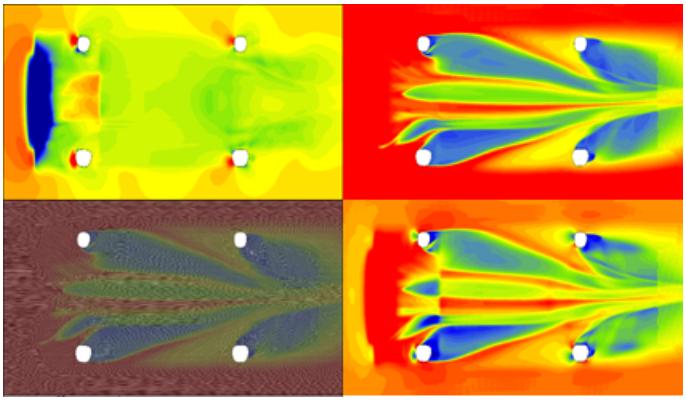

Figure 4.31. Deformed curved flow Cp, Cpt, Velocity at 6 STR

Comparing both rigid models and deformed model would provide clarity as to which aspect is more modeling technique sensitive or more shape sensitive.

It is clear that the side force is largely unaffected by deformation modeling, as both in the circular domain as well as the straight domain the vehicle reacts in the same manner for side force generation. A linear increase as yaw and steer increases in the straight domain while a shallow decrease in force is noted for both curved domain cases, showing that the side force is heavily yaw sensitive. This conclusion calls for verification to be done on track, as it presents a completely opposite trend to the current method in which the flow is yawed similarly to a WT test. Looking at the Balance curves, one can see that the rigid tires reacted similarly in both simulation techniques, while the deformed tires differed both in trend and in values. The deformed tire models provided significantly larger balance numbers, showing that both the underfloor and FW are very much sensitive to the tire modeling due to pressure peaks at

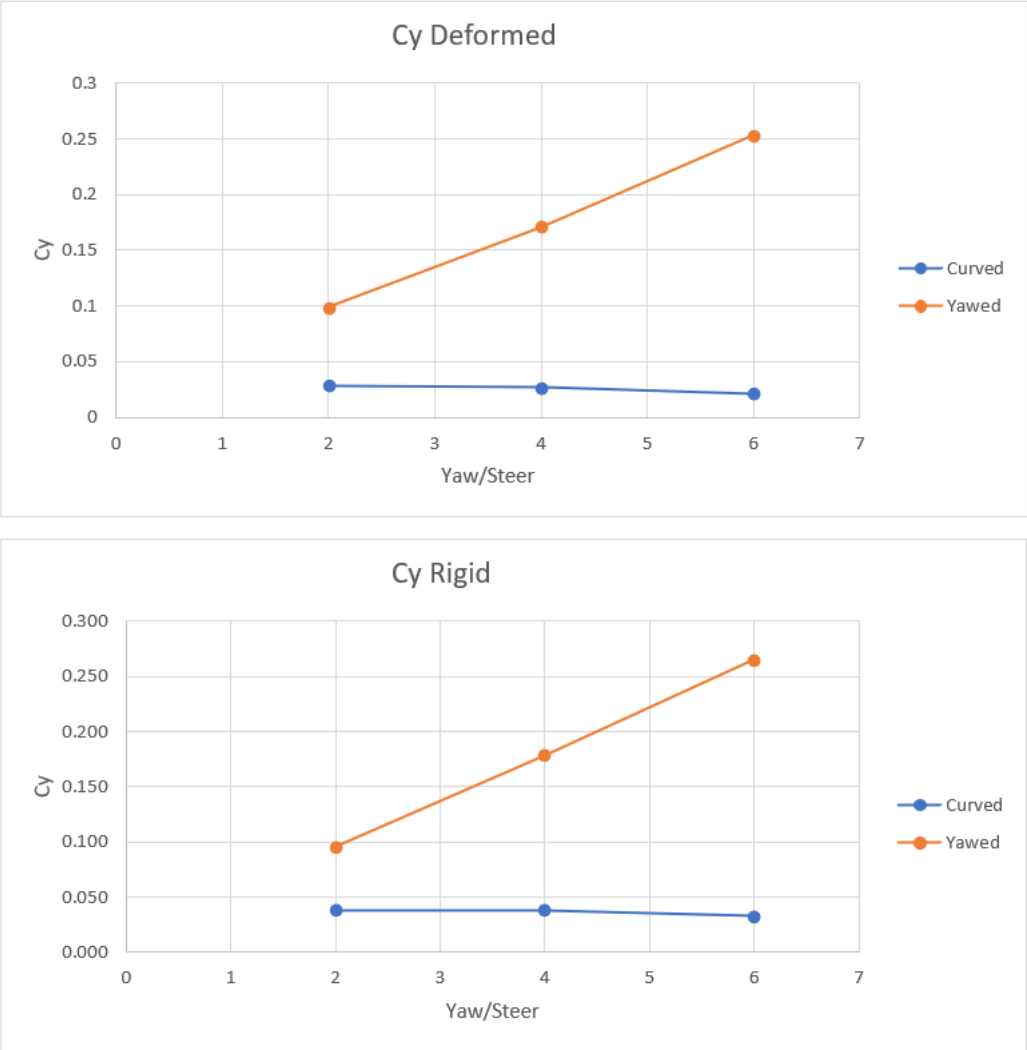

Figure 4.32. Cy comparison

the front tires and wake structure at the UF. Hence, the rigid tire shows lower sensitivity to CFD modeling technique than the deformed tire. Checking the Cz values shows that while the trends are mostly maintained for both techniques, the deformed tire provides more stable results with a low delta value, while the rigid tire has a large variation over the same test span. Concluding that the shape of the tire is more dominant than the modeling technique, which is to say that the deformed tire is less sensitive to CFD technique. Lastly, drag values are compared showing that while the rigid tire provides a stable set of results within the given sweep, the difference between the values for curved and yawed flow has a large deviation. The deformed tire, on the other hand, provides very similar results, except for

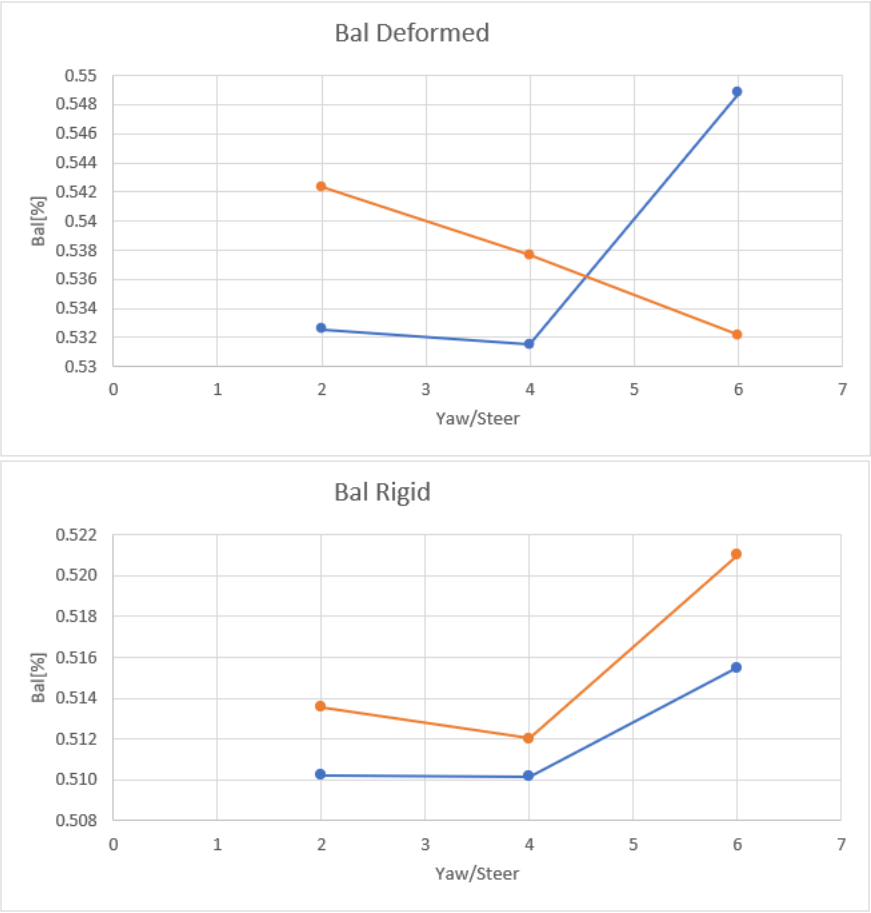

Figure 4.33. Balance comparison

the 4 degree cases that presented completely different flow patterns for curved and yawed flow. This suggested that drag values are more reliant on tire modeling than CFD technique. Looking at flow structures at the rear, a similar trend to the straight domain sweep can be seen. The flow under the car is almost identical in both rigid and deformed tire due to the large diffuser, and the same shift is evident again due to the RHS contact patch suction. The main difference evident in the curved domain as opposed to the straight line domain is a more oval like wake formation behind the LHS wheel. This is essentially the same upwash evident in the straight domain, only here it is more pronounced at the LHS than at the RHS, as was the case in the straight domain. This is due to the flow shifting direction from negative to positive yaw along the car. In addition, the over-prediction of side force for the yawed flow case is evident here as the wake of the curved domain is much less biased to one

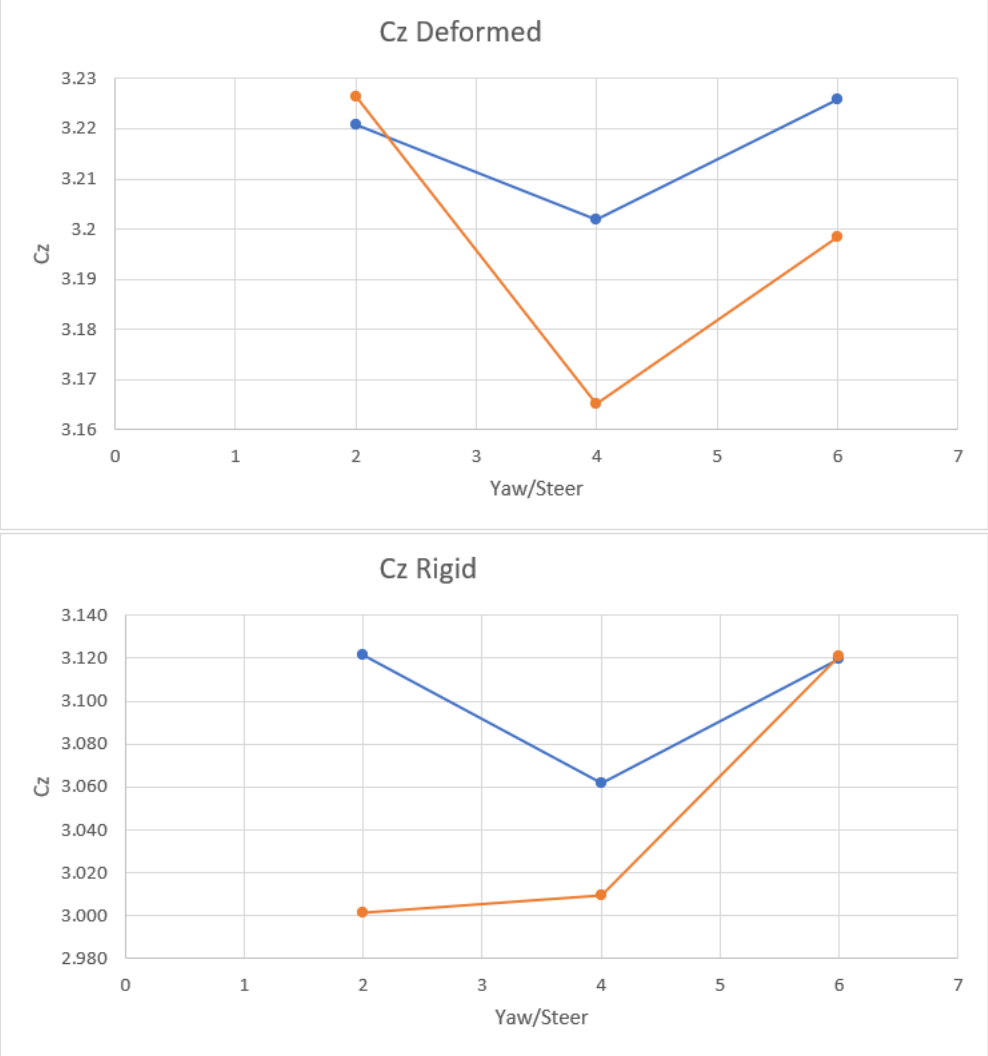

Figure 4.34. Cz comparison

side providing for significantly lower side force values. As the flow travels in an opposite direction at the front of the vehicle in this case, as opposed to the yawed flow case, the wake structure of the front is inherently different. The RHS wake at the curved case has decreased in size as the flow is coming in to that region instead of the other way around. The rigid tire at this position has smaller area exposed to flow, thus less blockage and a smaller wake. This is evident through all the ride points. As the deformed tire has a larger area exposed to flow that is coming in the same orientation as its centerline direction, the portion of the tire uncovered with body work actually remains attached, contributing to higher wheel lift values compared to the yawed flow case. Yet, these values are much lower than the ones

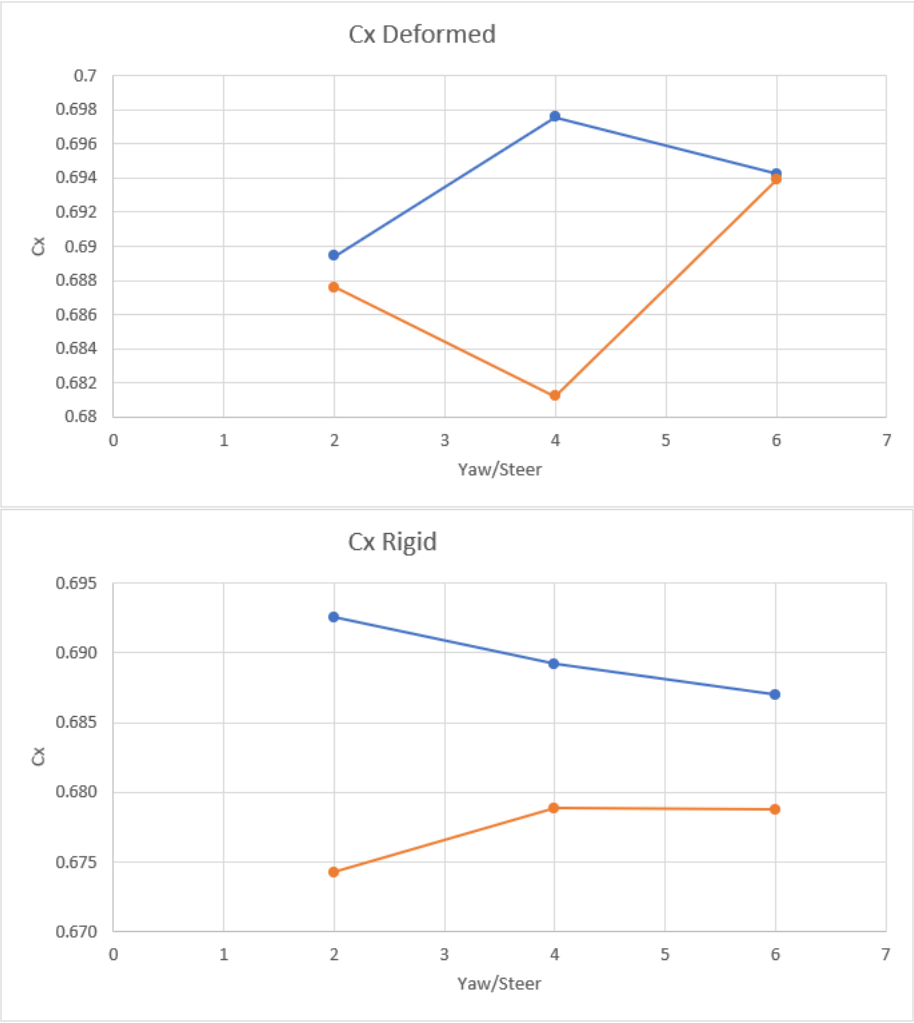

Figure 4.35. Cx comparison

recorded for the rigid tire. On the LHS a larger wake is observed compared to the yawed flow in a similar manner to the RHS as flow now travels in the opposite direction. Inboards of both sides the wake structure is more energized compared to the yawed case, as the flow condition streams higher Cpt through the middle of the car and a lesser blockage from each side is observed. The deformed tire at this flow condition has a larger effect on the front wing and with it on the aero balance of the car. Almost 100 [N] of downforce are added to the deformed tire model as the same effects observed in the yawed case are amplified here due to the direction of flow. The air moving from right to left has the benefit of the contact patch suction being on the inboard side, thus some of the wake is pulled away from the centerline of

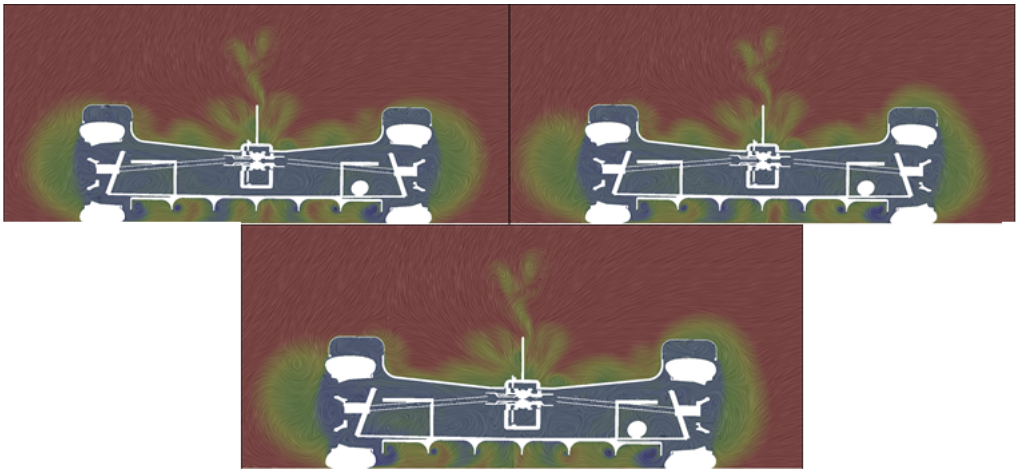

Figure 4.36. Curved domain X Cpt of 2(left),4(bottom),6(right) deformed tire at rear axle

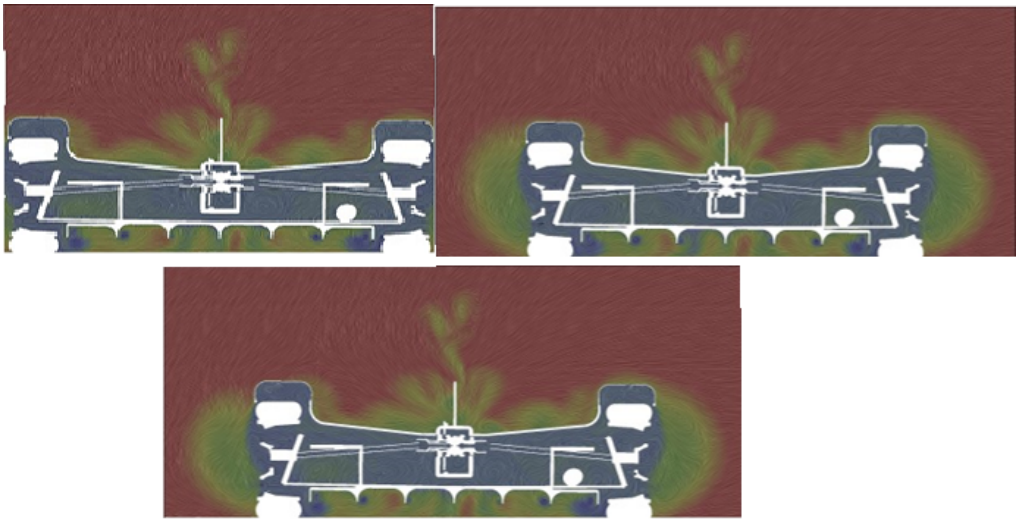

Figure 4.37. Curved domain X Cpt of 2(left),4(bottom),6(right) rigid tire at rear axle

the vehicle, increasing both the FW and UF efficiency shifting balance forwards. Compared to the rigid tire in this flow condition, the FW has more than 60 [N] increase in downforce at all slip angles along with higher drag values stemming from lift induced drag due to the same trends seen in the yawed case. These trends cause for a lesser difference from rigid to deformed at the curved domain, as the yaw magnitude relative to the centerline of the body is lower, showing that the tire deformation has some sensitivity to yaw, as increasing yaw magnifies the relative difference in flow field from deformed model to rigid

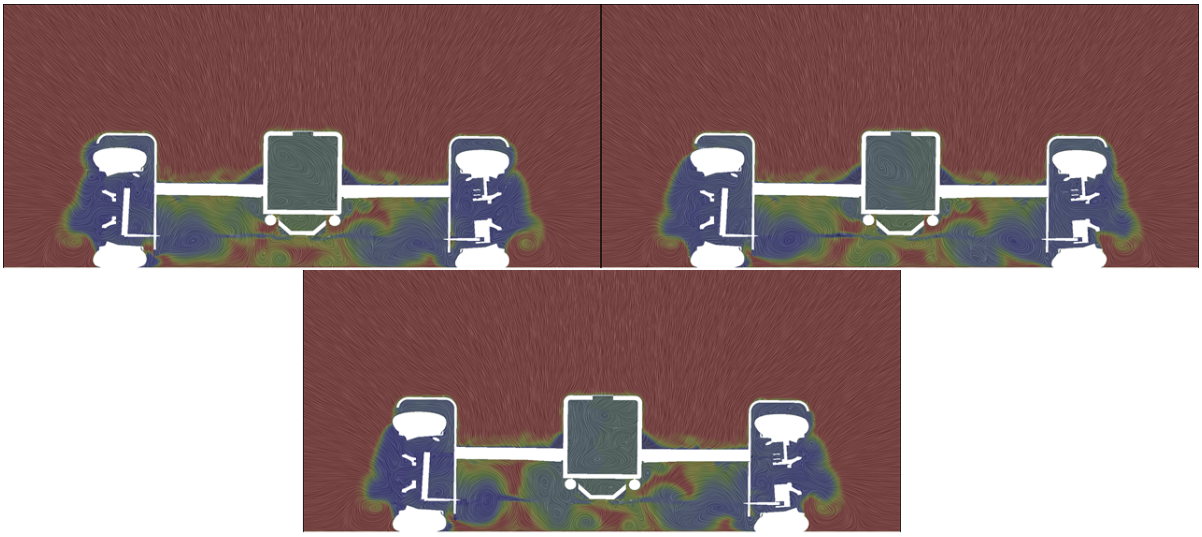

Figure 4.38. Curved domain X Cpt of 2(left),4(bottom),6(right) deformed tire at front axle

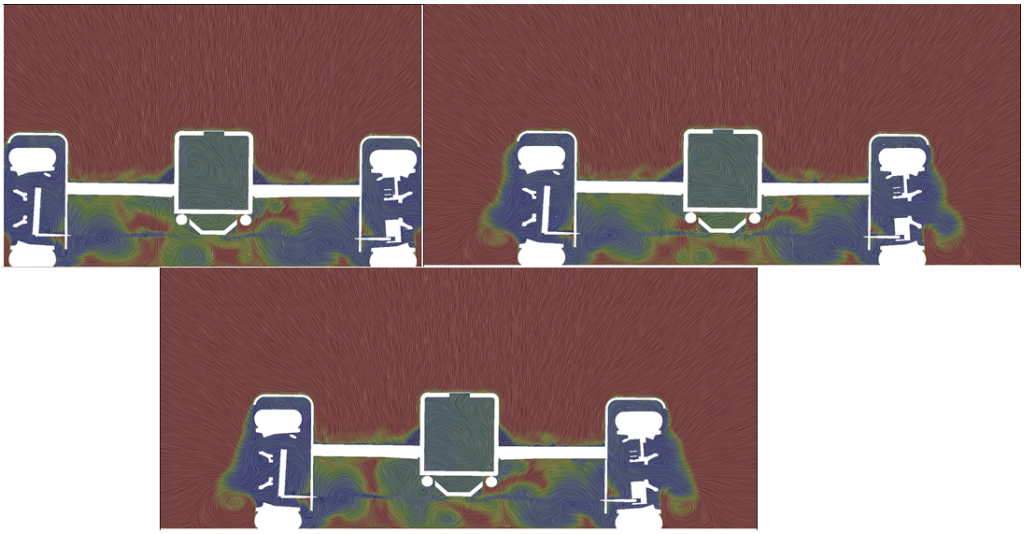

Figure 4.39. Curved domain X Cpt of 2(left),4(bottom),6(right) rigid tire at front axle

Taking all into account, it is fair to say that including deformation in the analysis can assist with more stable force results along with a different distribution of those forces. Yet this might only be true for this specific car, as it has a high ground effect dependency. Introducing deformation into the tire unlocks new flow patterns that just cannot be reproduced by a rigid tire, as it does not deform sideways or present an oval contact patch, both of which result in flow conditioning mechanisms that can either be used for future development or can be noted

for handling purposes. While the rigid tire provides for an easy representation of a block in the shape of a tire, it cannot accurately simulate a real tire as it is without contact patch acceleration nor shape dependency. As seen in the results, these effects leads to completely different results both in absolute number and in force trends.

4.4 Inflation Pressure Sweep

After understanding the significance tire modeling has on aerodynamics of a race car, the common tool for handling adjustments – inflation pressure changes was examined. As was seen in the work done so far, every subtle change in the tire's shape can result with a significant change in forces generation including the mechanism for generating those forces. For this reason, varying the inflation pressure introduces a number of variables to the model that can be easily modeled and reproduced with the deformed tire model, where as in the rigid model only the spring rate can be altered using linear assumption and provided tire deflection data. These variables simulate different steady states of the tire to ensure an accurate reading for every inflation pressure, and thus every outer dimension, stiffness and friction coefficient. During a race, a common tool to quickly adjust the handling characteristics of a car is by increasing or decreasing the tire inflation pressure. This in turn changes the cornering stiffness of the tire which accounts for the understeer gradient that determines a vehicles tendency to oversteer or understeer. While this tool has been in use for vehicle dynamics purposes, it is unclear whether a change in inflation pressure contributes to a gain or loss of aerodynamics performance. Hence, using the developed model these features can now be simulated by including 3 sets of tires at a given slip/steer angle. Since the inflation pressure in this case is set at 18 PSI, changing it drastically would introduce issues to the tire model, as the stiffness of the tire changes immensely due to inflation pressure variation. Thus, the model would need to be re-calibrated for very low pressures. It was decided to test the tire at a+- 2 PSI variation which corresponds to a 12.5-10% change in pressure. In terms of absolute numbers the tire was tested at 16, 18 (nominal) and 20 PSI, doing so will show the effects of softening the tire and hardening it at a given slip angle. The set of 2 yaw 2 steer was chosen as it presents a large delta between deformed and undeformed configurations while also showing

a significant amount of side deformation without lowering the tire shoulders onto the road - a condition that will cause rapid tire wear and reduced performance. In addition, since this is an extremely soft tire, the 2/2 set ensures that there is no over-prediction of the results as the analysis is done within the best operating conditions of the model with regards to mesh deformation. Since the pressure is already relatively low, it was assumed that an increase or decrease of +- 2PSI would provide with a significant difference in the results. Yet as can be seen from this data set, the change in pressure has not provided any large magnitude result deviation, nor has it provided any clear trend. The drag was largely unaffected by the pressure change as it displays only 3 [N] difference which is within the analysis error thus is considered constant. The exact same can be concluded for the side force as no major force data trend can be extracted for this set. The downforce showed an increase of 28[N] between 18-20 PSI cases, showing that while the drag and side force were unaffected, the downforce has some sensitivity to pressure changes. The area most affected by this change is the underfloor, as a 22[N] increase was documented going from 18 to 20 PSI while the front wing lost 13 [N] of force during that span. While it can be seen that the pressure on

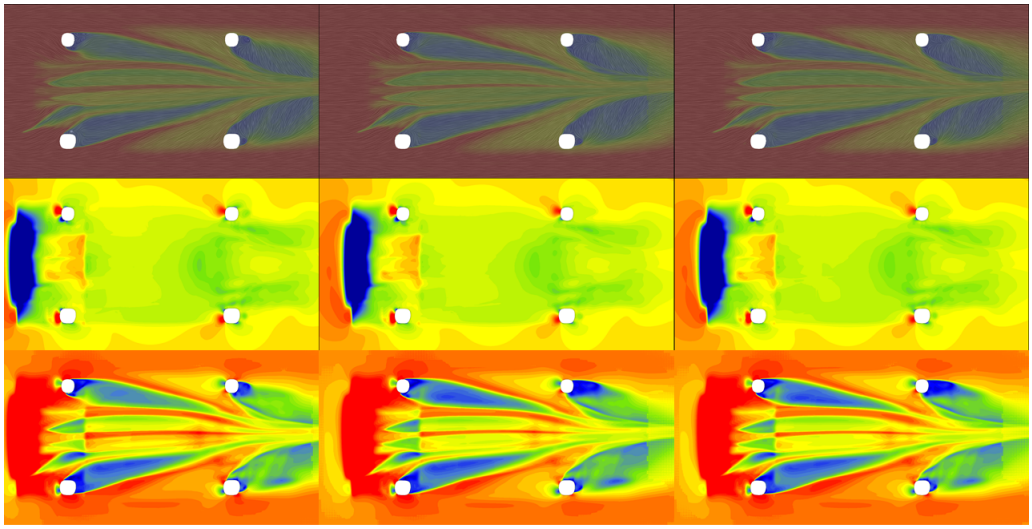

Figure 4.40. 16 (left), 18 (middle), 20 (right) PSI sweep Cp, Cpt, Velocity

the underfloor reduces as inflation pressure increases, there is no clear trend as to why this happens. Observing CpZ values further shows the change in pressure over the underfloor, yet

without any obvious mechanism for it. The interesting performance metric to note in this case is the balance shift. Plotting the balance VS tire pressure, one can see that the balance does not change proportional to the tire pressure, as it decreases by 0.6% for the 20 PSI case and decreases by 0.9% for the 16 PSI case. While the change is visible in the data, it is small yet it also implies that a further pressure change study might present a larger decrease in balance due to stiffness changes. It is important to note that as the tire pressure decreases the deformation increases and thus hysteresis loops gets larger, resulting in a loss of energy in the form of heat generation. This model does not take into account the temperature effect, as doing so for each tire is extremely time consuming. A decrease in pressure would not result with increased energy loss or increased friction coefficient, both of whom can provide further deformation to the tire than currently presented. As was described in the FEA generation chapter, the viscoelasticity characteristic is modeled using a Prony series, which describes the decay over time of a function - in this case the stress over time. This test is conducted under a single temperature and thus is not an accurate representation of the entire operating conditions range. In order to include this effect, a master curve needs to be generated describing the behavior over a large temperature range in addition to a subsequent step to the steady state transport. In this step the dissipated energy is to be extracted from "Abaqus", using the Elastic strain energy density output, and multiplying it by the tan delta which is the loss modulus divided by the storage modulus. The tan delta is a quantity used to describe hysteresis variations. Once the dissipated energy has been calculated, the heat flux can be obtained by multiplying the energy by the travel frequency. This heat flux determines the amount of energy lost to the environment by conduction and convection (neglecting radiation). Applying a conduction/convection condition to the corresponding section in the tire and performing a 2D temperature coupled analysis would result with the tire deformation, due to heat generation. Comparing the cross section of this analysis with the one being used for this study would reveal the significance of this issue and if it can be mitigated by a master curve Prony series representation. This is a case study by itself, fine tuning the analysis approach to find the most efficient mix between results accuracy and time to prepare and run a case. For future work it would be wise to examine a larger data set of both inflation pressure sweeps along with a slip angle sweep, as it is not clear if the small

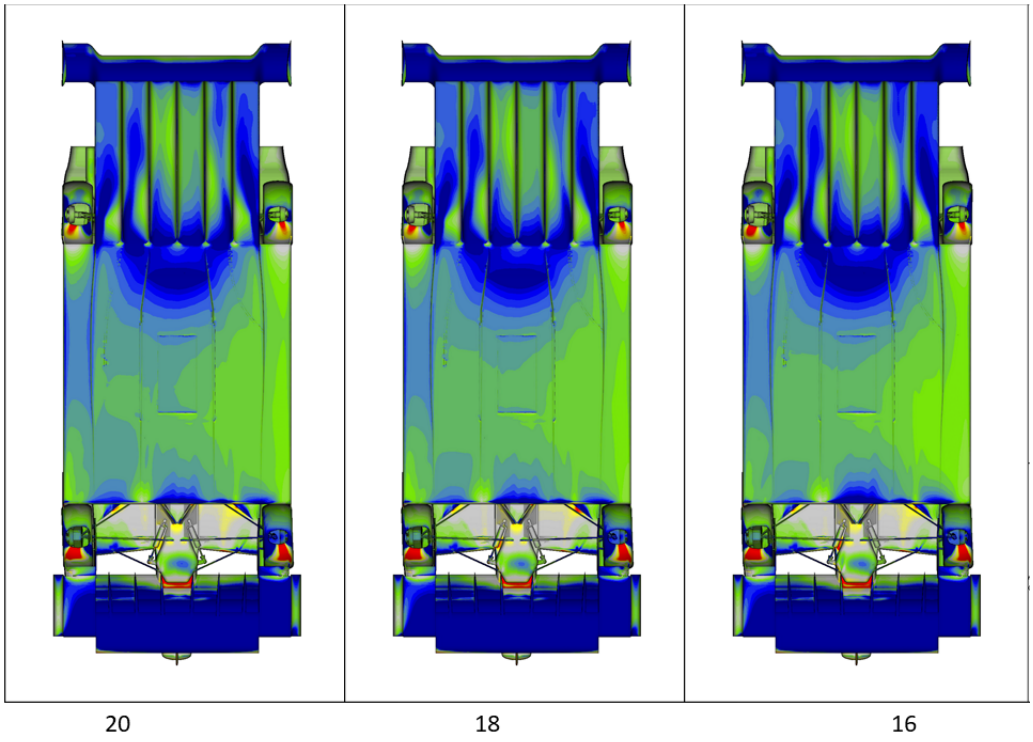

Figure 4.41. 16 (right), 18 (middle), 20 (left) PSI sweep Cpz

changes to the flow field are due to the low slip angle or too low of a pressure change. From the knowledge gained during this study it is safe to assume that increasing both inflation pressure deltas and slip angle would significantly affect the flow field. Larger deformations under low pressure and high slip angle would magnify the tires effect on aerodynamics performance, while the higher-pressure tire ,at the same high slip angle, would show closer resemblance to the rigid tire due to increased stiffness. Furthermore, the dimensions of the tire during the pressure sweep presented a 2 [mm] swing in the max Y deformation along with 2.1 [mm] swing in the Z dimension, both experiencing the largest deformation values at the 16 PSI case. Pursuing a larger test matrix would show if the deformation increases in a different magnitude for different inflation pressures. This case showed that at higher slip angles there is an exponential decrease in deformation between slip angles. It is important to note that for a change in tire pressure there is usually a following change in friction coefficient values increasing as inflation pressure decreases. This was not adjusted in this study as a constant μ of 1.3 was selected to maintain a common baseline. Including μ variation along

with pressure variation would create difficulties understanding which is the driving factor in any performance effects. In addition to the headline numbers and flow characteristics, this inflation pressure study has an effect on development for specific cornering case. As was discussed previously in the results of the straight-line cases, the side deformation created due to slip angle has an effect on flow blockage inwards and outwards of the wheel house. As both the wind tunnel and typical CFD development work are done on one set of tires, they do not capture the different flow structures due to blockage stemming from pressure reduction and increased slip angles. Thus, while at one tire pressure a component at the wheel house can be completely useless, at a different tire pressure it can be engaged and contribute either by drag reduction, or downforce/side force generation. Doing so can adjust the aerodynamic performance according to the required quantities at that point of the race by a simple pressure change. This is an approach that needs to be further tested, as it might be of use for vehicles riding on low tire pressure, while racing series running on high inflation pressures are more likely to be indifferent to this development method. The current tire model did manage to capture the flow characteristics leading to this conclusion, yet the extent of the pressure/slip angle changes, in addition to the fact that no component was specifically designed to capitalize on this phenomenon, concluded with a relatively weak influence on aerodynamic performance. Taking into consideration the increased deformation under higher slip angles as was shown in chapter 2, one can suggest that changing inflation pressures can be used for specific component development approach. Furthermore, it can be used as a tool for in-race strategy as inflation pressure can be adjusted according to the tactics taken by the race crew. It is then recommended to perform a specific study on this phenomenon by designing component of this nature while testing them in various inflation pressures and slip angles.

5. CONCLUSIONS

In this study, a tire modeling technique was presented and executed on race tire designated for a P2 car developed at IUPUI. Using a combination of literature and test data as inputs to the FEA model, the model was generated, analyzed and verified against test data for a similar size tire with good correlation for both static measurements and dynamic ones. This model was then incorporated in the CAD model for a CFD study to determine the significance of tire deformation on the flow field around a semi open-wheel race car. Under straight line conditions, it was shown that the addition of realistic shape and dimensions to the CAD model contributed with a significant increase in both drag and downforce for EOS and cornering RH. Thus, a cornering condition was investigated introducing steer and yaw to both the CAD and the CFD model respectively. The results further showed that including deformation unveils new flow patterns and areas of significance effecting both flow structures and overall forces. Both Drag and downforce numbers showed significant increase in force values local to the tires as well as the mutual relations between the tires and the surrounding components. The difference of results and flow patterns are mainly a product of contact patch shape and size, difference due to loaded and unloaded radius in the deformed tire as well as Y deformation of the whole tire due to the shifted contact patch under cornering conditions. All of which produce flow patterns and vorticies unpredicted by the rigid tire model and thus increased force values. It was shown that introducing deformation along with a valid contact patch shape has the ability to change flow conditions on surrounding components, showing attached flow in region where a rigid tire showed the opposite. The importance of tire deformation for a semi open wheeled car was shown, suggesting that including tire deformation is detrimental for an accurate representation of the flow field, without any distinction between open and closed wheel cars. The study concluded that the tire deformation provided for a more stable data set over all major force variables, both in trend and force values. The study also showed that the geometry of a vehicle will determine its sensitivity to tire deformations. The effects cannot be generalized for all closed wheel cars, rather show the flow patterns and expected behavior under certain conditions. Comparing the rigid and deformed tire under curved flow conditions further supported the claim for

introducing deformation to tires in CFD as, again, the deformed model showed more stable results along with clear trends. The curved domain itself showed that the yawed flow domain tends to over-predict side force generation by a wide margin, thus it is suggested to examine force generation at track testing to verify and correlate both the forces due to deformation, along with the relative difference between WT testing. As both variables are now included in this study, a single-track test suite can compare values from the study and WT testing to isolate variables and thus be able to fully correlate and understand which technique is captured best by CFD. An inflation pressure sweep was included in the study to gain some understanding of the model and vehicle sensitivity to inflation pressure, as this value changes during a race due to both race tactics and wear. The small sample size showed little influence on the aerodynamic performance of the car, whether it is due to low values of yaw/steer, inflation pressure or a combination of the two has yet to be determined and it is assumed to be worthwhile to pursue this further as this yielded a new development approach. The added Y direction deformation in both the contact patch and the centerline of the tire suggested that it is possible to develop stationary components to be modular to RH and in-race states, as the tire deformation mid corner triggers a component to provide forces beneficial to its current state, while as the tire returns to its original heading the increased gap disables that components contribution. This method has the potential to provide for significant gains in performance as development could be bracketed for specific conditions with a lesser reason for generalizing development over a large range of operation. The study presented the complexity involved with introducing tire deformation, as every change in loading, slip angle and inflation pressure has the potential to change flow features upstream and downstream of the tire. The extent of those effects has a wide range of dependencies such as vehicle force generation components and ride height range. The results obtained in this study suggest a more cautious approach should be taken when developing an aerodynamic package for a high deflection tire, as any change to tire orientation and stiffness has the potential to alter flow patterns substantially. The substantial data gathered during this study provided the conclusion that a proper tire model which accurately captures the shape of the tire, contact patch and clearances from the vehicles body is detrimental in order to fully simulate the flow field around a race car. It is as important as the design of a component, such as a

front diffuser, due to its effects up and down stream while its inclusion must be updated according to the loading condition applied to the given state. A distinction between EOS and cornering condition must be accompanied by a respective loading condition change to the tire model in order to fully present the physical state in a CFD simulation. Thus, the incorporation of at least a relatively simple and price efficient tire model as was shown in this study is suggested as a must have condition for any race car aerodynamics development process.

6. FUTURE WORK

It is suggested to test for correlation of both the curved domain as well as the tire model effect itself. The values obtained in this study were correlated to data for a standalone tire, rotating at a single velocity, while temperature effects as well as friction coefficients variation were not included leading to a potential error. As temperature effects were in generally neglected, an approach for estimating temperature buildup in the tire and its effect on the tire deformation was offered. Investigating this phenom would assist with the confidence level of the FEA model, as the current approach includes any temperature losses as hysteresis losses which are independent of velocity and pressure in this case, while in reality they are most definitely dependent. These losses were expressed in a simplistic fashion which can be explored further to determine whether temperature modeling is needed for CFD applications. A larger sample size is suggested as well for the pressure sweep, adding yaw and steer conditions as well as a larger swing in inflation pressures. This aspect would determine just how much inflation pressure effects the aerodynamic performance of a race car. In addition, performing a similar study with a smaller sample size using some LES solver, such as DES, is suggested to ensure that all unsteady flow features confirm with the findings of this study, as some literature sources suggest that using a DES solver unveils unsteady flow patterns not included in RANS simulations. While this study presented data for yaw, steer and pressure sweeps, it did not include any changes to camber. Camber can be easily implemented with the presented tire modeling technique by rotating the tire or road by the X axis. Past work done on the subject suggests that camber has the potential to expose even larger sensitivity to deformation modeling, as the tangential velocity around the tire has an additional component in addition to a more conical contact patch shape which was shown to be a driving factor in regards to flow patterns development around the tire. The work done in this study focused on a relatively small tire with low inflation pressures. It is then recommended that a repeat of this study or some part of it on an array of tires featuring a combination of large tires and stiffer tires, operating under higher inflation pressures, will be pursued. Doing so will uncover the sensitivity due to tire geometry as well as the importance of including deformations for a low deformation tire. Lastly, a development project is suggested using the

approach presented in this study for cornering condition specific design. The study offered a methodology for designing components capable of being triggered due to a change in tire position as an effect of the cornering maneuver. While the study showed the potential this method has, it did not dive in to explore and quantify the effect. Thus, performing a design study where components would be designed to follow this approach would be beneficial as to determine the applicability of the approach as well as providing example of its usage.

REFERENCES

[1] P. Leśniewicz, M. Kulak, and M. Karczewski, "Aerodynamic analysis of an isolated vehicle wheel," in *Journal of Physics: Conference Series*, IOP Publishing, vol. 530, 2014, p. 012 064.

[2] L. Axon, K. Garry, and J. Howell, "An evaluation of cfd for modelling the flow around stationary and rotating isolated wheels," *SAE transactions*, pp. 205–215, 1998.

[3] J. E. Fackrell, "The aerodynamics of an isolated wheel rotating in contact with the ground.," 1974.

[4] S. Diasinos, "The aerodynamic interaction of a rotating wheel and a downforce producing wing in ground effect," *School of Mechanical and Manufacturing Engineering*, 2009.

[5] E. Rajaratnam and D. Walker, "Experimental and computational study of the flow around a stationary and rotating isolated wheel and the influence of a moving ground plane," SAE Technical Paper, Tech. Rep., 2019.

[6] L. I. Prat *et al.*, "Study of the aerodynamics of the formula 1 rear wheels," B.S. thesis, Universitat Politècnica de Catalunya, 2018.

[7] A. Sprot, D. Sims-Williams, and R. Dominy, "The aerodynamic characteristics of a fully deformable formula one wind tunnel tyre.," *SAE International journal of passenger cars. Mechanical systems.*, vol. 5, no. 2, pp. 1026–1041, 2012.

[8] B. Schnepf, T. Schütz, and T. Indinger, "Further investigations on the flow around a rotating, isolated wheel with detailed tread pattern," *SAE International Journal of Passenger Cars-Mechanical Systems*, vol. 8, no. 2015-01-1554, pp. 261–274, 2015.

[9] J. Axerio-Cilies, *Predicting Formula 1 tire aerodynamics: sensitivities, uncertainties and optimization*. Stanford University, 2012.

[10] S. Krajnović, S. Sarmast, and B. Basara, "Numerical investigation of the flow around a simplified wheel in a wheelhouse," *Journal of fluids engineering*, vol. 133, no. 11, 2011.

[11] X. Yang, M. Behroozi, and O. A. Olatunbosun, "A neural network approach to predicting car tyre micro-scale and macro-scale behaviour," *Journal of Intelligent Learning Systems and Applications*, vol. 2014, 2014.

[12] X. Yang, O. Olatunbosun, and E. Bolarinwa, "Materials testing for finite element tire model," *SAE International Journal of Materials and Manufacturing*, vol. 3, no. 1, pp. 211–220, 2010.

[13] W. Blythe and D. E. Seguin, "Friction, tread depth and water; laboratory investigations of passenger car tire cornering performance under minimally-wet conditions," SAE Technical Paper, Tech. Rep., 2013.

[14] R. M. Brach and R. M. Brach, "Modeling combined braking and steering tire forces," SAE Technical Paper, Tech. Rep., 2000.

[15] R. D. Knowles, A. J. Saddington, and K. Knowles, "On the near wake of a formula one front wheel," *Proceedings of the Institution of Mechanical Engineers, Part D: Journal of Automobile Engineering*, vol. 227, no. 11, pp. 1491–1502, 2013.

[16] S. Kurachi, H. Kawamata, K. Hirose, S. Suzuki, and M. Oshima, "Aerodynamic sensitivity analysis of tire shape factors," SAE Technical Paper, Tech. Rep., 2020.

[17] T. Hobeika and S. Sebben, "Cfd investigation on wheel rotation modelling," *Journal of Wind Engineering and Industrial Aerodynamics*, vol. 174, pp. 241–251, 2018.

[18] K. F. Sagmo, "Computational fluid dynamics simulations of a formula student race car-effects predicted by the modelling of a steady state cornering vehicle," M.S. thesis, NTNU, 2016.

[19] M. Nakagawa, S. Kallweit, F. Michaux, and T. Hojo, "Typical velocity fields and vortical structures around a formula one car, based on experimental investigations using particle image velocimetry," *SAE International Journal of Passenger Cars-Mechanical Systems*, vol. 9, no. 2016-01-1611, pp. 754–771, 2016.

[20] P. Eder, T. Gerstorfer, C. Lex, and T. Amhofer, "Investigation of the effect of tire deformation on open-wheel aerodynamics," *SAE International Journal of Advances and Current Practices in Mobility*, vol. 2, no. 2020-01-0546, pp. 1913–1924, 2020.

[21] J. Reiß, J. Sebald, L. Haag, V. Zander, and T. Indinger, "Experimental and numerical investigations on isolated, treaded and rotating car wheels," SAE Technical Paper, Tech. Rep., 2020.

[22] A. Wäschle, "The influence of rotating wheels on vehicle aerodynamics-numerical and experimental investigations," SAE Technical Paper, Tech. Rep., 2007.

A. APPENDIX

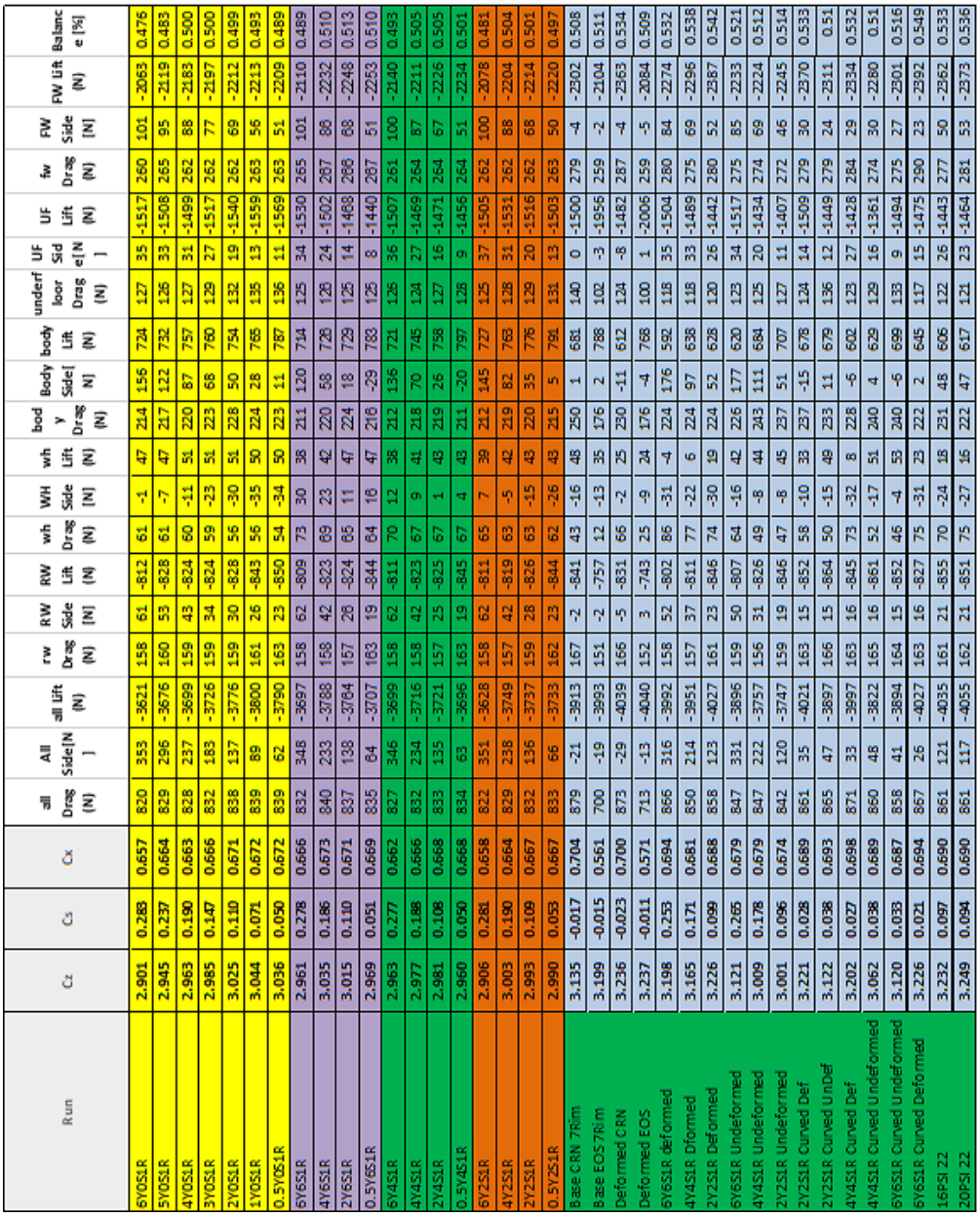

Run	Cz	Cs	Cx	all Drag (N)	All Side[N]	all Lift (N)	rw Drag (N)	RW Side [N]	RW Lift (N)	wh Drag (N)	WH Side [N]	wh Lift (N)	bod y Drag (N)	Body Side[N]	body Lift (N)	underf loor Drag (N)	UF Sid e[N]	UF Lift (N)	fw Drag (N)	FW Side [N]	FW Lift (N)	Balanc e [%]
6Y0S1R	2.901	0.283	0.657	820	353	-3621	158	61	-812	61	-1	47	214	156	724	127	35	-1517	260	101	-2063	0.476
5Y0S1R	2.945	0.237	0.664	829	296	-3676	160	53	-828	61	-7	47	217	122	732	126	33	-1508	265	95	-2119	0.483
4Y0S1R	2.963	0.190	0.663	828	237	-3699	159	43	-824	60	-11	51	220	87	757	127	31	-1499	262	88	-2183	0.500
3Y0S1R	2.985	0.147	0.666	832	183	-3726	159	34	-824	59	-23	51	223	68	760	129	27	-1517	262	77	-2197	0.500
2Y0S1R	3.025	0.110	0.671	838	137	-3776	159	30	-828	56	-30	51	228	50	754	132	19	-1540	262	69	-2212	0.499
1Y0S1R	3.044	0.071	0.672	839	89	-3800	161	26	-843	56	-35	50	224	28	765	135	13	-1559	263	56	-2213	0.493
0.5Y0S1R	3.036	0.050	0.672	839	62	-3790	163	23	-850	54	-34	50	223	11	787	136	11	-1569	263	51	-2209	0.489
6Y6S1R	2.961	0.278	0.666	832	348	-3697	158	62	-809	73	30	38	211	120	714	125	34	-1530	265	101	-2110	0.489
4Y6S1R	3.035	0.186	0.673	840	233	-3788	158	42	-823	69	23	42	220	68	726	126	24	-1502	267	86	-2232	0.510
2Y6S1R	3.015	0.110	0.671	837	138	-3764	157	26	-824	65	11	47	224	18	729	125	14	-1468	266	68	-2248	0.513
0.5Y6S1R	2.969	0.051	0.669	835	64	-3707	163	19	-844	64	16	47	216	-29	783	125	8	-1440	267	51	-2253	0.510
6Y4S1R	2.963	0.277	0.662	827	346	-3699	158	62	-811	70	12	38	212	136	721	126	36	-1507	261	100	-2140	0.493
4Y4S1R	2.977	0.188	0.666	832	234	-3716	158	42	-823	67	9	41	218	70	745	124	27	-1469	264	87	-2211	0.505
2Y4S1R	2.981	0.108	0.668	833	135	-3721	157	25	-825	67	1	43	219	26	758	127	16	-1471	264	67	-2226	0.505
0.5Y4S1R	2.960	0.050	0.668	834	63	-3696	163	19	-845	67	4	43	211	-20	797	128	9	-1456	264	51	-2234	0.501
6Y2S1R	2.906	0.281	0.658	822	351	-3628	158	62	-811	65	7	39	212	145	727	125	37	-1505	262	100	-2078	0.481
4Y2S1R	3.003	0.190	0.664	829	238	-3749	157	42	-819	63	-5	42	219	82	763	128	31	-1531	262	88	-2204	0.504
2Y2S1R	2.993	0.109	0.667	832	136	-3737	159	28	-826	63	-15	43	220	35	776	129	20	-1516	262	68	-2214	0.501
0.5Y2S1R	2.990	0.053	0.667	833	66	-3733	162	23	-844	62	-26	43	215	5	791	131	13	-1503	263	50	-2220	0.497
Base CRN 7Rim	3.135	-0.017	0.704	879	-21	-3913	167	-2	-841	43	-16	48	250	1	681	140	0	-1500	279	-4	-2302	0.508
Base EOS7Rim	3.199	-0.015	0.561	700	-19	-3993	151	-2	-757	12	-13	35	176	2	788	102	-3	-1956	259	-2	-2104	0.511
Deformed CRN	3.236	-0.023	0.700	873	-29	-4039	166	-5	-831	66	-2	25	230	-11	612	124	-8	-1482	287	-4	-2363	0.534
Deformed EOS	3.237	-0.011	0.571	713	-13	-4040	152	3	-743	25	-9	24	176	-4	768	100	1	-2006	259	-5	-2084	0.509
6Y6S1R deformed	3.198	0.253	0.694	866	316	-3992	158	52	-802	86	-31	-4	224	176	592	118	35	-1504	280	84	-2274	0.532
4Y4S1R Dformed	3.165	0.171	0.681	850	214	-3951	157	37	-811	77	-22	6	224	97	638	118	33	-1489	275	69	-2296	0.538
2Y2S1R Deformed	3.226	0.099	0.688	858	123	-4027	161	23	-846	74	-30	19	224	52	628	120	26	-1442	280	52	-2387	0.542
6Y6S1R Undeformed	3.121	0.265	0.679	847	331	-3896	159	50	-807	64	-16	42	226	177	620	123	34	-1517	275	85	-2233	0.521
4Y4S1R Undeformed	3.009	0.178	0.679	847	222	-3757	156	31	-826	49	-8	44	243	111	684	125	20	-1434	274	69	-2224	0.512
2Y2S1R Undeformed	3.001	0.096	0.674	842	120	-3747	159	19	-846	47	-8	45	237	51	707	127	11	-1407	272	46	-2245	0.514
2Y2S1R Curved Def	3.221	0.028	0.689	861	35	-4021	163	15	-852	58	-10	33	237	-15	678	124	14	-1509	279	30	-2370	0.533
2Y2S1R Curved UnDef	3.122	0.038	0.693	865	47	-3897	166	15	-864	50	-15	49	233	11	679	136	12	-1449	279	24	-2311	0.51
4Y4S1R Curved Def	3.202	0.027	0.698	871	33	-3997	163	16	-845	73	-32	8	228	-6	602	123	27	-1428	284	29	-2334	0.532
4Y4S1R Curved Undeformed	3.062	0.038	0.689	860	48	-3822	165	16	-861	52	-17	51	240	4	629	129	16	-1361	274	30	-2280	0.51
6Y6S1R Curved Undeformed	3.120	0.033	0.687	858	41	-3894	164	15	-852	46	-4	53	240	-6	699	133	9	-1494	275	27	-2301	0.516
6Y6S1R Curved Deformed	3.226	0.021	0.694	867	26	-4027	163	16	-827	75	-31	23	222	2	645	117	15	-1475	290	23	-2392	0.549
16PSI 22	3.232	0.097	0.690	861	121	-4035	161	21	-855	70	-24	18	231	48	606	122	26	-1443	277	50	-2362	0.533
20PSI 22	3.249	0.094	0.690	861	117	-4055	162	21	-851	75	-27	16	222	47	617	121	23	-1464	281	53	-2373	0.536

Figure A.1. Test Results